TRIPLE-NEGATIVE BREAST CANCER MICROENVIRONMENTS: MOLECULAR AND HISTOLOGIC PORTRAITS

Ashley M. Fuller

A dissertation submitted to the faculty at the University of North Carolina at Chapel Hill in partial fulfillment of the requirements for the degree of Doctor of Philosophy in the School of Medicine (Pathology and Laboratory Medicine).

Chapel Hill
2018

Approved by:

Melissa A. Troester

William B. Coleman

Stephen D. Hursting

Liza Makowski

Cyrus Vaziri

ABSTRACT

Ashley M. Fuller: Triple-negative breast cancer microenvironments: Molecular and histologic portraits
(Under the direction of Melissa A. Troester)

Triple-negative breast cancer (TNBC), comprised predominantly of the basal-like (BBC) and claudin-low (CLBC) intrinsic subtypes, is a proliferative, invasive disease that accounts for 15-20% of breast cancer cases. Unlike with other breast cancer subtypes, TNBC treatment modalities are generally limited to surgery, radiation, and cytotoxic chemotherapy. Therefore, identification of molecular contributors to TNBC initiation and progression, including signals with relevance to the tumor microenvironment, is important for development of biologically targeted therapies.

It is well accepted that the tumor microenvironment, the non-cancerous cells and tissues in proximity to the frank cancer cells, plays a critical role in breast cancer initiation and progression. However, little is known about the evolution of stromal-epithelial communication during breast tumorigenesis, or how specific signaling mediators alter subtype-specific tumor behavior. To this end, this work leveraged a suite of model systems to better understand how specific components of TNBC microenvironments influence tumor phenotypes and stromal-epithelial interactions. Following a literature review in Chapter 1, Chapter 2 describes research that used three-dimensional culture models of a pre-invasive BBC cell line panel, together with novel imaging technology, to evaluate cancer cell-fibroblast interactions during early stages of tumor initiation. Relative to wild-type cells, pre-invasive BBC cells lacking the *TP53* tumor suppressor gene exhibited accelerated and unique responses to fibroblast co-culture. In Chapter 3, the role of the immune

microenvironment in TNBC progression was evaluated using a novel animal model. Myeloid-specific *Glut1* knockout mice were used to demonstrate that alterations in myeloid cell metabolism reduced the inflammatory potential of mammary tissue macrophages (MTMs) and impeded CLBC progression. Chapter 4 leveraged observational studies of human tissue to develop a digital algorithm to identify histologically stained endothelial cells in cancer-adjacent breast. This algorithm will be used in future studies to quantitatively characterize the vascular microenvironment both across breast cancer subtypes, and for TNBCs in particular. Finally, Chapter 5 integrates insights from all three investigations to identify future directions for studies of TNBC microenvironments. This work reveals previously uncharacterized relationships between TNBCs and their associated stromal cells, some of which may represent plausible therapeutic targets for this tumor subtype.

ACKNOWLEDGEMENTS

Although there is only one author indicated herein, this work was, in fact, a team effort that would have been impossible without the input of many. I would first like to thank my mentor, Melissa Troester, for welcoming me into her laboratory. It has been a privilege to work in such a collaborative, interdisciplinary, and translational environment that has both fostered my development as a scientist and helped to refine my career goals. I would also like to thank Liza Makowski for her mentorship in navigating a challenging mouse study; I am a better scientist for the experience. I have genuinely enjoyed my time with my colleagues in both labs, and I look forward to our future collaborations.

I am also grateful to my committee members, Bill Coleman, Steven Hursting, and Cyrus Vaziri, for their insight during the course of this dissertation. I have been fortunate to work with this collegial group of scholars. I would also like to acknowledge my many collaborators, and particularly those in Amy Oldenburg's laboratory, without whom a significant portion of Chapter 2 of this work would not have been possible. I would further like to thank the staff of the Histology Research Core Facility, Translational Pathology Laboratory, Flow Cytometry Core Facility, and Lineberger Comprehensive Cancer Center Genomics Core Facility for their respective expertise. Finally, financial support from the Royster Society of Fellows and UNC Integrated Vascular Biology Program helped make this work possible.

Last, but not least, I would like to thank my family and friends (both two- and four-legged!) for their unwavering encouragement and diverting comedic relief. I am more grateful to all of you than words can express. You know who you are.

PREFACE

Chapter 1 is a previously unpublished overview of breast cancer risk factors, molecular features, and microenvironmental constituents, particularly as they relate to triple-negative breast cancers (TNBCs). All figures have been created for the express purpose of this chapter and have not previously appeared elsewhere.

The study presented in Chapter 2 is a manuscript in preparation that explores how gene-microenvironment interactions influence epithelial phenotypes and gene expression patterns associated with TNBC carcinogenesis. As lead author, I conceptualized the study, designed experiments, and analyzed all data reported in this document. Optical coherence tomography was performed in collaboration with Lin Yang, PhD and Xiao Yu, PhD; related financial and materials support was provided by Amy Oldenburg, PhD. Microarrays were run by the staff of the Lineberger Comprehensive Cancer Center Genomics Core Facility. Jason Pirone, PhD assisted with deconvolution of co-culture gene expression data, and Melissa Troester, PhD provided additional intellectual input, as well as financial and materials support. Finally, Rupninder Sandhu, PhD, designed and performed additional microarray experiments that will appear in the final document submitted for publication.

Chapter 3 discusses how alterations in macrophage glucose metabolism modulate mammary gland inflammation and TNBC progression in a murine model. It also identifies novel macrophage phenotypes that may be important in TNBC biology. This study is approaching re-submission and has been reformatted from its original version in accordance with university dissertation formatting requirements. Please note that the text presented herein will likely deviate from the final published form. Co-authors include Alyssa J. Cozzo,

Alex J. Freemerman, J. Ashley Ezzell, Joseph A. Galanko, Stephen D. Hursting, Melissa A. Troester, and Liza Makowski.

Chapter 4 describes the development of a novel digital algorithm designed to quantitate CD31 immunohistochemical staining (vascular endothelial cells) in cancer-adjacent, histologically benign human breast tissue. This algorithm will ultimately be used to investigate how patterns of endothelial cell marker distribution relate to breast cancer subtype, known breast cancer risk factors, and other histologic tissue features. Co-authors on this manuscript will include Linnea Olsson, Bentley R. Midkiff, Kirk K. McNaughton, J. Ashley Ezzell, Erin L. Kirk, and Melissa Troester.

Chapter 5 is an integrative summary of the data presented in Chapters 2, 3, and 4. It also describes ongoing analyses and identifies future directions for studies of TNBC microenvironments. Finally, due to substantial redundancy among chapters, a single list of references can be found at the end of this dissertation. Please note that ref. 183 is an unpublished manuscript from L. Makowski's group.

TABLE OF CONTENTS

LIST OF TABLES

LIST OF FIGURES

LIST OF ABBREVIATIONS AND SYMBOLS

$^{-/-}$	Knockout; null
ΔΔCt	Comparative analytical method for quantitative polymerase chain reaction
2D	Two-dimensional
2-DG	2-deoxyglucose
3’	3-prime end of nucleic acid
3D	Three-dimensional
5’	5-prime end of nucleic acid
α-SMA	alpha-smooth muscle actin
A_0	Number of initial cells in growth curve
AAALAC	Association for Assessment and Accreditation of Laboratory Animal Care
ADH	Atypical ductal hyperplasia
AHF	Atypical ductal hyperplasia-associated fibroblasts
ANOVA	Analysis of variance
APC	Antigen-presenting cell
ARG1	Arginase I
A_t	Number of cells at time “t” in growth curve
BBC	Basal-like breast cancer
BCA	Bicinchoninic acid
BMDM	Bone marrow-derived macrophage
BMI	Body mass index
BrdU	Bromodeoxyuridine
CAF	Cancer-associated fibroblast
CAN	Cancer-adjacent normal
CBCS	Carolina Breast Cancer Study
CC3	Cleaved caspase-3

CCL	Chemokine (C-C motif) ligand
CD	Cluster of differentiation
cDNA	Complementary DNA
CI	Confidence interval
CLBC	Claudin-low breast cancer
CK5/6	Cytokeratin 5/6
CK14	Cytokeratin 14
cKIT	Tyrosine-protein kinase Kit
cm	Centimeter
cMET	Tyrosine-protein kinase Met
CXCL	Chemokine (C-X-C) motif ligand
DAB	Diaminobenzidine
DCIS	Ductal carcinoma *in situ*
DMEM	Dulbecco's modified Eagle's medium
DSB	Double-strand break
ECM	Extracellular matrix
EGFR	Epidermal growth factor receptor
EMT	Epithelial-mesenchymal transition
ER	Estrogen receptor
FAP	Fibroblast activation protein
FBS	Fetal bovine serum
FFPE	Formalin-fixed, paraffin-embedded
FMO	Fluorescence-minus-one flow cytometry control
FOXP3	Forkhead box P3
FSP-1	Fibroblast-specific protein-1
g	Gram

GEMM	Genetically engineered mouse model
Glut1	Glucose transporter 1 protein
Glut1$^{M-/-}$	Glucose transporter 1 gene, myeloid-specific knockout (mouse)
Glut1$^{MFl/Fl}$	Glucose transporter 1 gene, myeloid-specific floxed (mouse)
H&E	Hematoxylin and eosin
HEPES	4-(2-hydroxyethyl)-1-piperazineethanesulfonic acid
HER1	Human epidermal growth factor receptor 1
HER2	Human epidermal growth factor receptor 2
HGF	Hepatocyte growth factor
hTERT	Human telomerase reverse transcriptase
IHC	Immunohistochemistry; immunohistochemical
iNOS	Inducible nitric oxide synthase
I	Coefficient of interaction in Buess method of gene expression deconvolution
IL	Interleukin
k	First-order rate constant of cell growth
LOH	Loss of heterozygosity
LysM-cre	Cre recombinase linked to lysozyme 2 gene
MCP-1	Monocyte chemoattractant protein 1
M-CSF	Macrophage colony-stimulating factor
MFP	Mammary fat pad
MFI	Median fluorescence intensity
M	Molar
µg	Microgram
mg	Milligram
MHCII	Major histocompatibility complex II
miR	microRNA

µL	Microliter
mL	Milliliter
µm	Micrometer
mm	Millimeter
MMP	Matrix metalloproteinase
MT	Masson's trichrome
MTM	Mammary tissue macrophage
ng	Nanogram
nm	Nanometer
NBS	Normal Breast Study
OCT	Optical coherence tomography
OD	Optical density
OR	Odds ratio
p53	Tumor protein p53 (also: *TP53*, *Trp53*)
PAI-1	Plasminogen activator inhibitor-1
PARP	Poly(ADP-ribose) polymerase
pCR	Pathologic complete response
PDAC	Pancreatic ductal adenocarcinoma
PDGFRβ	Platelet-derived growth factor receptor beta
PDT	Population doubling time
PR	Progesterone receptor
qRT-PCR	Quantitative reverse transcription-polymerase chain reaction
RB1	Retinoblastoma protein
RMF	Reduction mammoplasty fibroblast
RNA	Ribonucleic acid
RPMI	Roswell Park Memorial Institute

rRNA	Ribosomal RNA
ROUT	Non-linear regression with outlier removal
SAM	Significance analysis of microarrays
SEER	Surveillance, Epidemiology, and End Results Program
SEM	Standard error of the mean
-sh:GFP	Small hairpin RNA targeting green fluorescent protein
-sh:p53	Small hairpin RNA targeting p53
shRNA	Small hairpin RNA
SVF	Stromal vascular fraction
t	Time
TAM	Tumor-associated macrophage
TBS-T	Tris-buffered saline with 0.1% TWEEN-20
TDLU	Terminal ductal lobular unit
Tg	Transgenic
TGFβ	Transforming growth factor beta
TNBC	Triple-negative breast cancer
TNFα	Tumor necrosis factor alpha
UNC	University of North Carolina
US	United States
VE-cadherin	Vascular endothelial cadherin
WAP	Whey acidic protein
WHR	Waist-hip ratio
Y	Tyrosine

CHAPTER 1

INTRODUCTION TO THE NORMAL BREAST, BREAST CANCER, AND TISSUE MICROENVIRONMENTS

1.1. Normal mammary gland development, anatomy, and histology: a précis

The normal mammary gland is a complex, dynamic structure that undergoes numerous anatomic and functional changes throughout life [1]. Initial stages of mammary gland development occur during the pre-natal period, wherein ectodermal bud cells embedded within the mammary mesenchyme proliferate and invade into the mammary fat pad to form a small ductal epithelial tree [2]. Unlike most other organs, remaining stages of mammary gland development occur postnatally. During puberty, inductive hormonal and growth factor-derived signals stimulate extensive elongation and lateral branching of the nascent epithelial tree, and promote the differentiation of contractile myoepithelial cells [3]. This mature, adult breast tissue can undergo further differentiation during later life stages such as pregnancy and lactation, culminating in the formation of a milk-producing, lobulo-alveolar compartment [1, 2]. Following the cessation of lactation, the process of involution returns the parous mammary gland to a pre-pregnancy-like morphology via the activation of highly regulated developmental and wound-healing pathways [4, 5].

In adult women, the breast contains 15-25 secretory lobes that are embedded within stromal (connective) tissue and arranged radially around the nipple (**Figure 1.1A**). Each lobe is comprised of 20-40 glandular lobules (also known as terminal ductal lobular units [TDLUs]), which constitute the functional (i.e., milk-producing) acinar units of the mammary

gland (**Figure 1.1A-B**). Histologically, the mammary gland is composed of an outer layer of contractile myoepithelial cells and an inner layer of cuboidal to columnar luminal epithelium; this latter cell type can be further sub-divided into secretory lactocytes and non-secretory ductal cells [6, 7]. Importantly, the epithelial and stromal compartments of the breast are separated by a laminin-rich basement membrane (**Figure 1.1C**) [8].

1.2. Overview of breast cancer incidence and mortality

Breast cancer predominantly arises from the luminal ductal epithelial cells of the mammary TDLU [8] and is the most common non-cutaneous malignancy among women in the United States (US). Breast cancer is also the second-leading cause of cancer-related mortality in this population, with an estimated 266,120 new cases and 40,920 deaths anticipated in 2018 [9]. According to 2010-2014 Surveillance, Epidemiology, and End Results Program (SEER) data, breast cancer in the US is most frequently diagnosed among women aged 55-64 (median age at diagnosis: 62 years; seer.cancer.gov), although the median age at diagnosis is lower for African American than Caucasian women (59 vs. 63 years; www.cancer.org). Indeed, race is an important determinant of breast cancer risk and mortality. Among all breast cancer cases, breast cancer incidence from 2010-2014 was higher in Caucasian and African American women than in any other racial or ethnic group (128.7 and 125.5 cases/100,000 women, respectively; www.cancer.org). However, African American women have the highest breast cancer incidence rates prior to the age of 40, and are more likely to experience breast cancer-associated mortality irrespective of age (www.cancer.org).

1.3. Breast cancer subtypes

Beginning in the early 2000s, a molecular taxonomy of “intrinsic” breast cancer subtypes (luminal A, luminal B, human epidermal growth factor [HER2]-enriched, basal-like [BBC], and claudin-low [CLBC]) was identified on the basis of tumor gene expression patterns. These subtypes were found to differ substantially with respect to tumor molecular features, risk factors, treatment responses, and patient outcomes [10-16]. A sixth intrinsic subtype, normal-like breast cancer, is now believed to reflect contamination of tumor RNA with that of surrounding normal breast tissue [17]. Surrogate immunohistochemical (IHC) markers, including the estrogen receptor (ER), progesterone receptor (PR), and HER2, are routinely used to identify breast cancer subtypes in clinical settings; however, it should be noted that IHC-based and intrinsic subtype designations do not completely converge [18]. Nevertheless, luminal A and luminal B breast cancers (herein referred to as “luminal” cancers unless otherwise specified) are generally ER^+/PR^+, whereas basal-like and claudin-low tumors are typically negative for all three IHC-based biomarkers ($ER^-/PR^-/HER2^-$; so-called “triple-negative” breast cancers [TNBCs]). Interestingly, recent publications have reported that the utilization of additional IHC markers, including HER1, epidermal growth factor receptor (EGFR), and/or cytokeratin 5/6 (CK5/6), can facilitate diagnoses of BBC more specifically [19-23]. In fact, a five-marker IHC panel consisting of ER, PR, HER2, EGFR, and CK5/6 has been shown to predict BBC patient survival more accurately than the original triple-negative phenotype [20].

The focus of this dissertation research is triple-negative breast cancer. As described below, TNBC is characterized by poor clinical outcomes relative to other breast cancer subtypes, and exhibits molecular features that preclude effective utilization of currently available biologically targeted therapies. A better understanding of TNBC biology at all stages of disease is critical for improving patient outcomes

1.4. Features of triple-negative breast cancers

Triple-negative breast cancers exhibit unique risk factor profiles, molecular features, and clinical behaviors in comparison to other breast cancer subtypes. In this section, the clinical and molecular properties of human TNBCs (defined by the three-marker IHC profile), as well as those of BBCs more specifically, will be described in detail. Features of human CLBCs will also be presented in accordance with data availability; however, it should be noted that substantially less is known about CLBCs relative to the remaining intrinsic subtypes.

1.4.1. Risk factors

Age and race: Triple-negative breast cancers account for approximately 15-20% of all breast cancer cases in the general population, but are more prevalent among pre-menopausal and African American women [19, 22]. Specifically, compared to luminal A cases, patients with BBC (defined as $ER^-/PR^-/HER2^-/HER1^+$, and/or $CK5/6^+$) were 2.1 times more likely to be African American [19, 22], and 4.5 times more likely to be younger than 40 years of age [22]. Moreover, prevalence estimates indicated that BBC was significantly more prevalent in pre- compared to post-menopausal African American women (39% and 14%, respectively), as well as non-African American women of any age (16%), even after adjustment for tumor stage at diagnosis [19]. Similarly, a study of a racially heterogeneous population found that, compared to women of any other racial or ethnic group, African American women were 3 times more likely to present with TNBCs irrespective of age [24].

Obesity status: The relationship between obesity and breast cancer is controversial, as positive, negative, and null associations have been reported in the literature [25]. However, accumulating evidence indicates that obesity is associated with increased risk of TNBC, particularly among young/pre-menopausal women. For example, a pooled analysis

of 35,568 cases from the Breast Cancer Association Consortium revealed that, among women ≤50 years of age, obese women (defined as having a body mass index [BMI] ≥30 kg/m^2) were 1.8 times more likely to present with triple-negative (defined as ER$^-$/PR$^-$/HER2$^-$) compared to ER$^+$/HER2$^-$ or PR$^+$/HER2$^-$ tumors [26]. Similarly, data from the Seattle-Puget Sound SEER cancer registry indicated that obesity was associated with a 1.3-fold elevated risk of TNBC among women of all ages, and that risk of TNBC, but not non-TNBC, was further elevated among younger women aged 41-45 (odds ratio [OR]: 2.2; 95% confidence interval [CI]: 0.9-5.24) [27].

In addition to positive associations between obesity and ER$^-$/PR$^-$/HER2$^-$ TNBC, relationships between obesity and BBC have also been described. For instance, compared to patients with luminal A tumors, BBC patients were 3.75-fold more likely to be highly obese (BMI ≥35 kg/m^2) than normal weight (BMI 18.5-24.9 kg/m^2) [28]. Additionally, in the Carolina Breast Cancer Study (CBCS), a population-based study that oversampled for younger (<50 years of age) and African American women, an elevated waist-hip ratio (WHR) was strongly associated with BBC in both pre- and post-menopausal women [22]. Interestingly, BMI was not associated with BBC in this study [22], consistent with views that WHR is a superior metric of adiposity given that it better reflects important considerations such as adipose tissue distribution (e.g. central/abdominal vs. peripheral) [29, 30].

Reproductive history: It is well established that early menarche, nulliparity, late age at first birth, and never having breastfed are associated with an increased risk of breast cancer. As such, recent studies have sought to establish whether these reproductive variables are also associated with increased TNBC risk. Increased duration of breastfeeding is the single reproductive factor most consistently associated with reduced risk of both TNBC and BBCs more specifically [22, 31, 32]. Interestingly, this association has been shown to be modified by age and race, as parous African American women between 20 and 44 years of age who breastfed for at least 6 months had an 82% lower TNBC risk than

parous African American women who had never breastfed [32]. In addition, an inverse association between age at menarche and TNBC/BBC risk has been reported in a small number of studies [22, 33, 34]. However, both parity and younger age at first birth have been inconsistently associated with TNBC risk, with certain studies reporting positive associations [22, 33, 35, 36], and others failing to reach statistical significance [reviewed in 31].

1.4.2. Clinical presentation

Triple-negative breast cancers present as palpable tumors in the majority of patients, likely due to the reduced rates of mammographic screening in younger and African American women compared to older and Caucasian women, respectively [37]. These cancers also frequently present as high grade, high stage, and highly mitotic lesions; are poorly differentiated in approximately 90% of cases [19, 37]; and are characterized by geographic patterns of necrosis, strongly demarcated “pushing borders” of invasion, and conspicuous lymphocytic infiltrates [21].

1.4.3. Molecular features

Basal-like subtype: Basal-like breast cancers are more molecularly homogeneous than TNBCs classified according to the three-marker IHC panel (i.e., $ER^-/PR^-/HER2^-$ tumors), and were first described in the late 1980s using IHC data collected from benign and malignant breast tissue specimens [38, 39]. These tumors were designated “basal-like” due to their expression of cytoskeletal proteins associated with the basal (myoepithelial) layer of the normal mammary gland, including CK5/6, CK14, and vimentin [21, 23, 38-40]. At the genomic level, BBCs are also enriched for a “basal-like” gene cluster, consisting of growth factor receptors such as *MET* (cMET), *EGFR*, and *KIT* (cKIT); cytoskeletal elements such as *CAV1* and *CAV2* (caveolins 1 and 2) and *CDH3* (p-cadherin); and the gene encoding the

small heat shock protein, αB-crystallin (*CRYAB*), among others [41]. However, it is important to note that BBCs do not originate from the myoepithelium despite their similarities to this cell type. Instead, elegant genetic studies in murine models have suggested that these tumors, or at least a subset thereof, are derived from mammary luminal epithelial progenitors [42].

In accordance with their highly mitotic behavior, BBCs exhibit genetic defects that accelerate cellular proliferation and undermine cell stress responses. Most notably, >80% of these tumors harbor mutations in *TP53* (tumor protein 53; p53) [19, 43], a master regulator of genome stability. Importantly, compared to luminal breast cancers wherein missense *TP53* mutations predominate in approximately 12-35% of cases, BBCs are substantially enriched for deleterious nonsense (truncation), frameshift, and splice-site mutations that severely impair p53 protein function [43, 44]. In fact, although p53-wild-type (WT) BBCs have been reported in the literature, an analysis of genetic signatures of inferred p53 pathway activity in 506 breast tumors revealed that loss of p53 pathway function may be a feature of most, if not all, BBCs [43]. Future research should address the impact of specific *TP53* mutation types on therapeutic responses and patient survival, particularly in association with tumor subtype and other prognostic clinicopathologic characteristics.

In addition to exhibiting unique *TP53* mutation profiles, BBCs are also strongly associated with germline mutations in the tumor suppressor gene *BRCA1*, a critical component of the DNA double-strand break (DSB) repair pathway. Indeed, Foulkes et al. demonstrated that tumor-specific expression of CK5/6 (i.e., a “basal-like” epithelial phenotype) was significantly associated with the presence of *BRCA1* germline mutations [45], whereas Sorlie et al. found that 100% of tumors from *BRCA1* mutation carriers fell within the basal-like intrinsic subtype [46]. Interestingly, with the recent development of experimental poly(ADP-ribose) polymerase (PARP) inhibitors, the association between germline *BRCA1* mutations and BBCs now has important clinical implications, with the

combination of *BRCA1* loss-of-function and PARP inhibition inducing synthetic lethality in cancer cells [47].

Claudin-low subtype: First reported in 2007, CLBC is the most recently identified intrinsic breast cancer subtype. Early genomic studies of 13 human claudin-low tumors, 12 of which were ER^-, indicated that these lesions exhibited low expression levels of tight junction proteins such as *CLDN3*, *CLDN4*, and *CLDN7* (hence, "claudin-low"), and high expression levels of lymphocyte and endothelial cell markers [48]. Further work has revealed both similarities and differences between claudin-low and basal-like tumors. For example, like BBCs, CLBCs are more likely to present as large ($\geq$2 cm), high-grade, undifferentiated lesions with circumscribed borders [49]. In contrast to basal-like tumors, however, CLBCs are characterized by a mesenchymal morphology and are genomically enriched for markers of cancer stem cells and the epithelial-mesenchymal transition [12, 50]. CLBCs are also more likely than BBCs to be ER^+ or non-triple-negative [50, 51], indicating the potential for greater heterogeneity among claudin-low relative to basal-like tumors [51].

1.4.4. Prognosis and clinically available treatment modalities

Due in part to the highly proliferative nature of TNBCs, these tumors exhibit more favorable responses to cytotoxic chemotherapy than ER^+ and $HER2^+$ cancers, particularly in the neoadjuvant (pre-operative) setting [52-54]. Indeed, the cytotoxic agents used in the treatment of TNBCs, such as fluorouracil, alkylating agents (e.g., cyclophosphamide), anthracyclines (e.g., doxorubicin; epirubicin), and taxanes (e.g., paclitaxel; docetaxel) non-specifically target actively dividing cells; hence, it follows that highly mitotic TNBC cells would exhibit greater susceptibility to these drugs than more indolent (i.e., luminal) cancers. Accordingly, significantly higher rates of pathologic complete response (pCR; defined as a lack of histologic evidence of residual invasive cancer cells following neoadjuvant chemotherapy) have been observed in TNBC compared to non-TNBC patients [53, 55].

Further, among cases achieving pCR, no survival differences have been reported in association with tumor subtype within the first ~5-6 years of follow-up [53, 56]. Interestingly, in one study of 5447 clinically annotated breast cancers, expression of a proliferation-related metagene in claudin-low tumors was significantly lower than in BBCs, but significantly higher than in luminal A tumors [51]. Thus, although this study did not detect significant differences in disease-free survival between CLBC and BBC patients within the first 10 years of follow-up [51], more comprehensive evaluations of long-term CLBC patient survival is an important avenue of future research.

Despite their relatively increased neoadjuvant chemosensitivity, TNBCs for which pCR is not achieved are paradoxically more likely than other breast cancer subtypes to locally recur and/or distantly metastasize – particularly to visceral organs and the central nervous system – within the first 3 to 5 years of patient follow-up [52, 53, 57, 58]. These observations illustrate the need to develop novel treatments that improve the progression-free and overall survival of TNBC patients, particularly for those with residual disease (i.e., non-pathologically complete responders) following neoadjuvant therapy.

1.5. The tumor microenvironment: Concepts, model systems, and constituents

One possible explanation for the relatively increased rates of TNBC recurrence pertains to the concept of the “tumor microenvironment” or “tumor stroma,” the collection of non-cancerous cell and tissue types within (intratumoral microenvironment) and surrounding (extratumoral or cancer-adjacent microenvironment) a frank cancer. While the normal tissue microenvironment is indispensable for maintenance of tissue homeostasis and repression of tumorigenesis, evolving stromal-epithelial interactions in the context of cancer exert profound tumor-promoting effects [59]. In this section, experimental model systems used to

study stromal-epithelial interactions in breast cancer, as well as the advantages and disadvantages thereof, will be discussed. Specific constituents of the tumor microenvironment germane to this dissertation research, including fibroblasts, macrophages, and endothelial cells, will also be described as they relate to TNBCs.

1.5.1. Model systems for studies of the tumor microenvironment

In vitro *co-culture models*: Cancer cell lines cultured *in vitro* on plastic dishes ("monocultures") are perhaps the most ubiquitous models used to study genetic and molecular aberrations associated with tumor initiation and progression. Indeed, extensive work has been undertaken to comprehensively characterize the molecular features, including intrinsic subtypes, of over 50 breast cancer cell lines [60]. However, these models are only informative of cancer cell-intrinsic defects, and cannot be used to explore microenvironmental influences on cancer cell biology.

In response to the limitations of cancer cell monocultures, two-dimensional (2D) co-culture models have been developed to enable studies of stromal-epithelial interactions. These highly tractable model systems consist of two (or more) cell types grown either in direct physical contact ("direct" co-cultures; **Figure 1.2A**) or separated by a "transwell," a porous physical barrier that enables cellular communication exclusively via soluble signaling mediators (**Figure 1.2B**). Although both types of 2D co-culture models have shown utility in gene expression studies [reviewed in 61], transwell cultures are particularly useful for evaluating the influence of the microenvironment on cancer cell phenotypes such as proliferation, migration, and invasion [62]. Importantly, however, 2D co-culture models exhibit limited physiological relevance, because: 1) rigid culture substrates, such as plastic and glass, exhibit substantially greater mechanical stiffness than even the stiffest living tissue [63]; and 2) the morphologic and organizational features of cells in 2D culture do not emulate *in vivo* conditions due to the loss of important contextual signals [64].

To study stromal-epithelial interactions in a more tissue-relevant environment, three-dimensional (3D) co-cultures can be used. Several variations of this model have been reported in the literature [reviewed in 62]; however, one of the most widely used variations is the “spheroid” or “organoid” culture, wherein breast epithelial cells suspended in a 3D collagen- and laminin-rich extracellular matrix (ECM) form polarized, multi-cellular structures that closely recapitulate the *in vivo* architecture of mammary gland secretory acini [65, 66] (**Figure 1.2C-D**). Over the last 3 decades, pioneering work has demonstrated that the ECM plays a critical role in maintaining tissue integrity by imparting both structural support and mechanosignaling cues to surrounding epithelia (for an excellent comprehensive review that provides a historical perspective on the utility of 3D cultures to studies of the tumor microenvironment, refer to ref. [67]). Thus, 3D co-cultures represent powerful tools with which to study normal stromal-epithelial communication patterns “in context”, and to understand how these interactions change in the setting of malignancy. However, one challenge associated with the use of 3D co-cultures is the limited number of techniques that can quantitatively assess alterations in organoid phenotypes. Development of novel analytical approaches, particularly in the realm of biomedical imaging, is an active area of current research [68-71] (see also, Chapter 2).

In vivo *murine models*: Utilization of murine models facilitates a comparative biology approach to studies of the tumor microenvironment. Two of the most widely used types of murine models include orthotopic models, wherein murine cancer cells are orthotopically injected into syngeneic mice, and xenograft models, in which human cancer cells are heterotopically implanted into immunocompromised animals. However, these models possess certain limitations: Orthotopic tumors do not mimic many of the etiologic and/or molecular features of human tumors, whereas xenograft tumors do not develop in the context of an immunocompetent human microenvironment, precluding analyses of how stromal-epithelial interactions influence the course of human disease [72]. In contrast,

genetically engineered mouse models (GEMMs), wherein expression of a given gene can be spatially and/or temporally controlled, can more closely recapitulate specific aberrations found in human tumors. In fact, recent genomic expression analyses have identified GEMM "counterparts" to human breast cancer intrinsic subtypes [73]. For example, mammary tumors from three mouse lines, including the Tg (transgenic) C3(1)-*Tag*, TgWAP-*Myc*, and *Trp53*$^{-/-}$ (p53-null) lines, cluster with human BBCs [73], suggesting that these models may be particularly useful for studies of basal-like microenvironments. Interestingly, a single GEMM analogous to human CLBC was not identified in this study; instead, the gene expression patterns of unique tumors from multiple GEMMs converged to form a claudin-low expression class [73]. Nevertheless, two additional GEMMs that closely mimic the genomic expression patterns of human CLBC have been described, including: 1) orthotopic, syngeneic, transplantable tumors from a *Trp53*$^{-/-}$ mouse (T11 model) [73, 74]; and 2) transgenic mammary-specific Met-overexpressing mice harboring a conditional loss of *Trp53*, also in the mammary epithelium [75].

Cancer-adjacent normal tissue: Studies of cancer-adjacent normal (CAN) breast tissue can reveal important associations between tumor biology and features of extra-tumoral microenvironments as they relate to breast cancer subtypes. In particular, given that TNBCs are more likely than other subtypes to locally recur within the first 3 to 5 years of patient follow-up [52, 53, 57, 58], these studies may yield important insights into microenvironmental factors that contribute to subtype-specific differences in disease recurrence. Accordingly, recent work has shown that the genomic expression patterns of CAN breast tissue differ in association with the intrinsic subtype [76] or ER status [77] of the corresponding tumor. Studies of CAN tissue have also identified extra-tumoral gene signatures that predict mortality among ER^{+} cases [78], as well as in "whole tumor" datasets independent of subtype [79], or ER or HER2 status [80]. However, given that these studies have primarily focused on global CAN tissue gene expression patterns, future work should

examine associations between tumor clinicopathologic factors and specific components of the extra-tumoral microenvironment, particularly in the context of TNBCs (see also, Chapter 4).

1.5.2. Cellular constituents of TNBC microenvironments

Fibroblasts: Fibroblasts are a major stromal cell component of many normal tissue types, including breast, and primarily function in the production and secretion of ECM, as well as the regulation of epithelial cell differentiation and polarity [81]. In the setting of cancer, however, numerous studies suggest that dysregulated fibroblasts (also known as cancer-associated fibroblasts [CAFs]) facilitate tumor progression by promoting ECM remodeling, inflammation, angiogenesis, and tumor cell proliferation [reviewed in 81]. Indeed, both high mammographic density (a radiologic metric of fibroglandular breast content) and a high histologic stroma-tumor ratio are negative prognostic indicators in breast cancer, particularly among TNBCs and ER^- tumors, respectively [82-84].

Little is known about fibroblast-epithelial interactions as they relate to breast cancer subtypes. However, one study by Camp et al. [85] revealed that stromal-epithelial communication patterns are distinct in co-culture models of basal-like vs. luminal breast cancer. Specifically, fibroblast-luminal co-cultures upregulated genes involved in a number of cellular proliferation pathways, whereas fibroblast-BBC co-cultures upregulated genes associated with immune signaling and wound healing responses. Consistent with this gene expression data, basal-like, but not luminal, breast cancer cells also exhibited enhanced migratory and wound-healing capacities in response to fibroblast co-culture [85]. Interestingly, primary fibroblasts isolated from the interface zone of human TNBCs were also shown to induce the epithelial-mesenchymal transition (EMT) in a TNBC cell line [86]. However, as this study did not evaluate the effect of fibroblasts on luminal breast cancer cells phenotypes [86], it is unclear whether the observed induction of EMT in TNBC cells is a

subtype-specific phenomenon, or rather a general cellular response to interface-zone fibroblasts from triple-negative tumors.

In addition to enhancing the invasive potential of TNBC cells, a growing body of work indicates that CAFs may also influence the therapeutic responses of this tumor subtype. For example, fibroblast-specific secretion of the pleiotropic signaling molecule hepatocyte growth factor (HGF) has been recently shown to mediate TNBC cell resistance to EGFR tyrosine kinase inhibitors; these data offer a possible explanation as to why EGFR-over-expressing TNBCs fail to respond to drugs in this class [87]. Interactions between CAFs and stromal immune cells may also facilitate TNBC progression and impede therapeutic responses by fostering an immunosuppressive microenvironment. One study of CAF heterogeneity determined that a specific subset of CAFs ("CAF-S1," defined as $CD29^{Med}$ FAP^{Hi} [fibroblast activation protein] $FSP\text{-}1^{Low\text{-}Hi}$ [fibroblast-specific protein-1] αSMA^{Hi} [alpha-smooth muscle actin] $PDGFR\beta^{Med\text{-}Hi}$ [platelet-derived growth factor receptor beta] $CAV1^{Low}$) were enriched in the microenvironment of human TNBCs relative to other tumor subtypes, and were associated with the stromal infiltration of immunosuppressive, regulatory $FOXP3^{+}$ (forkhead box P3) T cells [88]. The CAF-S1 subpopulation also promoted the differentiation of $FOXP3^{+}$ T cells in the tumor microenvironment, and enhanced their capacity to inhibit the proliferation of pro-inflammatory effector T cells [88]. Additionally, xenograft models in which primary human monocytes were co-transplanted with TNBC or luminal cell lines revealed that CAFs in triple-negative microenvironments produce CXCL16 (chemokine C-X-C motif ligand 16), in turn recruiting both additional CAFs and immunosuppressive myeloid cells [89]. Taken together, these studies suggest that CAFs may be a viable therapeutic target in triple-negative tumors, as well as a potential biomarker of therapeutic responses. Accordingly, targeting of CAFs with the anti-fibrotic agent Perfenidone inhibited CAF-induced TNBC morphogenesis in 3D culture models, and synergistically blocked tumor growth and lung metastasis when administered in combination with doxorubicin [90].

Macrophages: Macrophages are a highly heterogeneous class of myeloid-lineage cells that function in both developmental and immune response processes [91-94]. In the context of breast cancer, however, these cells have been implicated in numerous facets of tumor progression, including the induction of angiogenesis (see below) [95, 96]; immunosuppression and tumor immune evasion [97]; and local invasion and metastasis [98-100]. Accordingly, it is unsurprising that tumor-associated macrophage (TAM) infiltration into the breast cancer microenvironment is associated with triple-negativity [101-103], and correlates with an increased risk of metastasis and reduced recurrence-free survival among these patients [101-104]. Elucidation of specific TAM-TNBC interactions that promote tumor progression warrants further study.

In addition to the effects of TAM infiltration on tumor biology, reciprocal interactions between macrophages and breast cancer cells can also exert striking alterations in macrophage phenotypes. Historically, macrophages have been classified as either M1 (pro-inflammatory, classically activated) or M2 (anti-inflammatory/immunosuppressive, alternatively activated) cells; however, this dichotomy is insufficient to account for the diversity and plasticity of macrophages *in vivo* [reviewed in 25]. In the setting of breast cancer, TAMs exhibit properties of both M1 and M2 cells, and molecularly distinct subpopulations have been identified in association with their locations relative to the frank tumor. For example, migratory, pro-metastatic “M1-like” TAMs are generally observed in perivascular regions, whereas sessile, pro-angiogenic, “M2-like” TAMs are more prevalent in hypoxic regions and at the tumor-stroma interface [105]. Interestingly, breast cancer subtypes exhibit differential abilities to “educate” macrophages toward TAM phenotypes. For example, exposure to conditioned culture medium from claudin-low, but not luminal, breast cancer cells facilitated the differentiation of peripheral blood mononuclear cells into immunosuppressive M2-like macrophages, in a mechanism dependent upon CLBC-mediated secretion of macrophage colony-stimulating factor (M-CSF) [106]. Similarly, basal-

like, but not luminal, breast cancer cells stimulated the differentiation of THP-1 monocytes into a “mixed” population of M1- and M2-like macrophages, with some cells displaying dual positivity for both M1 and M2 markers, and others exclusively expressing markers associated with a single subpopulation [107]. Further refinement of TAM phenotypes in TNBC microenvironments, as well as the prognostic and potential therapeutic implications thereof, is an important avenue for future research.

Endothelial cells: The process of angiogenesis, or the formation of new blood vessels from existing vasculature, is a critical, rate-limiting step of tumor growth and metastasis. Establishment of a tumor vascular supply occurs in a discrete step known as the “angiogenic switch,” wherein the net balance of pro- and anti-angiogenic signaling mediators favors blood vessel development [108]. Recent reports have shown that high microvessel density (number of vessels per unit area) and microvessel proliferation (number of vessels containing $Ki67^{+}$ endothelial cells) are associated with both BBCs [109, 110] and specific molecular features of basal-like tumors (e.g., CK5/6, p-cadherin, or EGFR protein expression). These data indicate that a specific subset of TNBC patients may have strong potential to benefit from anti-angiogenic therapies [109, 110].

Examination of cancer cell-endothelial interactions is crucial for better understanding how the vasculature contributes to the growth, invasion, and metastasis of TNBCs. For example, Ingthorsson and colleagues [111] recently demonstrated that primary endothelial cells derived from reduction mammoplasty tissue stimulated the growth and 3D morphogenesis of both pre-invasive and malignant TNBC organoids. Two-dimensional co-culture models were subsequently used to show that the endothelial-derived proliferative signals were soluble in nature; however, specific signaling mediators responsible for the observed phenotypes were not identified [111]. Using a similar model system, this same group also showed that reduction mammoplasty-derived endothelium could induce the epithelial-mesenchymal transition (EMT) in “stem-like” ($CD44^{hi}/CD24^{low}$) BBC cells, and that

this process could be partially reversed via inhibition of HGF signaling [112]. With respect to TNBC metastasis, Di Modica et al. [113] demonstrated that TNBC cells release exosomes containing miR-939, a microRNA molecule that inhibits translation of the endothelial cell adherens junction protein, vascular endothelial (VE)-cadherin. Notably, miR-939-mediated targeting of VE-cadherin compromised the integrity of endothelial cell-cell contacts, and facilitated TNBC cell trans-endothelial migration, a critical step in the metastatic cascade. CLBC cells have been further shown to secrete plasminogen activator inhibitor-1 (PAI-1), a mesenchymal marker of EMT that stimulates the production of chemokine (C-C motif) ligand 5 (CCL5) by endothelial cells [114]. In turn, endothelial-derived CCL5 accelerates TNBC-mediated PAI-1 secretion, and promotes CLBC cell migration, invasion, and metastasis through the formation of a positive feedback signaling loop [114]. Taken together, in light of the fact that currently available angiogenesis inhibitors do not confer a significant survival advantage to TNBC patients [115], this body of work suggests that the study of cancer cell-endothelial communication patterns may be a powerful means by which to identify novel anti-angiogenic targets for TNBC.

Little is known about the endothelium of TNBC-adjacent breast. Moreover, very little work has examined the vascular properties of normal (i.e., non-cancer-associated) mammary tissue. One study of an unspecified number of reduction mammoplasty tissue samples revealed that $CD31^+$, VE-$cadherin^+$, and $CD34^+$ microvessels are prominent features of TDLUs [116]. In another study of reduction mammoplasty tissue from 9 pre-menopausal women, Naccarato et al. [117] described different patterns of microvascular distribution and morphology in breast ducts vs. TDLUs: whereas ducts were surrounded by a relatively higher number of small, prototypical capillaries, TDLUs were encompassed by a relatively smaller number of large microvessels that were sinusoidal in shape. The functional significance of these findings in normal tissue, as well as whether similar features are also apparent in TNBC-adjacent breast, is currently unknown.

1.6. Benign and pre-malignant breast lesions: Role of microenvironment in progression to invasive disease

Over the last several decades, a spectrum of benign and pre-malignant breast disorders with varying pre-cancerous potentials have been identified and characterized. By definition, these lesions are distinct from frank breast cancers, in that the former are confined to the mammary gland *proper* and do not breach the epithelial basement membrane. In this section, the features of benign and pre-malignant growths germane to this dissertation will be briefly discussed, with emphases on: 1) their associations with invasive breast cancer risk; and 2) mechanisms by which tissue microenvironments regulate the transition from pre-invasive to malignant disease.

1.6.1. Clinical and histologic features and associated breast cancer risk

Fibrocystic change: Formerly known as “fibrocystic disease,” fibrocystic change is a heterogeneous class of common, benign disorders that are most prevalent in pre-menopausal women under the age of 50 [118]. These lesions may be proliferative (e.g., hyperplasia without atypia; intraductal papilloma) or non-proliferative (e.g., cysts) [6, 118], and are thereby associated with differential risks of invasive breast cancer. For example, two large cohort studies with median follow-up times of 15 and 17 years, respectively, demonstrated that women with non-proliferative findings were not at increased risk of breast cancer [119, 120]. In contrast, women presenting with hyperplasia without atypia had a 1.9-fold increased breast cancer risk compared to women with non-proliferative lesions [120], and a 1.88-fold increased risk relative to the expected number of breast cancer cases on the basis of Iowa SEER registry data [119]. Moreover, given that invasive breast cancer can occur co-incidentally with a benign lesion (for example, fibrocystic changes may occur

secondary to a proximal malignancy), mammographic and histopathologic evaluation of benign disorders is critical for an exclusionary diagnosis [6].

Atypical ductal hyperplasia: Atypical ductal hyperplasia (ADH) is a proliferative epithelial abnormality that is typically diagnosed as an incidental finding, accounting for only ~4% of symptomatic, non-malignant biopsies [121]. This disorder is characterized by the filling and distention of mammary ducts by a homogenous, proliferative population of dysplastic epithelial cells [119, 121], and is considered a *bona fide* pre-malignant condition because it exhibits some, but not all, features of invasive breast cancer [122]. Beginning in the mid-1980s, several studies have demonstrated that ADH is associated with an increased risk of subsequent invasive breast cancer, with a cumulative breast cancer incidence of approximately 30% after 25 years of follow-up [119-125]. However, with the exception of young age [119, 122, 126, 127], specific, uncontested demographic factors that predispose ADH patients to malignant disease have not been identified.

Ductal carcinoma in situ: Pure ductal carcinoma *in situ* (DCIS) (i.e., DCIS in the absence of coincident invasive breast cancer) accounts for 20-25% of all newly diagnosed breast cancer cases in the US, and the incidence in women under 50 years of age only continues to rise in association with screening [128]. Similar to ADH, DCIS lesions are characterized by a homogeneous-appearing population of proliferative malignant epithelial cells, with no evidence of invasion beyond the basement membrane [121]. Accordingly, there is currently no clear consensus on the specific histologic criteria that should be employed to distinguish between ADH and DCIS: some clinicians apply a 2-mm size cutoff (<2 mm and ≥2 mm indicating ADH and DCIS, respectively), whereas others enumerate the number of involved ducts apparent on biopsy sampling (involvement of <2 acinar spaces indicative of ADH) [6, 129]. Interestingly, molecular studies have revealed that both IHC-based and intrinsic subtype definitions of invasive breast cancer can also be applied to

DCIS [130-134]. However, subtype frequencies may differ between DCIS and invasive cases [130-133].

DCIS is a known risk factor for invasive breast cancer; however, knowledge regarding the extent of this risk has shifted over time. For much of the 20th century, women diagnosed with DCIS were nearly universally treated with mastectomy [135]. However, given reports that lumpectomy and radiation were equally effective treatment strategies for invasive breast cancers, mastectomy rates for DCIS began to slowly decline beginning in ~1980 [135]. According to current estimates, 25-50% of DCIS cases will recur as invasive cancers even in the absence of treatment (i.e., with biopsy alone), with latency periods of up to or greater than 40 years [136, 137]. However, clinically validated biomarkers and clinicopathologic features that predict DCIS progression to malignant disease remain elusive [138-140], indicating that the regulation of the invasive transition is an important area of future research (see below).

1.6.2. Natural history and progression to invasive disease

The prevailing model of the pre-malignant to invasive breast cancer transition describes a stepwise, evolutionary continuum that was first conceptualized over 100 years ago [reviewed in 141]. First, initiating mutations within a luminal epithelial cell are believed to give rise to flat epithelial atypia, a disorder in which minimally proliferative, cytologically atypical luminal cells dilate the walls of the affected TDLU. The acquisition of growth-promoting mutations, together with molecular alterations such as loss of heterozygosity (LOH) at hotspot tumor suppressor loci [141], is then believed to promote the development of ADH. In turn, a series of additional genetic and molecular changes (e.g., gene amplification [142]; further LOH events [143]) enables progression to DCIS, and potentially ultimately to invasive disease [141]. This clonal, linear model is supported by substantial evidence demonstrating that specific gene expression, histologic, and mutation patterns can

be detected in both pre-invasive and malignant breast tissue specimens from the same individual [144-148]. Several studies have similarly reported that transcriptional signatures unique to each stage of tumor progression are lacking, suggesting that the gene expression patterns required in the setting of malignancy are established at early stages of tumor development [139-141]. These observations, coupled with the inability to use molecular tumor data to identify DCIS lesions at risk of progression to malignant breast cancer, suggest that other factors, such as tissue microenvironments, are important regulators of the benign-to-invasive transition.

No published reports have described microenvironmental features of flat epithelial atypia, and very little is known about those of ADH tissue. One study revealed that activated fibroblasts (defined as positive for both α-SMA and FSP-1) are present in the microenvironment of human ADH tissue (ADH-associated fibroblasts; AHFs), and possess an intermediate phenotype between that of normal- and cancer-associated fibroblasts [149]. These cells were also shown to enhance the proliferation of MCF-7 luminal breast cancer cells in transwell co-culture and tumor xenograft assays, in a mechanism dependent upon down-regulation of miR-200/c [149]. Whether AHFs can also promote growth of ADH epithelium and/or TNBC cells should be explored. Interestingly, an additional study demonstrated that HGF secretion was significantly up-regulated in co-culture models of basal-like ADH epithelium and fibroblasts, suggesting that HGF/cMET signaling is important in both pre-malignant [150] and invasive (see above) stages of BBC progression.

In contrast, the role of the microenvironment in the regulation of the DCIS-to-invasive breast cancer transition has been more extensively evaluated. Broadly, recent studies have identified substantial genomic, phenotypic, and epigenetic changes between normal microenvironmental cells and their DCIS- and/or invasive cancer-associated counterparts, suggesting that these molecular alterations may promote progression to malignant disease [151-154]. Current research in this area has focused predominantly on fibroblasts and

myoepithelial cells, which have been shown to promote and inhibit the invasive transition, respectively. For example, Hu et al. used xenograft models to demonstrate that co-injection of a human DCIS cell line with either normal or cancer-associated fibroblasts promoted progression to invasive disease [155], potentially due to activation of cyclooxygenase-2 (COX-2), a negative prognostic indicator in breast cancer [156]. Remarkably, the stimulatory effect of fibroblasts on DCIS xenograft invasion was abrogated by the additional injection of human myoepithelial cells [155]. Interestingly, the tumor-suppressive functions of this cell type have also been reported in other studies. For instance, normal myoepithelium constitutively expresses a number of proteinase inhibitors that both suppress cancer cell proliferation and prevent epithelial cell-mediated degradation of the basement membrane [152, 154, 157]. In fact, downregulation of these markers in DCIS-associated myoepithelium may promote the invasive transition by a variety of mechanisms, including: 1) activation of transforming growth factor beta (TGFβ) signaling; 2) reduced adhesion of myoepithelial cells to ECM proteins; and 3) increased secretion of matrix-degrading enzymes such as matrix metalloproteinases (MMPs) [154, 158, 159]. In sum, this body of work indicates that molecular studies of myoepithelial cells and/or fibroblasts in DCIS tissue samples may aid in the identification of patients at risk of progression from benign to invasive breast cancer. Future efforts to identify specific microenvironmental signaling mediators that may be relevant to this transition are paramount (see also, Chapter 2.

1.7. Objectives and significance of this dissertation research

The diverse components of the breast cancer microenvironment are critical mediators of tumor initiation and progression. However, the molecular and histologic characteristics of tumor microenvironments as they relate to breast cancer subtypes remain

understudied. Therefore, the overarching goal of this research was to establish a foundation for understanding how tissue microenvironments vary in association with the subtype of the corresponding tumor, with a focus on clinically intractable TNBCs. *In vitro*, murine, and human tissue models were leveraged to profile diverse stromal-epithelial interactions in both pre-invasive and malignant TNBCs. Utilization of different models highlights the strengths of each system for studying particular endpoints relevant to TNBC microenvironments. Moreover, studying a variety of stromal cell types (fibroblasts, macrophages, and endothelial cells) underscores the complexity of the breast microenvironment.

The primary objective of this work was to identify specific, microenvironmental signaling mediators with potential to influence TNBC initiation and progression (Chapters 2 [fibroblasts] and 3 [macrophages]). In addition, to directly address the paucity of work relating to the vascular features of extra-tumoral microenvironments, Chapter 4 describes a novel digital algorithm that can be used to link vascular content and patterns of endothelial cell marker distribution in cancer-adjacent, histologically benign human breast tissue to epidemiologic data such as tumor subtype and known breast cancer risk factors. This work is significant because it reveals novel stromal-epithelial interactions in TNBCs. Molecular and histologic features unique to TNBC microenvironments may ultimately be leveraged as therapeutic targets for this tumor subtype.

1.8. Figures

Figure 1.1. Normal adult mammary gland anatomy and histology

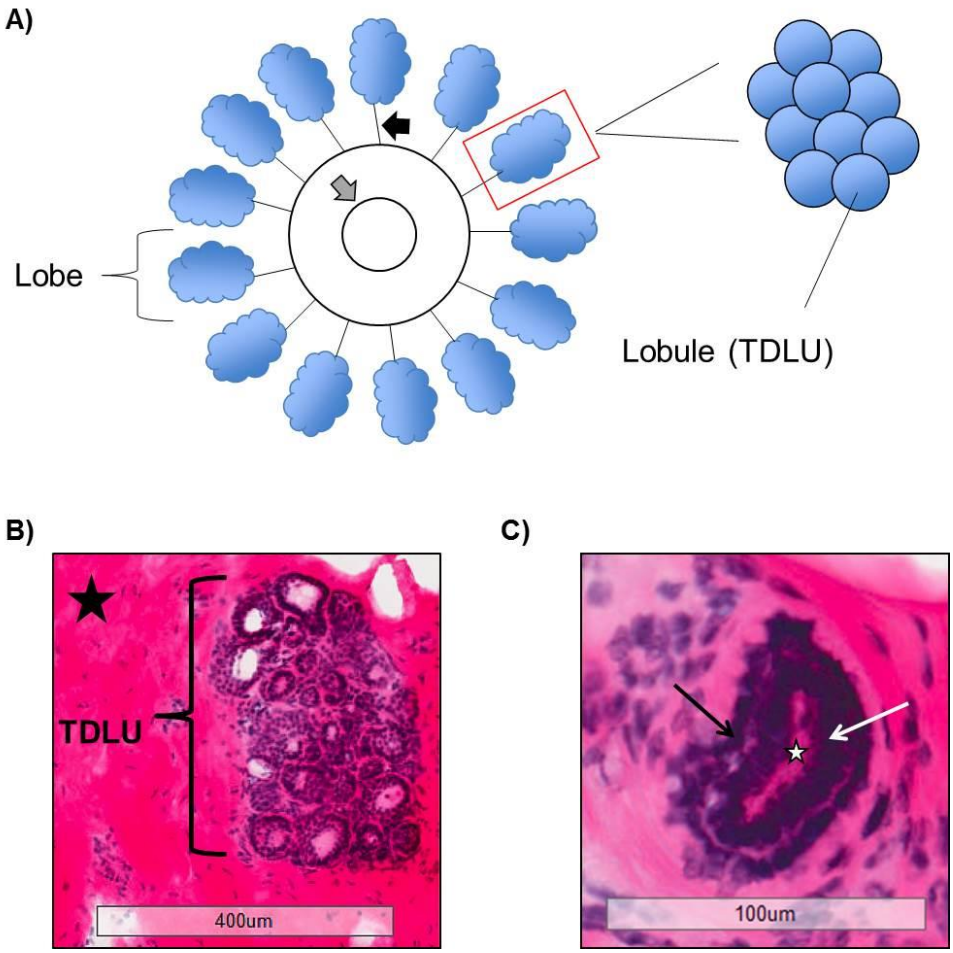

A) Schematic representation of mammary gland gross anatomy in adult women. The mammary gland consists of secretory lobes that are connected to the nipple (grey arrow) via lactiferous ducts (black arrow). Lobes are further composed of 20-40 lobules (TDLUs), in which the majority of breast cancers develop. **B)** Human TDLU stained with hematoxylin and eosin (H&E). Star indicates connective tissue stromal component. Scale bar = 400 μm. **C)** Cross-section of human mammary epithelium stained with H&E. White arrow indicates luminal epithelial cells; black arrow indicates myoepithelial cells. Star indicates location of lumen. Scale bar = 100 μm. Not pictured: basement membrane.

Figure 1.2. *In vitro* culture models for studies of stromal-epithelial interactions in breast

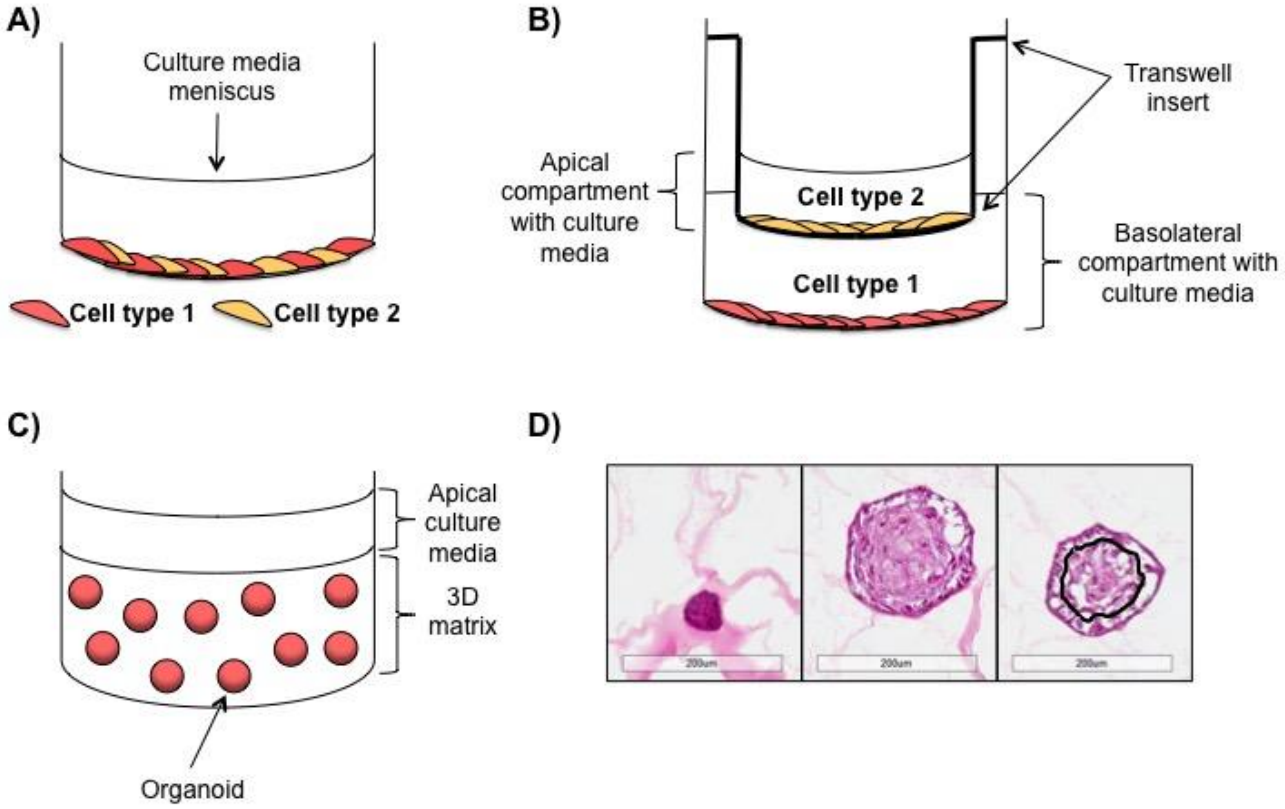

A) Schematic of “direct” co-culture model wherein two cell types are grown together in the same tissue culture well. **B)** Schematic of “transwell” co-culture model. Although the two cell types are not in direct physical contact, they are separated by a porous physical barrier and can still communicate via soluble signaling mediators. **C)** Schematic of “organoid” culture. Epithelial cells are suspended in a three-dimensional matrix and differentiate into multi-cellular structures that recapitulate *in vivo* properties of the mammary gland. **D)** Cross-sections of mammary epithelial organoids. Organoids begin as small, multi-cellular structures without a visible lumen (left). As they mature, organoids increase in size and begin to undergo apoptosis-mediated cavitation (lumen formation; middle). Cell proliferation will cease once the organoid reaches its mature, final size (right). Additionally, all cells in the center of the organoid will apoptose (contained within the black line), leaving only a single outer layer of epithelial cells. Scale bar = 200 μm.

CHAPTER 2

p53-DEPENDENT STROMAL-EPITHELIAL INTERACTIONS INDUCE MORPHOLOGIC CHANGES IN PRE-MALIGNANT BREAST THAT CORRELATE WITH UNIQUE PATTERNS OF GENE EXPRESSION

2.1. Overview

Basal-like and luminal breast cancers exhibit subtype-specific transcriptional and phenotypic responses to stroma, but little is known about how stromal-epithelial interactions evolve during carcinogenesis. The vast majority of basal-like breast cancers (BBCs) also harbor loss-of-function mutations in the tumor suppressor gene, *TP53* (p53), but the manner in which p53 deficiency *per se* alters stromal-epithelial interactions in BBC remains unexplored. To address these knowledge gaps, we leveraged the MCF10 progression series of breast cell lines to engineer a longitudinal, tissue-contextualized model of p53-deficient, pre-malignant breast. An optical coherence tomography-based imaging platform, together with gene expression microarray data, identified novel p53-dependent morphogenetic responses to stroma that correlated with unique transcriptional changes. p53-dependent stromal-epithelial interactions in benign and pre-malignant BBC may hold promise as biomarkers of invasive cancer risk and/or targets for BBC prevention.

2.2. Introduction

Breast carcinogenesis occurs in a step-wise fashion, with flat epithelial atypia (FEA), atypical ductal hyperplasia (ADH), and ductal carcinoma *in situ* (DCIS) recognized as *bona fide*, non-obligate precursors to invasive and metastatic disease [141, 160]. However, decades of work have failed to identify tumor-intrinsic features that robustly predict progression to invasive cancer, suggesting a strong role for the tumor microenvironment in mediating the benign to malignant transition [134, 138-142, 160]. However, due to: 1) the cross-sectional nature of previous epidemiologic studies of stromal tissue; 2) the reliance of these studies on samples from patients with concurrent DCIS and invasive breast cancer; and 3) the extensive genomic similarities between *in situ* and invasive microenvironments [151, 152, 155, 161], little is known about the evolution of stromal-epithelial interactions during carcinogenesis, particularly during early stages of disease.

Breast cancer subtypes exhibit distinct interactions with their microenvironments, with stroma inducing more extensive gene expression changes in basal-like (BBC) relative to luminal breast cancers [85]. BBCs also exhibit unique tumor-intrinsic features, including nearly universal loss-of-function (nonsense and frameshift) mutations in the tumor suppressor gene, *TP53* (p53) [19, 43, 162]. As many previous studies of BBC microenvironments have utilized a mix of p53-wild-type and -mutant/deficient cell lines [85, 150], characterizing stromal-epithelial interactions in the context of this important genetic defect is crucial for better understanding the biology of this tumor subtype.

We hypothesized that epithelial p53 status modifies stromal-epithelial interactions during BBC carcinogenesis. To test this hypothesis, we utilized RNA interference to engineer p53-deficient MCF10 series cell lines. The MCF10 progression series is an isogenic collection of cell lines that recapitulates features of pre-invasive, basal-like breast lesions, including benign fibrocystic change (MCF10A), ADH (MCF10AT1), and DCIS

(MCF10DCIS.com, herein referred to as MCF10DCIS), in xenograft models. These isogenic lines were utilized in three-dimensional (3D) co-culture assays, and evaluated with both gene expression microarrays and an innovative quantitative imaging platform. The resulting longitudinal, tissue-contextualized models demonstrate that p53-dependent stromal-epithelial interactions during BBC carcinogenesis evoke differential morphogenetic phenotypes in pre-malignant breast cells that correlate with unique transcriptional responses.

2.3. Materials and methods

2.3.1. Cell lines

The isogenic MCF10 progression series of pre-malignant breast cell lines was obtained from the Barbara Ann Karmanos Cancer Institute (Detroit, MI). Cells were maintained in Dulbecco's modified Eagle's medium/F12 nutrient mix (DMEM/F12, Gibco, Life Technologies, Carlsbad, CA), supplemented with 5% horse serum (Gibco), 20 ng/mL epidermal growth factor (Invitrogen, Life Technologies), 0.5 µg/mL hydrocortisone (Sigma-Aldrich, St. Louis, MO), 10 µg/mL insulin (Gibco), and 0.1 µg/mL cholera toxin (Millipore Sigma, Burlington MA). Similar to previous studies, we also utilized an hTERT-immortalized reduction mammoplasty fibroblast (RMF) cell line, a kind gift from Charlotte Kuperwasser, PhD (Tufts University Medical Center, Boston, MA), to circumvent the technical challenges (e.g., cell senescence) and substantial genomic heterogeneity associated with the use of primary human fibroblasts [85, 150]. RMFs were maintained in RPMI1640 medium supplemented with 10% FBS prior to use in 3D cultures (see below). All cells were grown in a humidified incubator at 37°C and 5% CO_2, and were propagated for <6 months (breast cells) or <1 month (RMFs) prior to use in experiments.

2.3.2. Endogenous TP53 *sequencing and generation of p53-deficient MCF10 cell line series*

The endogenous *TP53* coding sequence in parent MCF10A, MCF10AT1, and MCF10DCIS lines was sequenced prior to generation of p53-deficient and control lines. RNA was reverse-transcribed (RT^2 Reverse Transcription Kit, QIAGEN, Valencia, CA), and the resulting cDNA was used to PCR-amplify (Phusion Polymerase, New England BioLabs, Ipswich, MA) the *TP53* coding sequence with primers specific to canonical human *TP53* (F: 5'-ATGGAGGAGCCGCAGTCAGATC-3'; R: 5'-TCAGTCTGAGTCAGGCCCTTCTG-3'; Eurofins Genomics, Louisville, KY). Samples were electrophoresed on and excised from a 0.8% agarose gel (QIAquick Gel Extraction Kit, QIAGEN), and an A-tailing reaction was performed on the purified blunt-ended products (Taq DNA polymerase with ThermoPol Buffer, New England Biolabs). The resulting DNA was ligated into the pGEM-T Easy TA cloning vector and transformed into JM109 competent cells (Promega, Madison, WI) according to the manufacturer's instructions. Following blue-white colony selection, plasmid DNA from 4-5 colonies per cell line was purified (QIAprep Plasmid Miniprep Kit, QIAGEN) and sequenced by GeneWiz using SP7 and U6 primers. Sequences were analyzed with ApE software.

shRNA plasmids used to construct the p53-deficient MCF10 cell line series were generated by Masutomi and colleagues [163] and purchased from Addgene (p53 knock-down [-sh:p53] lines: pMKO.1-puro-p53 shRNA 2 [Addgene #10672]; GFP knock-down [-sh:GFP] control lines: pMKO.1-puro-GFP shRNA [Addgene #10675]). Plasmids were transfected into the Phoenix-AMPHO packaging cell line (ATCC, Manassas, VA) using Lipofectamine LTX (Invitrogen, Carlsbad, CA) according to the manufacturers' instructions, and the virus-containing supernatants were harvested and directly applied to each of the 3 parent lines in the MCF10 series. Stable cell populations were established by selection in 1 μg/mL puromycin for 14 days.

2.3.3. Calculation of population doubling time

Cells were plated at a density of 1 x 10^5 cells per 60-mm dish and were harvested and enumerated every 24 hours for 4 days. Log-phase cell growth was with the regression equation, $\ln(A_t) = \ln(A_0) + kt$, wherein "A_t" represents the number of cells present at time "t"; "A_0" represents the initial number of cells; and "k" represents the first-order rate constant of cell growth with units of $time^{-1}$ [150]. For each cell line, k was computed in each of 3 independent experiments, and population doubling time (PDT) was calculated as follows: $PDT = \frac{\ln(2)}{k}$.

2.3.4. 2D culture RNA isolation and quantitative PCR (qRT-PCR)

Total RNA was extracted (RNeasy Mini kit, QIAGEN) and reverse-transcribed (RT^2 Reverse Transcription Kit, QIAGEN) according to the manufacturers' instructions. Gene expression was quantitated with exon-spanning TaqMan Gene Expression Assays (Applied Biosystems, Foster City, CA) using an ABI 7900HT Fast real-time PCR machine (Invitrogen) using the SsoAdvanced Universal Probes Supermix (Bio-Rad, Hercules, CA). Normalization to *GAPDH* was performed using the ΔΔCt method.

2.3.5. 3D culture conditions

Cells were suspended in a biologically derived matrix comprised of 50% phenol red-free Matrigel (#356237; Corning, Corning, NY) and 50% rat-tail collagen I (#354236; Corning) diluted to a final concentration of 1 mg/mL as previously described [68, 71, 150, 164]. Suspended cells were then seeded into tissue culture plates pre-coated with the same matrix, and growth medium was dispensed to the apical side of each culture after 30-60 minutes. Co-cultures were maintained in MCF10 series growth medium (DMEM/F12), as we have previously demonstrated that RMF doubling times in this medium are similar to those

observed in RPMI1640 [85, 150]. RMF mono-cultures maintained in DMEM/F12 were used as normalization controls for gene expression microarray analyses (see below). Corresponding mono- and co-cultures were constructed with the same total starting cell number (rather than the same starting number of breast cells) to reduce the potential for nutrient deprivation in co-cultures (**Table 2.1**). Cultures were refreshed every 2-3 days and were maintained for 14 days, as both MCF10A and MCF10DCIS organoids cease log-phase growth by this time point [68].

2.3.6. Optical coherence tomography (OCT)-based morphology assay

Organoid morphology was quantitated using optical coherence tomography (OCT), a method of "optical histology" sensitive to changes in signaling mediator activity, toxicant exposure, and cell-cell and cell-matrix interactions [68, 69, 71, 150]. We particularly focused on organoid "asphericity," a unitless morphologic metric defined as the ratio of the volume of a perfect sphere with the same surface area as a given organoid to the volume of the organoid; a value of 1 is indicative of a perfectly spherical structure [68]. This metric has been described to reflect cell invasive potential (i.e., local invasion) [68], and the asphericity of MCF10 series control organoids increases with progression to malignancy (**Figure 2.1A**).

The OCT system used in the present study has been described in detail previously, and consists of a titanium-sapphire laser with a central wavelength and bandwidth of 800 nm and 120 nm, respectively [68]. Spectral images (200 frames per sample) were collected using a custom spectrometer with a Dalsa Piranha line scan CCD camera operated at 2-4 kHz. As described in previous studies, we used custom MATLAB scripts to quantitate organoid asphericity [68, 150]. Briefly, individual organoids were manually identified within each image stack, and an intensity threshold was selected for each region of interest to distinguish the included organoid from the surrounding matrix (background). Computation of organoid morphology was then performed in an automated fashion. To avoid selection bias,

organoids that 1) did not overlap with adjacent structures; 2) were not in close proximity to the edge of an image frame or the apical surface of the culture; and 3) could be adequately distinguished from background were analyzed. For each independent experiment, all cultures were grown, imaged, and analyzed simultaneously. An average of ~30-45 organoids across 2-3 independent experiments was analyzed for each culture condition, and all 3D organoid renderings shown in this document are representative. Organoids generated for OCT imaging were not utilized in microarray experiments (see below) to circumvent the possible transient effects of imaging on gene expression.

2.3.7. 3D culture RNA isolation

Cultures were rinsed with cold PBS and technical replicates (2 cultures for each of 2 independent experiments) were transferred into a single tube containing 800 µL of Cell Recovery Solution (#354253; Corning) on ice. Each well was rinsed with an additional 1.0 mL of Cell Recovery Solution to ensure complete transfer of the sample. Phenol-chloroform RNA extraction was then performed using QIAzol lysis reagent (QIAGEN) according to the manufacturer's instructions, with modifications: following centrifugal separation of the organic and aqueous phases, the aqueous phase was mixed with 100% ethanol at a ratio of 1:1 and applied to a QIAGEN RNeasy column according to the manufacturer's instructions. RNA concentrations were determined using a NanoDrop 2000 Spectrophotometer (Thermo Fisher Scientific, Waltham, MA). Samples were further purified with the RNA Clean and Concentrator Kit (Zymo Research, Irvine, CA) as needed.

2.3.8. Whole genome microarrays

RNA from 3D cultures was isolated and quantified as described above, and sample quality was determined using the Agilent Tape Station (Santa Clara, CA). All samples had

RNA integrity numbers of ≥7. RNA samples were labeled and amplified using the Agilent Low Input Two-Color, QuickAmp Labeling kit (#5190-2306) according to the manufacturer's instructions. Cy-5-labeled cDNAs were generated from all experimental samples, and reference RNA (Stratagene Universal Human Reference spiked 1:1000 with MCF-7 RNA and 1:1000 ME16C RNA to increase expression of breast cancer genes) was labeled with Cy-3. All samples were run on Agilent human 4x44K v2 whole genome microarrays (#G4845A). For RMF-only samples, RNA from 4 wells (2 wells from each of 2 independent experiments) was pooled, concentrated, and applied to 4 microarrays due to low sample concentrations.

2.3.9. Microarray data normalization and analysis

Microarray data were Lowess-normalized and probes with >80% good data (signal >10 dpi in both channels) were selected for further analysis. During data pre-processing, we: 1) eliminated probes without corresponding ENTREZ Gene IDs; 2) collapsed duplicate probes corresponding to the same ENTREZ Gene ID by averaging; and 3) imputed missing data using the k-nearest neighbors' imputation with k = 10. Unless otherwise specified, we also excluded genes that did not have at least a two-fold deviation from the mean expression in at least one sample. For mono-culture analysis, a pre-processed dataset consisting only of epithelial mono-culture samples was constructed; RMF mono-cultures were excluded from this dataset because they were only utilized for co-culture data normalization (see below). Mono-culture gene expression analysis was conducted using significance analysis of microarrays (SAM) procedures as indicated in the text.

For co-culture data, we first used the method of Buess et al. [165] to normalize co-cultures to the corresponding mono-cultures grown under identical conditions [85, 150]. This expression deconvolution approach estimates the percentage of cancer cells and fibroblasts in each co-culture, normalizes the resulting data for additive effects in the mixed-

composition co-culture sample, and calculates a coefficient of interaction ("I") for each gene by determining the ratio of observed to expected co-culture gene expression. We used this approach to generate an I-matrix consisting of interaction coefficients for each gene in all co-cultures, which can be analyzed in an identical manner to "conventional" (i.e., non-co-culture-normalized) microarray data. Estimation of the proportion of breast epithelial cells revealed that breast epithelial cells comprised >90% of cells in each co-culture (**data not shown**), indicating that RMF contributions to signaling were ostensibly null at sample harvest. We confirmed this result by correlating co-culture gene expression data with that of the corresponding breast epithelial monoculture (**data not shown**). Therefore, co-culture gene expression data were analyzed in a manner analogous to that of mono-culture data: A pre-processed dataset was created containing only gene expression data from co-culture samples. The expression of each gene in replicate knock-down co-culture samples was normalized to the average expression of that gene across the corresponding control co-culture samples, and the resulting dataset was median centered and analyzed via SAM as indicated in the text. Gene lists were functionally annotated with DAVID Bioinformatics Resources, version 6.8 (https://david.ncifcrf.gov).

2.3.10. Statistics

All statistical analyses were performed with GraphPad Prism version 6.0 (GraphPad Inc., La Jolla, CA). Data were analyzed using the two-tailed unpaired student's t-test or two-way ANOVA with Tukey's multiple comparison test as appropriate. Error bars indicate the mean $\pm$ standard error of the mean (SEM), and $p<0.05$ was considered statistically significant.

2.4. Results

2.4.1. Phenotypic characterization of p53-deficient MCF10 series

To study the effects of p53 deficiency in pre-malignant BBC cells, a p53-targeting shRNA construct (herein referred to as, "-sh:p53") was stably expressed in MCF10A, MCF10AT1, and MCF10DCIS cells; the 3 parent lines were confirmed by our laboratory to express wild-type *TP53* (**data not shown**). Stable lines expressing a GFP-targeting shRNA construct ("-sh:GFP") were also generated as negative controls. qRT-PCR analysis indicated that a >80% reduction in p53 expression was achieved for each knock-down cell line in our panel (**Figure 2.1B**; $p<0.0001$ sh:p53 vs. sh:GFP for each isogenic cell line pair). Additionally, growth curve analyses of cells grown on plastic revealed that population doubling times did not significantly differ between the corresponding -sh:GFP and -sh:p53 isogenic pairs (e.g., MCF10A-sh:GFP vs. MCF10A-sh:p53; **data not shown**). Moreover, -sh:p53, but not –sh:GFP, cells exhibited the ability to survive and grow in the absence of serum (**data not shown**), consistent with expected results.

2.4.2. Contextual responses of pre-malignant BBC cells to p53 deficiency

We employed 3D morphogenesis assays to track the evolution of epithelial morphogenesis with pre-invasive BBC progression and in response to epithelial p53 deficiency. Epithelial cells grown in a 1:1 mixture of Matrigel and collagen I differentiate into 3D, multicellular organoids that recapitulate the *in vivo* structure of mammary gland acini, enabling studies of both physiologic and pathologic processes in a tissue-relevant context [65, 150]. Organoid morphogenesis, which requires coordination of cell proliferation, apoptosis, and migration [166], was quantitated with OCT imaging. To characterize the morphogenetic responses of pre-invasive BBC cells to p53 deficiency, OCT-based quantitation of asphericity was performed on mono-cultures after 2 weeks of culture (**Figure**

2.2A-C). We observed that benign MCF10A organoids exhibited significantly increased asphericity in response to p53 expression deficits ($p = 0.0023$), but that the morphologic characteristics of MCF10AT1 and MCF10DCIS organoids were independent of p53 status.

We next determined whether the morphologic responses (or lack thereof) of each cell line to p53-knock-down correlated with unique patterns of gene expression. First, a 2-class SAM analysis of the top ~10% most variable genes across mono-culture samples (all 3 -sh:p53 samples vs. all 3 -sh:GFP controls) revealed that p53 deficiency did not elicit a common transcriptional response; in fact, gene expression patterns across the 6 cell lines were highly variable (**data not shown**). In light of this result, we next sought to understand how transcriptional responses to p53 deficiency varied across cell lines. The expression of each gene in replicate -sh:p53 mono-culture samples was normalized to the average expression of that gene across the corresponding -sh:GFP control samples, and a multi-class SAM analysis on the resulting data set identified 47 genes that were significantly differentially regulated among the three p53-knock-down cell lines (FDR = 10.02%).

Previous work in our laboratory has demonstrated that stromal cells induce broad transcriptional changes in cancer cells [85, 150]. Therefore, we considered that cell-line specific responses to p53 deficiency may also depend upon microenvironmental context. Each line in the MCF10 series was co-cultured with fibroblasts (RMFs) at a ratio of 1:1, and microarray analyses were performed after 2 weeks. To facilitate comparisons with mono-cultures, each gene in replicate -sh:p53 co-culture samples was normalized to the average expression of that gene across the corresponding -sh:GFP co-culture controls. A multi-class SAM on the resulting normalized data set identified 69 genes that were significantly differentially regulated among p53-deficient co-cultures (FDR = 9.50%). The 69 genes from this list, as well as the 47 genes differentially expressed among p53-knock-down monocultures, are presented in a single heat map (**Figure 2.3**). This expression map shows that transcriptional responses to p53 deficiency are contextual, differing both by cell line

(stage of disease) and according to the presence or absence of paracrine signals from stroma.

One group of genes in which we were particularly interested was up-regulated in MCF10A-sh:p53 mono-cultures relative to the remaining culture conditions (grey bar in **Figure 2.3**). These genes are nearly uniformly down-regulated with progression both in the presence and absence of stroma; hence, their dysregulation may have potent effects on charting the natural history of a p53-deficient BBC. In particular, we noted that *ATF7IP*, a binding partner of the transcriptional repressor *MBD1*, was present in this cluster, potentially indicating that a more transcriptionally primed or active state is induced with progression and in response to fibroblasts.

A second gene cluster of interest was that for which expression was generally highest in MCF10DCIS-sh:p53 co-cultures compared to the remaining culture conditions (black bar in **Figure 2.3**). In the context of p53 deficiency, these genes may promote the pre-malignant to invasive BBC transition [151]. Three chaperone or DNA repair genes were present in this cluster (*DNAJ4B*, *C1GALT1C1*, and *IPPK*), suggesting that a general stress response may be induced in p53-deficient MCF10DCIS co-cultures. Up-regulation of *IPPK* may also confer a survival advantage in these cells [167]. In addition, two genes in this cluster, including *MMP23* and *DOCK1*, have been previously implicated as poor prognostic markers in different cancers: *MMP23* expression in melanoma is associated with deficits in anti-tumor immune function and poor responses to immunotherapies [168], whereas high *DOCK1* expression correlates with poor survival in BBC and mediates $HER2^+$ breast cancer metastatic progression [169]. Finally, we identified the pseudogene *CRYBB2PS1* immediately outside this cluster. This pseudogene is homologous to the protein-coding gene *CRYBB2*, the latter of which is linked to race-associated disparities in breast cancer outcomes [170-172]. This gene was strongly down-regulated in MCF10A-sh:p53 cells

relative to nearly all other culture conditions, but was less robustly upregulated in MCF10DCIS-sh:p53 cells in response to stroma.

2.4.3. p53 deficiency accelerates morphologic responses of pre-invasive BBC cells to fibroblast co-culture

Having established that the genomic responses of benign breast cells to p53 deficiency change according to the presence of microenvironmental signals, we next explored whether stromal context also elicits phenotypic changes in cells. OCT-based asphericity analyses were performed on co-cultures after 2 weeks of culture. Asphericity of acini in co-culture was compared to that of organoids in the corresponding epithelial mono-culture. Organoid asphericity in response to co-culture is presented in **Figure 2.4**. The morphologies of both p53-deficient and -sufficient MCF10DCIS organoids were independent of stroma-derived signals (**Figure 2.4**, **right**), but fibroblasts did exert morphologic effects on acini at earlier stages of pre-malignancy. Among the control cell lines, fibroblasts significantly increased the asphericity of MCF10AT1-sh:GFP organoids ($p = 0.0144$ vs. MCF10AT1-sh:GFP mono-culture; **Figure 2.4**, **center**). In p53 deficient cells, in contrast, fibroblast-induced increases in organoid asphericity were observed in both MCF10A-sh:p53 ($p = 0.0070$ vs. MCF10A-sh:p53 mono-culture; **Figure 2.4**, **left**) and MCF10AT1-sh:p53 ($p<0.0001$ vs. MCF10AT1-sh:p53 mono-culture; **Figure 2.4**, **center**) cultures. These data indicate that stromal fibroblasts alter the morphologic features of both p53-sufficient and -deficient breast epithelial cells at early stages of pre-malignancy, but that morphogenetic changes are accelerated in the setting of p53 deficiency.

2.4.4. p53-dependent stromal-epithelial interactions are cell line-specific

Given that the timing of morphologic responses to co-culture was dependent upon epithelial p53 status, we sought to further characterize p53-dependent stromal-epithelial

interactions across the three cell lines. Each gene in replicate -sh:p53 mono-culture samples was normalized to the average expression of that gene across the corresponding mono-culture controls, and each gene in replicate -sh:p53 co-culture samples was normalized to the average expression of that gene across the corresponding co-culture controls. A 2-class SAM on the resulting normalized dataset (normalized knock-down mono-cultures vs. normalized knock-down co-cultures) identified only 7 genes that were significantly changed in p53-deficient cells in response to co-culture; these genes represent a common response to stroma shared by all p53-deficient cell lines (FDR = 12.2%; **data not shown**). Using the same method, we performed this analysis for each isogenic cell line pair in isolation and visualized the 3 resulting lists of significant genes with a single heat map (**Figure 2.5**). This heat map represents the unique p53-dependent responses of each cell line to co-culture. The broadest range of expression differences was observed in co-cultured vs. mono-cultured MCF10DCIS-sh:p53 organoids. Notably, 21 genes associated with phosphoprotein signaling were upregulated in MCF10DCIS-sh:p53 co-cultures (**Table 2.2**; black bar in **Figure 2.5** shows all genes upregulated in co-cultured MCF10DCIS-sh:p53 cells), suggesting activation of a diverse array of pathways in response to stroma. Additionally, consistent with previous reports demonstrating that fibroblasts promote the *in situ* to invasive breast cancer transition [155], three genes associated with metalloproteinase activity (*MMP23B*, *YME1L1*, *TMEM27*) were upregulated in MCF10DCIS-sh:p53 co-cultures compared to mono-cultures. Furthermore, in agreement with our previous finding that stroma up-regulates inflammatory and immune response genes in invasive BBCs [85], we noted that the pro-inflammatory interleukin receptor *IL12RB1* was also induced in MCF10DCIS-sh:p53 co-cultures. Down-regulated genes in p53-deficient MCF10DCIS co-cultures (grey bar in **Figure 2.5**) included those associated with cell proliferation, differentiation, and apoptosis (*POLI*, *MRPS30*, *ETS2*, *ETV4*, *NKAP*, *GDF7*, *MAP2K7*, and

MEGF8). Taken together, these results imply that p53 deficiency in DCIS may accelerate the stroma-induced transition from benign to malignant disease.

2.5. Discussion

Mutations in epithelial cells undoubtedly play indispensible roles in breast carcinogenesis, but the importance of stroma in tumor development is increasingly recognized. Dramatic gene expression changes occur in numerous stromal cell populations during progression to malignant disease [151], and pre-invasive breast stroma exhibits extensive genomic overlap with the microenvironment of malignant carcinomas [161, 173]. However, carcinogenesis is an evolutionary process that requires complementary input from both epithelium and stroma [85, 150], and it is important to understand how specific communication patterns change throughout the course of tumor development, particularly in the context of breast cancer subtypes. We previously used co-culture models to demonstrate that coordinated signaling responses occur in both stromal and epithelial cells during malignant BBC progression [150]. Herein, we build upon this work by elucidating how tissue-contextualized stromal-epithelial interactions are altered in the context of a genetic defect (p53 loss) with clinical relevance to this tumor subtype.

Three-dimensional organoid morphogenesis requires a coordinated balance of cell proliferation, apoptosis, and migration [166]. Previous 3D culture-based studies have relied upon integration of multiple histologic assays (e.g., BrdU, TUNEL, and immunohistochemical staining) to characterize these processes [64, 174, 175]. However, a general limitation to this approach is that histology is subject to selection bias, and multiple sections or microscopic fields must be analyzed per sample to confidently assess changes in phenotype or protein expression. In contrast, our OCT-based asphericity assay was able to capture the

net result of multiple cellular processes across individual organoids in a single metric. Organoid volume was also measured in this study as a more direct proxy of cell proliferation (**data not shown**), and changes in volume tracked closely with trends in asphericity. Moreover, we have previously used OCT to quantitate the intracellular dynamics of organoid cultures in response to toxicants, exogenous signaling mediators, and tissue culture composition [68, 69, 71, 150]; hence, in the present study, we probed novel, contextual cell-cell interactions with a well-validated system. In our mono-culture experiments, benign breast epithelium (MCF10A) was the only cell type to exhibit morphologic responses to p53 deficiency; in contrast, the increasingly aspherical morphologies of MCF10AT1 and MCF10DCIS organoids were independent of p53 status. Nevertheless, the transcriptional responses to p53 loss did vary among all 3 cell types, suggesting that the specific point at which p53 is mutated/lost in human BBCs has potential to influence the natural history of a given tumor.

More diverse changes in organoid asphericity were seen in co-culture, which further depended upon epithelial p53 status. Fibroblast-induced morphologic changes initially observed in p53-sufficient ADH acini (MCF10AT1-sh:GFP) were accelerated in the context of p53 deficiency, first manifesting at the benign stage (MCF10A-sh:p53). Although prior research in this area has not considered the p53 status of epithelial cells, our results differ from those in previous reports. Sadlonova et al. demonstrated that normal breast-associated fibroblasts, but not cancer-associated breast fibroblasts, inhibited the proliferation of MCF10AT1 organoids [174, 175]. However, the discrepancies between these studies and the present report may reflect methodologic differences, highlighting that co-culture conditions such as cell ratios; matrix composition and culture construction (cells grown on top of a matrix layer vs. embedded within); and the character and source of fibroblasts (immortalized vs. primary; normal vs. cancer-associated) are important considerations for future research.

Compared to a previous study of fibroblast-MCF10 series interactions [150], the present study identified far fewer transcriptional changes in epithelial cells in response to stroma. The relatively limited gene expression changes identified herein may have arisen due to the generally inhibitory effect of basement membrane proteins on cell signaling in 3D cultures [176, 177]. Alternatively, methodologic consequences may be considered. Herein, cells were embedded within a semi-solid matrix that almost certainly limited the diffusion range of soluble factors. In ref. [150], however, stromal and epithelial cells were cultured together on plastic (in the same culture well), enabling both physical cell-cell contacts and reduced dependence on the stability of signaling mediators. Finally, RMFs had low prevalence (<10% of total cell content) in each 3D culture studied here. This result was surprising, because, at least in two-dimensional cultures, fibroblasts and MCF10 series cells exhibit similar population doubling times. Therefore, the most dramatic stroma-induced gene expression changes in our model likely occur during the first few days of culture when the proportions of each cell type are roughly equivalent. Transcriptional patterns at later time points, such as those analyzed here, reflect long-term, steady-state responses to co-culture and/or morphologic changes induced therein.

The aim of this study was to explore how p53-dependent stromal-epithelial communication patterns in breast tissue models evolve during progression from pre-malignant to invasive disease. Some of the identified genes have been previously studied in invasive breast cancer, whereas others have only been reported in other tumor types. While certain stroma-modified genes may be targets for BBC prevention, the factors identified herein must be studied mechanistically in greater detail to evaluate their translational relevance. Nevertheless, our results indicate that 3D culture models of pre-invasive breast can recapitulate previously described aspects of invasive breast cancer biology, consistent with reports that *in situ* and invasive breast cancers share certain genomic characteristics

[143-148]. Simultaneously, these models can also generate new insight into how stroma modifies epithelial behavior and signaling patterns during early stages of disease.

2.6. Figures

Figure 2.1. Development of a methodology to study p53-dependent stromal-epithelial interactions in 3D cultures

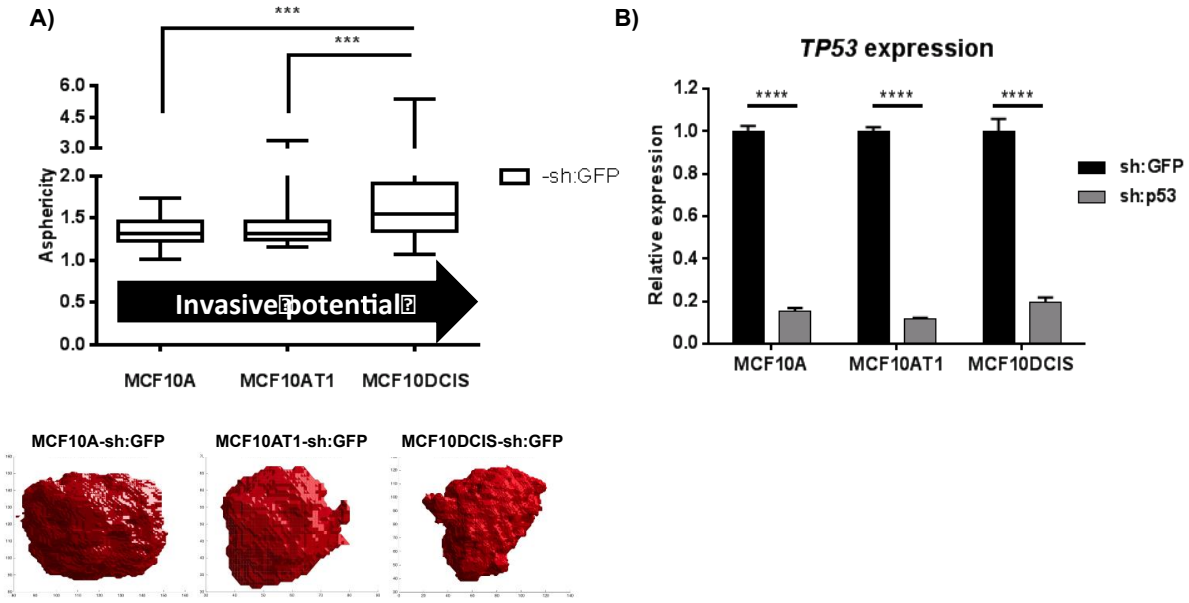

A) Top: Optical coherence tomography (OCT)-based analyses of organoid asphericity. ***p< 0.001. Bottom: Representative organoid renderings showing increased asphericity with progression. **B)** qRT-PCR analysis of *TP53* expression in p53-deficient (-sh:p53) and control (-sh:GFP) MCF10 series cell lines. ****p< 0.0001 -sh:GFP vs. -sh:p53.

Figure 2.2. p53 deficiency increases the asphericity of benign MCF10A organoids

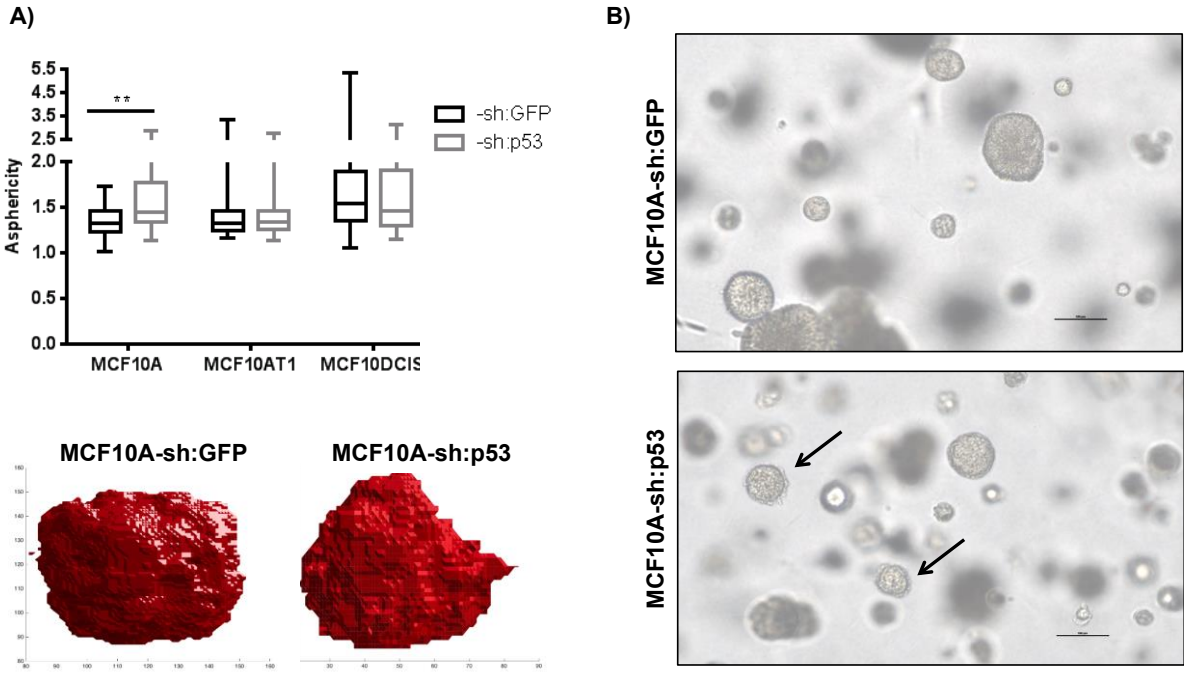

A) Top: OCT-based asphericity measurements of MCF10 series organoids in monoculture. -sh:p53 organoids were compared to their respective -sh:GFP controls. **p<0.01. n = 3 independent experiments. Error bars indicate mean ± SEM. Bottom: Representative MCF10A organoid renderings. **B)** Photomicrographs of MCF10A-sh:GFP and MCF10A-sh:p53 organoids. Note how some MCF10A organoids have small projections invading the 3D matrix (arrows).

Figure 2.3. Contextual transcriptional responses of MCF10 series organoids to p53 deficiency

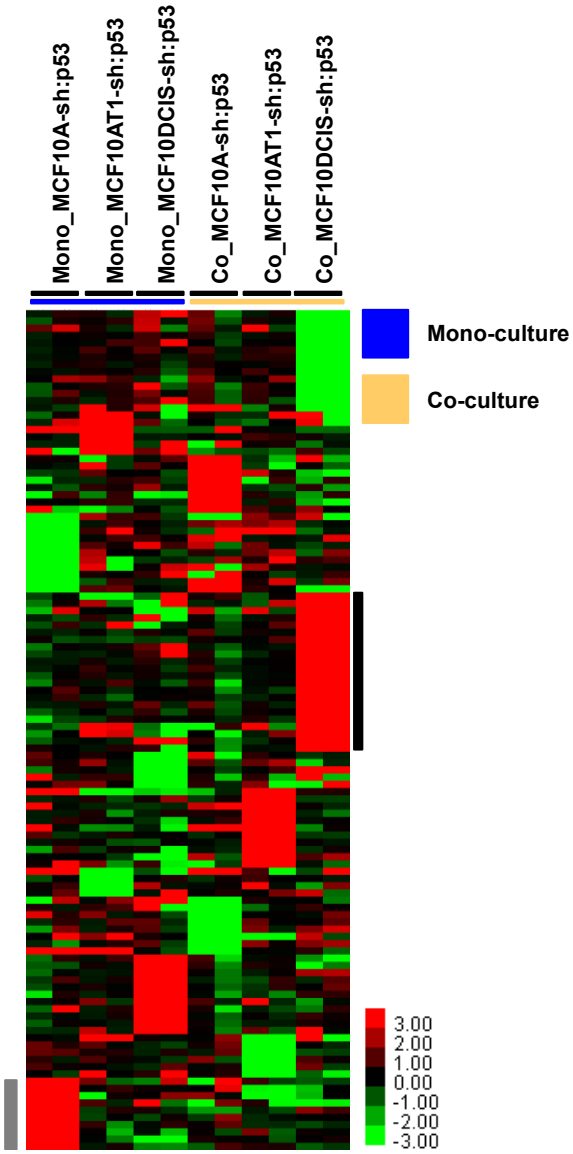

This heat map demonstrates that transcriptional responses to p53 deficiency vary among the MCF10 cell lines, both in mono-culture and co-culture. For mono-cultures (blue bar), the expression of each gene in replicate -sh:p53 samples was normalized to the average expression of that gene across the corresponding -sh:GFP control samples, and data were analyzed by multi-class SAM. Co-culture data (gold bar) was analyzed in a similar manner, and both lists of significant genes (116 genes in total) are included in this heat map. Gene

clusters marked by bars are described in detail in the text. The grey bar indicates genes that were up-regulated in MCF10A-sh:p53 mono-cultures relative to the remaining culture conditions. The black bar indicates genes for which expression was generally highest in MCF10DCIS-sh:p53 co-cultures relative to the remaining culture conditions. Fold change (log[2R/G]) is relative to median expression.

Figure 2.4. p53 deficiency accelerates morphogenetic responses to co-culture

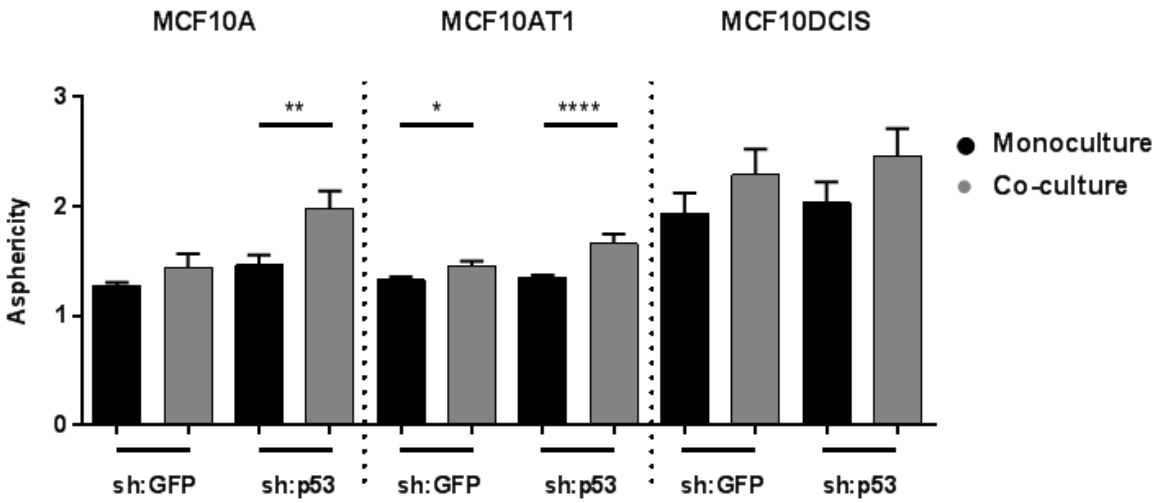

OCT-based asphericity measurements of MCF10 series organoids. For each cell line, co-cultures were compared to their mono-culture controls. *p<0.05; **p<0.01; ****p<0.0001. n = 2 independent experiments. Error bars indicate mean ± SEM.

Figure 2.5. p53-dependent stromal-epithelial interactions are cell line-specific

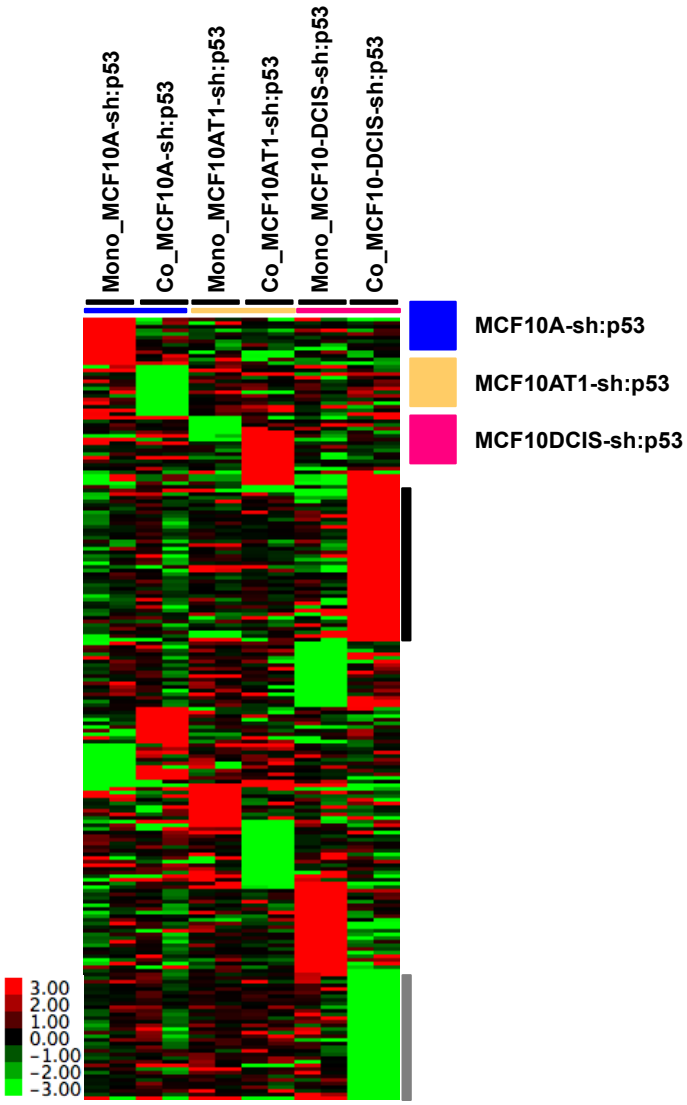

This gene expression heat map depicts the unique p53-dependent responses of each cell line to co-culture. For each cell line, each gene in replicate -sh:p53 mono-culture samples was normalized to the average expression of that gene across the corresponding mono-culture controls, and each gene in replicate -sh:p53 co-culture samples was normalized to the average expression of that gene across the corresponding co-culture controls. A 2-class SAM on each resulting normalized dataset (normalized knock-down mono-culture vs. normalized knock-down co-culture) identified genes that were significantly altered in p53-

deficient cells in response to co-culture. All 3 lists were visualized with a single heat map. Each cell line is indicated with a different color: blue, gold, and magenta bars depict MCF10A-sh:p53, MCF10AT1-sh:p53, and MCF10DCIS-sh:p53 cultures, respectively. Gene clusters marked by black and grey bars are discussed in the text; these clusters contain genes that were up- and down-regulated, respectively, in MCF10DCIS-sh:p53 cultures in response to stroma. Fold change (log[2R/G]) is relative to median expression.

2.7. Tables

Table 2.1. 3D culture seeding densities (cells/mL)

Isogenic pair	Culture medium	Mono-culture	Co-culture	
			Breast cells	RMFs
MCF10A	DMEM/F12	30,000/mL	15,000/mL	15,000/mL
MCF10AT1	DMEM/F12	30,000/mL	15,000/mL	15,000/mL
MCF10DCIS	DMEM/F12	30,000/mL	15,000/mL	15,000/mL
RMFs only	DMEM/F12	30,000/mL as controls for microarray analysis		

Table 2.2. Phosphoprotein-associated genes induced by co-culture in MCF10DCIS-sh:p53 organoids

ENTREZ Gene ID	Gene name symbol)
25966	C2 calcium dependent domain containing 2(C2CD2)
56474	CTP synthase 2(CTPS2)
84444	DOT1 like histone lysine methyltransferase(DOT1L)
11080	DnaJ heat shock protein family (Hsp40) member B4(DNAJB4)
2733	GLE1, RNA export mediator(GLE1)
9778	KIAA0232(KIAA0232)
56950	SET and MYND domain containing 2(SMYD2)
23480	Sec61 translocon gamma subunit(SEC61G)
10629	TATA-box binding protein associated factor 6 like(TAF6L)
4904	Y-box binding protein 1(YBX1)
8091	high mobility group AT-hook 2(HMGA2)
10525	hypoxia up-regulated 1(HYOU1)
3710	inositol 1,4,5-trisphosphate receptor type 3(ITPR3)
64768	inositol-pentakisphosphate 2-kinase(IPPK)
55154	misato 1, mitochondrial distribution and morphology regulator(MSTO1)
8079	myeloid leukemia factor 2(MLF2)
399687	myosin XVIIIA(MYO18A)
79834	pseudopodium enriched atypical kinase 1(PEAK1)
80346	receptor accessory protein 4(REEP4)
57393	transmembrane protein 27(TMEM27)
54877	zinc finger CCHC-type containing 2(ZCCHC2)

CHAPTER 3

MYELOID-SPECIFIC *GLUT1* KNOCKOUT ATTENUATES CLAUDIN-LOW BREAST CANCER PROGRESSION

3.1. Overview

Claudin-low breast cancer (CLBC) is an invasive triple-negative subtype characterized by the presence of a growth-permissive, inflammatory microenvironment, to which myeloid-lineage macrophages are a major contributor. Macrophage *Glut1* (*Slc2a1*)-mediated glucose metabolism is a critical regulator of the inflammatory responsiveness of this cell type; thus, the goal of this study was to evaluate the effect of myeloid lineage *Glut1* loss on CLBC progression. Myeloid-specific *Glut1* knockout ($Glut1^{M-/-}$) mice and littermate controls ($Glut1^{MFl/Fl}$) were orthotopically injected with syngeneic M-Wnt cells, a model of CLBC that recapitulates genomic and molecular features of human disease. We show herein that mammary tissue macrophages (MTMs) of $Glut1^{M-/-}$ compared to $Glut1^{MFl/Fl}$ animals were skewed toward an anti-inflammatory phenotype, and that M-Wnt tumor progression was impeded in $Glut1^{M-/-}$ animals. Collectively, our results indicate that myeloid *Glut1* regulates the inflammatory microenvironment of both normal mammary and breast cancer, with consequences for CLBC progression.

3.2. Introduction

Claudin-low breast cancers (CLBCs) are invasive triple-negative tumors characterized in part by steady-state up-regulation of immune response genes and the presence of histologically conspicuous leukocytic infiltrates [12, 49, 51]. In particular, myeloid-lineage tumor-associated macrophages (TAMs) are highly prevalent in triple-negative breast cancers (TNBCs), and possess a diverse array of recognized roles in promoting inflammation in the tumor microenvironment [98, 100, 101, 103, 104, 178, 179]. Given the growth-permissive, mutagenic nature of chronic inflammation [100, 180], processes or interactions that reduce macrophage inflammatory responsiveness may represent promising targets for novel CLBC therapies.

Energy metabolism is an important component of macrophage inflammatory responsiveness. Pro-inflammatory macrophages preferentially metabolize glucose as an energy substrate [181] in a mechanism reliant upon the glucose transporter, Glut1 (encoded by *Slc2a1*) [182, 183 [submitted manuscript]]. Indeed, *Glut1* overexpression was sufficient to confer a pro-inflammatory phenotype in *ex vivo* bone marrow-derived macrophages (BMDMs) even in the absence of exogenous pro-inflammatory stimuli, suggesting that macrophage metabolic and inflammatory states are tightly linked [182]. Similarly, BMDMs from myeloid-specific *Glut1* knockout mice demonstrated reduced expression of pro-inflammatory and oxidative stress markers, as well as an enhanced capacity to buffer against oxidative stressors [183]. Taken together, these results suggest that modulation of macrophage metabolism is a powerful means by which to alter the inflammatory responsiveness of this cell type, with potential to prevent or delay inflammation-associated mechanisms linked to breast cancer.

In this paper, we explored the consequences of myeloid *Glut1* deficiency on CLBC progression, with a particular emphasis on macrophage-associated features of the tumor

microenvironment. Myeloid-specific *Glut1* knockout mice (*LysM-Cre*; *Slc2a1*$^{Fl/Fl}$ ["*Glut1*$^{M-/-}$"]) and floxed littermate controls ("*Glut1*$^{MFl/Fl}$") [183] were orthotopically injected with M-Wnt cells, a model of CLBC that recapitulates key genomic and histologic features of human disease [184]. Our results underscore a need to comprehensively evaluate the role of the tumor immune microenvironment in CLBC progression, and to further define potentially unique macrophage phenotypes in normal mammary and breast cancer.

3.3. Materials and methods

3.3.1. Animal model

All animal studies were approved by the Institutional Animal Care and Use Committee of the University of North Carolina at Chapel Hill and were performed in accordance with the recommendations of the Panel on Euthanasia of the American Veterinary Medical Association. Animal facilities at UNC are accredited by the Association for Assessment and Accreditation of Laboratory Animal Care (AAALAC), and veterinary care meets National Institutes of Health standards set forth in the Guide for the Care and Use of Laboratory Animals (DHHS Publication No. (NIH) 85-23 Revised 1985). UNC also accepts as mandatory the Public Health Service Policy on Humane Care and Use of Laboratory Animals by Awardee Institutions, as well as NIH Principles for the Utilization and Care of Vertebrate Animals Used in Testing, Research, and Training. Mice were housed in a climate-controlled facility with a 12-hour light-dark cycle, and were given *ad libitum* access to water and diet. *Glut1*$^{M-/-}$ and *Glut1*$^{MFl/Fl}$ on the C57BL/6J background have been described previously [183]. *Glut1*$^{Fl/Fl}$ mice used for breeding were a kind gift from Dr. E. Dale Abel. At three weeks of age, female mice were weaned onto a purified diet delivering 10% kcal from fat (#D12450J). Animals were weighed weekly from 3 weeks of age until euthanasia (see

below) to monitor the impact of experimental procedures on overall health. Expected trends in mouse growth rates were observed, and body weights did not significantly differ by genotype at any time point (**data not shown**).

3.3.2. Flow cytometric analysis of mammary tissue macrophages (MTMs)

Female mice were euthanized via CO_2 asphyxiation and cervical dislocation at 18 weeks of age (n = 3 per genotype group). The left and right abdominal (4^{th} and 7^{th}) MFPs were removed and the intramammary lymph nodes excised. Fat pads were transferred to ice cold high-glucose Dulbecco's Modified Eagle Medium (DMEM, Corning, Corning, NY) containing 20 mM HEPES buffer (Cellgro, Manassas, VA), and were minced with surgical scissors. Both MFPs from each mouse were then digested in 2 mg/mL Type I collagenase (Worthington, Lakewood, NJ) on a rotating incubator for 45-60 min. A single-cell suspension was generated via mechanical dissociation with a Stomacher® 80 Biomaster small tissue lab paddle blender (Seward, Worthing, West Sussex, United Kingdom). Suspensions were diluted with an equal volume of HEPES-buffered DMEM and filtered through a 100-µm cell strainer, followed by centrifugation at 200 *x* g for 10 min at 4°C to generate an immune cell-enriched stromal-vascular fraction (SVF). The resulting SVF pellet was resuspended in HEPES-buffered DMEM and digested with DNase I (Sigma, St. Louis, MO). Red blood cells incubated in ACK lysis buffer (Gibco, Gaithersburg, MD) for 3-5 min at RT. The resulting SVF cells from each mouse were transferred to separate low-adhesion microcentrifuge tubes, blocked with Fc Block (CD16/32) (Biolegend, San Diego, CA), and stained with pre-titrated antibodies (**Table 3.1** for antibody information and dilutions). MTMs were defined as $CD45^+CD11b^+CD64^+$, as CD64 has been reported as a reliable marker to distinguish adipose tissue macrophages from $CD64^-$ myeloid lineage dendritic cells [185, 186]. Viability staining was conducted using Zombie Green™ fixable viability dye (Biolegend) in DPBS as directed. Extracellular antigen staining was conducted using antibodies diluted in DPBS

containing 1% FBS and 5 mM EDTA. Cells were then washed and fixed/permeabilized using Cytofix/Cytoperm™ Fixation/Permeabilization solution (BD Biosciences, San Jose, CA), and incubated with antibodies to intracellular antigens (**Table 3.1**) diluted in BD Perm/Wash™ Buffer overnight at 4°C with gentle agitation. SVF cells were then washed twice with 1X Perm/Wash™ solution, re-suspended in DPBS, and filtered through a 30-µm filter. SVF cells were analyzed on a BD™ LSR II flow cytometer. Compensation was set using single-stained cellular controls and gating was determined based on fluorescence-minus-one (FMO) controls. Data were analyzed with FlowJo (FlowJo, LLC, Ashland, OR).

3.3.3. Orthotopic tumor model and tissue collection

At 13 weeks of age, female mice (*n* = 15-20 per group) received an ipsilateral orthotopic injection of $5x10^4$ viable M-Wnt tumor cells (derived from syngeneic C57BL/6J mice) into the 4^{th} mammary gland as previously described [184] (**Figure 3.1**). Mice were palpated three times weekly to monitor tumor growth. Tumors were measured with electronic calipers and ellipsoid tumor volume was calculated as in ref. [187]. Mice were euthanized via CO_2 asphyxiation and cervical dislocation at tumor maximum size (1 cm. in the largest dimension). Tumors and contralateral (un-injected) 9^{th} mammary glands were collected at sacrifice, and samples were divided in half for both snap freezing and formalin fixation. Contralateral mammary glands from 18-week-old tumor-bearing mice (euthanized 5.0 weeks after M-Wnt cell injection) were used in further molecular analyses to facilitate direct comparisons with flow cytometric profiling of MTMs (see above). Molecular tumor analyses were conducted on size-matched specimens measuring 1.0 $\pm$ 0.25 cm in the largest dimension *ex vivo* to account for minor variations between *in situ* and *ex vivo* maximum size.

3.3.4. Quantitative RT-PCR (qRT-PCR)

Snap-frozen tumor specimens and un-injected contralateral mammary glands from tumor-bearing mice were pulverized under liquid nitrogen. Total RNA was extracted (RNeasy Mini Plus kit, QIAGEN, Valencia, CA) and reverse-transcribed (500 ng per sample; iScript Reverse Transcription Supermix, Bio-Rad) according to the manufacturers' instructions. Gene expression was quantitated using TaqMan Gene Expression Assays (Applied Biosystems, Foster City, CA), except for *Il10, Ccl2*, and *Nos2* which were measured using Roche Universal Probe Library Assays (Roche Diagnostics US, Indianapolis, IN) with the following oligonucleotide pairs: *Il10*: F: 5'-CAGAGCCACATGCTCCTAGA-3'; R: 5'-GTCCAGCTGGTCCTTTGTTT-3'; *Ccl2*: F: 5'-AGCACCAGCCAACTCTCACT-3'; R: 5'-GTGGGGCGTTAACTGCAT-3'; and *Nos2*: F: 5'-TGACACACAGCGCTACAACA-3'; R: 5'-GCCAGTGTGTGGGTCTCC-3'. All samples were run on an ABI 7900HT Fast real-time PCR machine (Invitrogen, Carlsbad, CA) using the SsoAdvanced Universal Probes Supermix (Bio-Rad). Genes of interest were normalized to 18S rRNA using the ΔΔCt method.

3.3.5. Digital histology

Staining: Formalin-fixed, paraffin-embedded (FFPE) tumor and contralateral mammary tissue specimens were sectioned at 5 μm and mounted on positively charged glass slides. Immunohistochemical (IHC) staining was conducted using pre-titrated antibodies (**Table 3.2**) according to previously described procedures [188], and no-primary controls were employed for each stain. Hematoxylin and eosin staining was also performed on FFPE tumor sections according to standard protocols.

Tissue annotation: Stained slides were scanned into digital images using the Aperio ScanScope CS system (Aperio Technologies, Vista, CA). Aberrations in the tissue, as well as areas of non-mammary or non-tumor tissue (e.g., skin, lymph nodes, muscle) were

excluded from digital analyses. All annotations were made by an investigator blinded to mouse genotype.

Quantitative histology: Diaminobenzidine (DAB) staining in IHC-stained slides was analyzed quantitatively using Aperio ImageScope algorithms ("IHC Nuclear" algorithm for Ki67 staining; "Color Deconvolution" algorithm for remaining IHC markers except for cleaved caspase-3) [188]. Cleaved caspase-3 expression was quantitated using the "positive pixel count" algorithm; only cells with "strong positive" staining, which exhibited a rounded-up apoptotic morphology, were analyzed. Positive DAB staining in negative control (no primary antibody) slides was subtracted from the corresponding stained samples as non-specific background. For all analyses, tissue sections were examined in their entirety. All images shown herein are representative of a given tissue section and genotype group.

3.3.6. Luminex assays

Tumor cytokines and chemokines were measured using the Bio-Plex Multiplex Immunoassay System with Luminex xMAP Technology (Bio-Rad, Hercules, CA) according to the manufacturer's instructions. Tumors were pulverized under liquid nitrogen and 100 mg of each sample was diluted in 500 µL of RIPA buffer containing 1x Halt Protease Inhibitor Cocktail (Thermo Scientific, Waltham, MA). Samples were homogenized and centrifuged at 16000 x *g* for 20 minutes at 4°C, and a bicinchoninic acid (BCA) assay (Pierce, Waltham, MA) was performed on sample supernatants. Supernatants were then diluted to 450 µg/mL, and 50 µL of each sample was used in the Bio-Plex assays. Samples were analyzed in duplicate.

3.3.7. Statistics

Statistical analyses were performed using GraphPad Prism version 7.0 (GraphPad Inc., La Jolla, CA). For flow cytometric analyses of marker distribution between *Glut1*$^{M-/-}$ and

Glut1$^{MFl/Fl}$ mice, statistical significance was determined with multiple t-tests (1 per row [cell subpopulation/quadrant]) correcting for multiple comparisons using the Holm-Sidak method with alpha = 0.05. As each cell subpopulation originated from the same sample, computations assumed that all rows were sampled from a population with the same standard deviation. All other data were analyzed using the two-tailed unpaired student's t-test or log-rank test as appropriate. Unless otherwise specified, error bars represent the mean ± standard error of the mean (SEM), and statistical outliers were identified using the robust non-linear regression with outlier removal (ROUT) method with Q = 1%. For all analyses, p-values less than 0.05 were considered significant.

3.4. Results

3.4.1. Myeloid Glut1 loss reduced MTM inducible nitric oxide synthase (iNOS) expression

As a first step to elucidating the effect of myeloid *Glut1* loss on CLBC progression, we used flow cytometry to characterize the immune microenvironment of the normal mammary gland, with a particular emphasis on mammary tissue macrophages (MTMs). Macrophages are the most highly represented immune cell type in the mouse and human mammary gland, and are crucial regulators of initiation, invasion, and metastasis in breast cancer [25]. To determine whether myeloid-specific *Glut1* knockout altered mammary immune cell proportions, we quantitated total leukocyte ($CD45^+$), myeloid cell ($CD45^+CD11b^+$), and MTM ($CD45^+CD11b^+CD64^+$) content in freshly isolated MFP specimens of 18-week-old mice (see gating strategy in **Figure 3.2**). The proportions of each cell type did not vary by genotype (**data not shown**).

We next sought to characterize specific immunophenotypes of MTMs in *Glut1*$^{M-/-}$ and *Glut1*$^{MFl/Fl}$ mice. Based on recent work in mice and humans suggesting that macrophages in adipose-rich tissues exhibit "mixed" expression of pro- and anti-inflammatory markers [189-195], we quantitated the expression of iNOS and arginase 1 (ARG1), canonical pro- and anti-inflammatory markers, respectively, among macrophages in the mammary fat pad. There were no significant *Glut1*-driven differences in the proportions of classically defined M1 (ARG1^{-}iNOS^{+}) or M2 (ARG1^{+}iNOS^{-}) macrophages (**Figure 3.3A**). Interestingly, however, the proportion of ARG1^{+}iNOS^{+} MTMs was diminished in *Glut1*$^{M-/-}$ relative to *Glut1*$^{MFl/Fl}$ mice (**Figure 3.3A**; p = 0.0086 *Glut1*$^{M-/-}$ vs. *Glut1*$^{MFl/Fl}$ LFD). In sum, the percentage of iNOS^{+} MTMs (irrespective of ARG1 positivity) was reduced in the absence of myeloid *Glut1*.

To determine whether select MTM subpopulation(s) were driving observed differences in ARG1/iNOS distribution, we stratified MTMs based on MHCII expression level (hi vs. lo/-). A significantly increased proportion of MHCII^{hi} MTMs was detected in MFP of *Glut1*$^{M-/-}$ vs. *Glut1*$^{MFl/Fl}$ mice (p = 0.0034) (**Figure 3.3B**), but no significant *Glut1*-mediated differences in ARG1 or iNOS expression in MHCII^{hi} MTMs were observed by analysis of median fluorescence intensities (MFIs) (**data not shown**). In contrast, the proportion of MTMs negative for or expressing low levels of MHCII (MHCII$^{lo/-}$) did not significantly differ between *Glut1*$^{M-/-}$ and *Glut1*$^{MFl/Fl}$ mice (**Figure 3.3B**). Interestingly, however, in this MHCII$^{lo/-}$ population, the proportion of ARG1^{+}iNOS^{+} MTMs was significantly reduced in *Glut1*$^{M-/-}$ compared to *Glut1*$^{MFl/Fl}$ mice (p = 0.0216; **Figure 3.3C**). This finding suggests that the observed reductions in ARG1^{+}iNOS^{+} cells among total MTMs (**Figure 3.3A**) was driven by differential expression of ARG1 and/or iNOS within the MHCII$^{lo/-}$ subpopulation.

To gain insight into the cellular and molecular basis for the observed *Glut1*-driven shifts in ARG1/iNOS expression distribution among MHCII$^{lo/-}$ MTMs, we next analyzed expression of ARG1 and iNOS within this subpopulation. Quantification of ARG1 and iNOS MFIs in MHCII$^{lo/-}$ MTMs revealed reduced iNOS expression, with no significant change in

ARG1 expression (**Figure 3.3D** p = 0.0229 *Glut1*$^{M-/-}$ vs. *Glut1*$^{MFl/Fl}$). In sum, compared to those in *Glut1*$^{MFl/Fl}$ MFP, MTMs of *Glut1*$^{M-/-}$ mice exhibited diminished pro-inflammatory iNOS expression, with the MHCII$^{lo/-}$ subpopulation predominately driving this reduction.

3.4.2. Myeloid-specific Glut1 knockout did not alter markers of mammary gland inflammation

As MTMs in *Glut1*$^{M-/-}$ mice exhibited diminished pro-inflammatory iNOS expression, we reasoned that *Glut1*$^{M-/-}$ MFP would also display attenuated inflammatory mediator expression. To facilitate temporal comparisons with flow cytometry data, we quantitated the expression of cytokines and chemokines with recognized roles in breast cancer onset and progression [25] in MFP tissue from 18-week-old mice. None of the factors in our panel (*Il6*, *Il10*, *Il12*, *Tnf*, *Ccl2*, *Il1b)* were differentially regulated between *Glut1*$^{M-/-}$ and *Glut1*$^{MFl/Fl}$ MFP (**data not shown**), perhaps reflecting the status of macrophages as minority components of the normal mammary gland.

3.4.3. Myeloid-specific Glut1 knockout delayed CLBC growth

Having profiled select inflammatory characteristics of the mammary gland with particular relevance to breast cancer, we next examined the impact of myeloid-specific *Glut1* deficiency on CLBC progression. *Glut1*$^{M-/-}$ mice and *Glut1*$^{MFl/Fl}$ controls were orthotopically injected with M-Wnt CLBC cells at 13 weeks of age. Similar to previous reports [184], M-Wnt tumors in our study were poorly differentiated, contained abundant intratumoral adipocytes (**Figure 3.4A**), and exhibited microvascular proliferation (CD31 positivity) (**Figure 3.4B**). Quantitation of CD31 staining indicated that tumor angiogenesis did not dramatically vary by genotype (**Figure 3.4B**), and in both groups, blood vessels were most prevalent proximal to the tumor margins.

Tumor progression was tracked to a pre-determined maximum size (1 cm. in the largest dimension). Tumors in *Glut1*$^{M-/-}$ mice were substantially smaller than those in *Glut1*$^{MFl/Fl}$ controls after 5.5 weeks of growth (p = 0.0593; **Figure 3.5A**). We also noticed that *Glut1*$^{M-/-}$ tumors appeared to grow for a longer period of time before reaching the 1-cm cutoff, which was confirmed by Kaplan-Meier analysis (**Figure 3.5B**; p = 0.0137 *Glut1*$^{M-/-}$ vs. *Glut1*$^{MFl/Fl}$). This differential tumor progression could not be attributed to significant differences in time to palpation of detectable lesions (**data not shown**), or tumor cell proliferation (Ki67 staining; **Figure 3.4C**) or apoptosis (cleaved caspase-3 staining; **Figure 3.4D**).

3.4.4. Glut1$^{M-/-}$ *immune microenvironments may suppress tumor growth*

Heterotypic cancer-stroma interactions, together with tissue remodeling induced by tumor immune infiltrates, foster a growth-permissive microenvironment characterized in part by chronic, low-grade inflammation [100, 188, 196]. Given the known role of *Glut1* in the regulation of macrophage inflammatory character [182, 183], as well as the high prevalence of TAMs in TNBCs [103, 178], we reasoned that delayed tumor growth in *Glut1*$^{M-/-}$ mice would correlate with reduced expression of inflammatory cytokines and chemokines in the tumor microenvironment. Consistent with our hypothesis, we observed striking reductions in the protein concentrations of MCP-1 (CCL2), IL-12β, TNFα, and IL-10 in *Glut1*$^{M-/-}$ relative to *Glut1*$^{MFl/Fl}$ tumors (**Figures 3.6A-D**; p = 0.0064, p = 0.0171, p = 0.0050, and p = 0.0003, respectively), even in the absence of significant genotype-driven differences in TAM content (**Figure 3.6E**). This result suggests that the inflammatory potential of TAMs, like MTMs, may be reduced in *Glut1*$^{M-/-}$ mice. As the inflammatory properties of macrophages are intimately linked to cell behavior [105], we began to explore whether loss of myeloid *Glut1* elicited alterations in macrophage function. Antigen presentation to T cells is an important general function of macrophages, particularly in the context of T cell-mediated anti-tumor immunity.

Hence, we quantitated the expression of select antigen presenting cell (APC) markers [197] in CLBC tumors. While *Cd74* did not significantly differ by genotype, we observed a significant up-regulation of *Cd80* ($p = 0.0026$) and *Cd86* ($p = 0.0073$) in *Glut1*$^{M-/-}$ compared to *Glut1*$^{MFl/Fl}$ tumors (**Figures 3.6F-G)**. Taken together, these data indicate that *Glut1*$^{M-/-}$ CLBCs are characterized by unique inflammatory microenvironments with potential to influence the course of disease.

3.5. Discussion

Specific roles of the tumor microenvironment in promoting breast cancer progression are increasingly understood. However, as the most recently recognized breast cancer subtype [48], tumor-microenvironment interactions in CLBC are poorly defined. Steady-state up-regulation of inflammatory and immune response genes is one well-documented molecular feature of CLBCs [12, 49, 51, 103]. While these gene expression patterns may represent cancer cell-intrinsic features, they also reflect the presence of a wide array of infiltrating leukocytes, particularly pro-inflammatory macrophages. Due to associations among CLBC, inflammation, and macrophage energy metabolism [26, 100, 101, 104, 179, 182, 183, 198-200], we used a pre-clinical model to determine whether suppression of myeloid cell glucose metabolism modulated CLBC progression and immunologic features of the tumor microenvironment linked to breast cancer.

Previous cell-based assays in our laboratory have shown that *Glut1* expression and glucose utilization are intimately tied to macrophage pro-inflammatory character [182]. Herein, we built upon our previous data by describing relationships between myeloid *Glut1* and the regulation of inflammation *in vivo*. This whole-animal context is important because it demonstrates that myeloid *Glut1* regulates tissue-level inflammation with functional

implications for disease. Although our study did not identify specific mechanisms by which myeloid *Glut1* represses CLBC progression, our data offer several clues. First, chronic inflammation *per se* is growth-permissive, but we did not observe genotype-driven differences in tumor Ki67 expression. Second, both *Glut1*$^{M-/-}$ BMDMs [183] and MTMs express lower levels of oxidative stress markers (e.g., iNOS/*Nos2*), so the reactive oxygen species burden associated with chronic inflammation may be relatively lower in *Glut1*$^{M-/-}$ tissues. Third, upregulation of APC markers (*Cd80* and *Cd86*) in *Glut1*$^{M-/-}$ relative to *Glut1*$^{MFl/Fl}$ cancers may indicate a direct role for myeloid *Glut1* in the control of tumor immune tolerance [201, 202]. Future studies should more closely examine the potential role of myeloid *Glut1* in the regulation of tumor immunogenicity.

Our data suggest that *Glut1*$^{M-/-}$ macrophages are skewed toward an anti-inflammatory phenotype, but are associated with attenuated tumor progression. This pattern contrasts sharply with much of the available literature pertaining to TAM biology. Although little research has characterized the metabolic properties of TAMs, many studies have indicated that TAMs in advanced tumors possess anti-inflammatory character, and are therefore likely to exhibit an oxidative, rather than a glycolytic, metabolic signature [203]. TAMs have also been widely demonstrated to facilitate tumor progression, mediate development of therapeutic resistance, and promote relapse [203]. However, one recent study [204] found that macrophages exposed to secretions from pancreatic ductal adenocarcinoma cells (PDAC-TAMs) exhibited a pronounced glycolytic signature. PDAC-TAMs also promoted tumor behaviors associated with invasion and metastasis, but these phenotypes were blocked upon inhibition of TAM glycolysis. This study [204] provided the first direct evidence that alterations in macrophage metabolism could promote cancer cell metastasis, and that reduced macrophage glycolysis – a previously reported feature of *Glut1*$^{M-/-}$ BMDMs [183] – could suppress metastatic spread. Although the CLBC cells used in the present study only invade locally, macrophage glycolysis-dependent tumor metastasis

may be applicable to this tumor type. Future work should establish whether CLBC-associated TAMs also exhibit a glycolytic signature, and if inhibition of glycolysis in metastatic TNBC can prevent tumor cell dissemination.

An additional intriguing finding of the present study is that myeloid *Glut1* regulated the inflammatory character of normal mammary macrophages. To our knowledge, our study is the first to characterize specific immunophenotypes of MTMs; hence elucidating specific functions of individual MTM populations identified herein is an important area of future research. We were interested to observe a significantly increased proportion of MHCII^{hi} MTMs in *Glut1*$^{M-/-}$ relative to *Glut1*$^{MFl/Fl}$ mice, as MHCII expression in *tumor* immune cells inversely correlates with cancer progression [205-209]. Accordingly, our study could be strengthened by immunophenotypic analyses of TAMs in *Glut1*$^{M-/-}$ vs. *Glut1*$^{MFl/Fl}$ CLBCs.

Although *Glut1* expression in myeloid lineage neutrophils and dendritic cells is also targeted by *LysM-Cre*-mediated excision in our mouse model [210], we primarily focused our studies on macrophages because they are the most prevalent immune cell type in both normal and tumor mammary tissue, and play crucial roles in all phases of breast cancer development [25, 100]. Nevertheless, ongoing experiments in M-Wnt tumor tissue are further exploring how other myeloid cell types may contribute to the *Glut1*-dependent cancer progression phenotype. Ultimately, our study underscores a need to comprehensively evaluate the role of the tumor immune microenvironment in CLBC progression, and to further define potentially unique macrophage phenotypes in normal mammary and breast cancer.

3.6. Figures

Figure 3.1. Study schematic

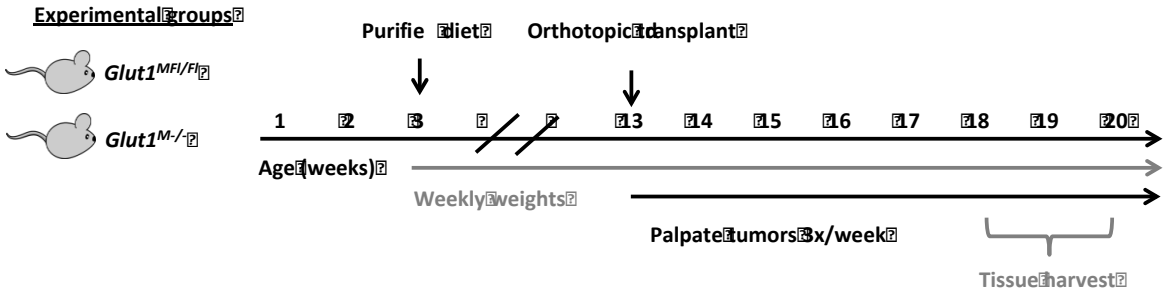

Study design. Mice were fed a purified diet at weaning and were orthotopically injected with M-Wnt CLBC cells at 13 weeks of age. Contralateral mammary and tumor tissues were harvested at tumor maximum size (1 cm in the largest dimension). Body weights were measured weekly.

Figure 3.2. Gating strategy for flow cytometric analysis of mammary tissue macrophages

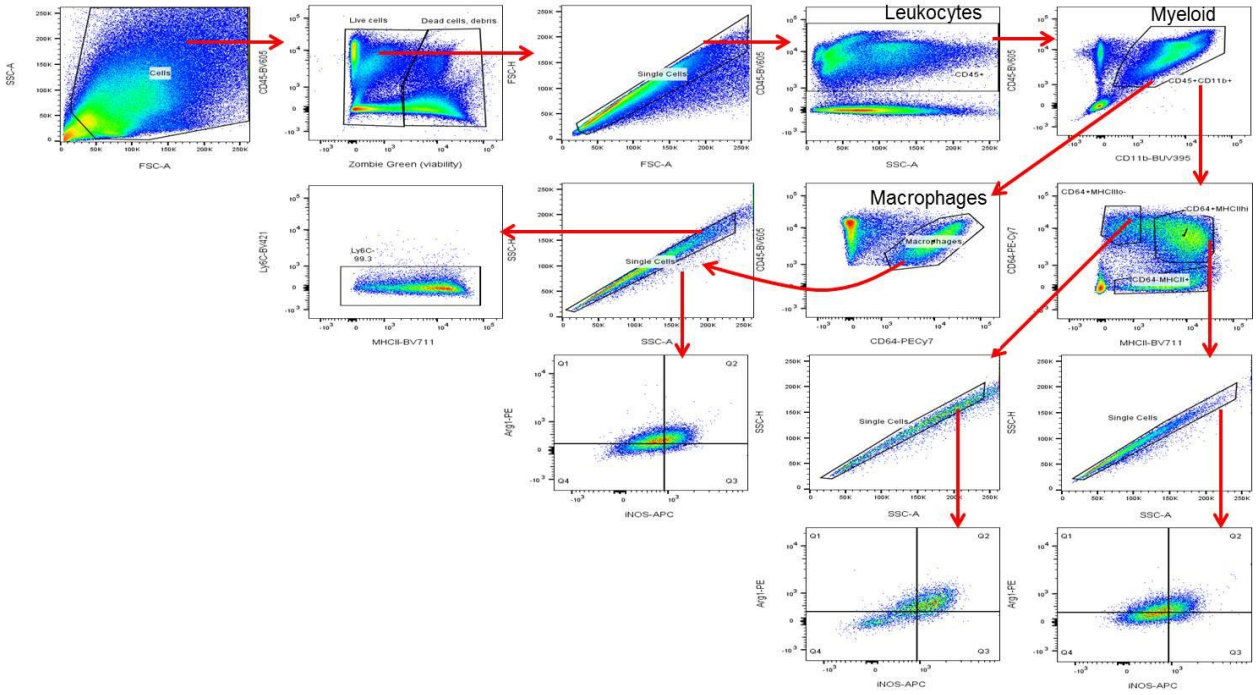

Figure 3.3. Myeloid *Glut1* deletion reduced MTM iNOS expression

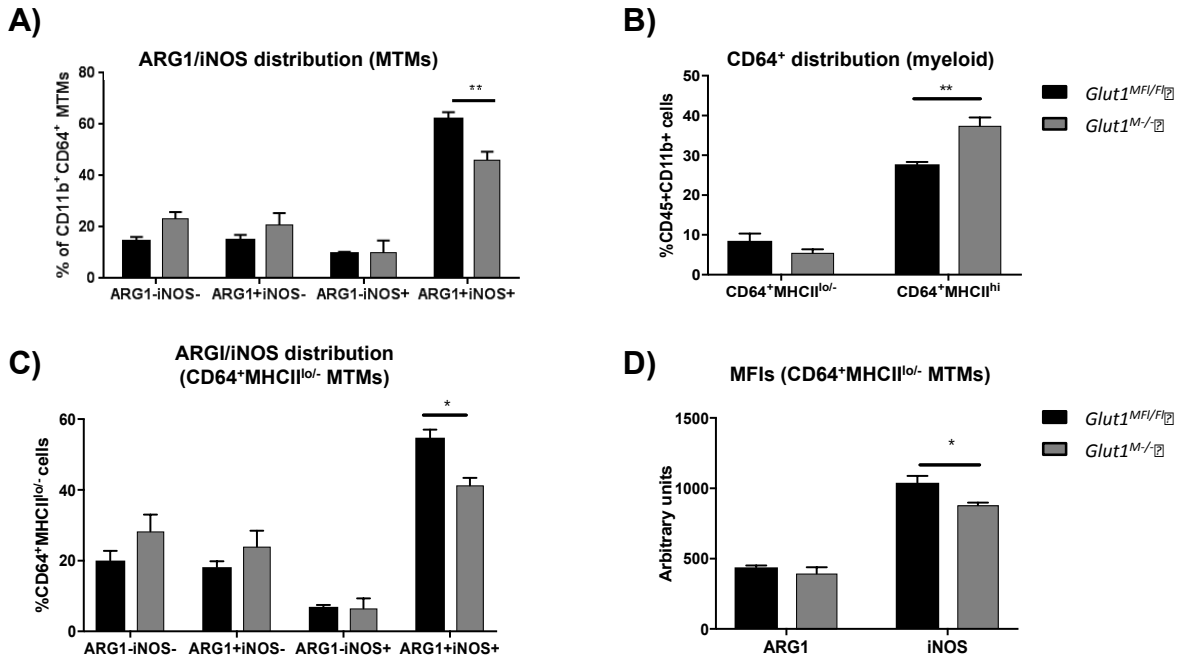

A) Distribution of ARG1 and iNOS expression among total mammary tissue macrophages (MTMs). **B)** Distribution of CD64 and MHCII expression among myeloid cells. **C)** Distribution of ARG1 and iNOS expression among $CD64^{+}MHCII^{lo/-}$ MTMs. **D)** ARG1 and iNOS MFIs among $CD64^{+}MHCII^{lo/-}$ MTMs. For all graphs, *$p \leq 0.05$; **$p \leq 0.01$, ***$p \leq 0.001$. Exact significance levels are reported in the text. Error bars indicate mean $\pm$ SEM.

Figure 3.4. Histologic features of M-Wnt tumors

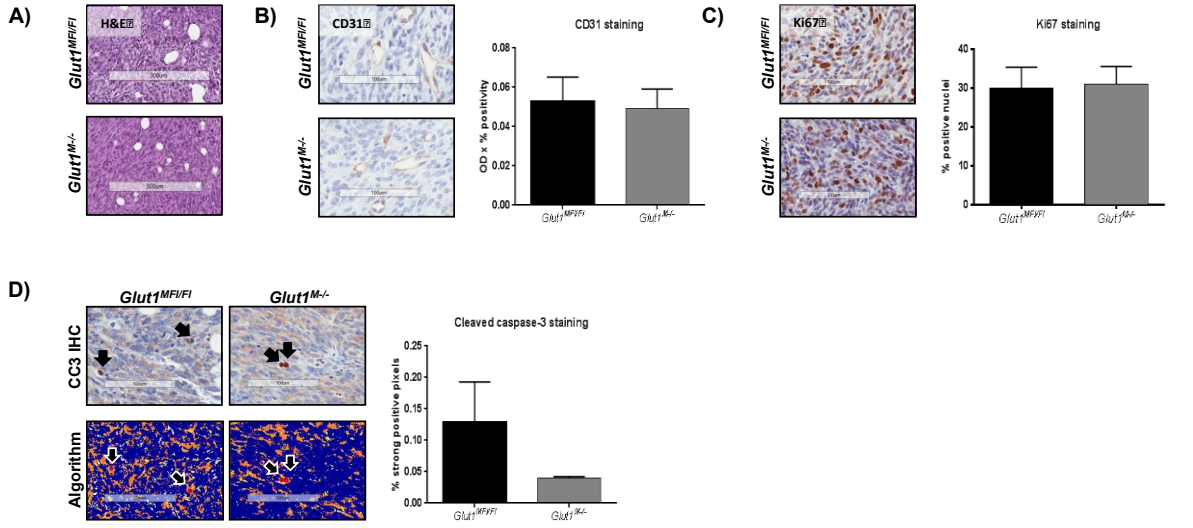

A) Representative tumor H&E staining. Scale bar = 300 μm. **B)** Representative images and digital quantitation of tumor CD31 staining. Scale bar = 100 μm. **C)** Representative images and digital quantitation of Ki67 staining. Scale bar = 100 μm. **D)** Top: Representative images of tumor cleaved caspase-3 (CC3) staining. Arrowheads indicate “strong CC3-positive” apoptotic cells with a rounded-up morphology. Scale bar = 100 μm. Bottom: Positive pixel count algorithm output. Only “strong positive” staining (red), corresponding to apoptotic cells in top panels (arrowheads), was quantitated. Scale bar = 100 μm. Right: Digital quantification of tumor CC3 staining.

Figure 3.5. Myeloid-specific *Glut1* knockout delays tumor growth

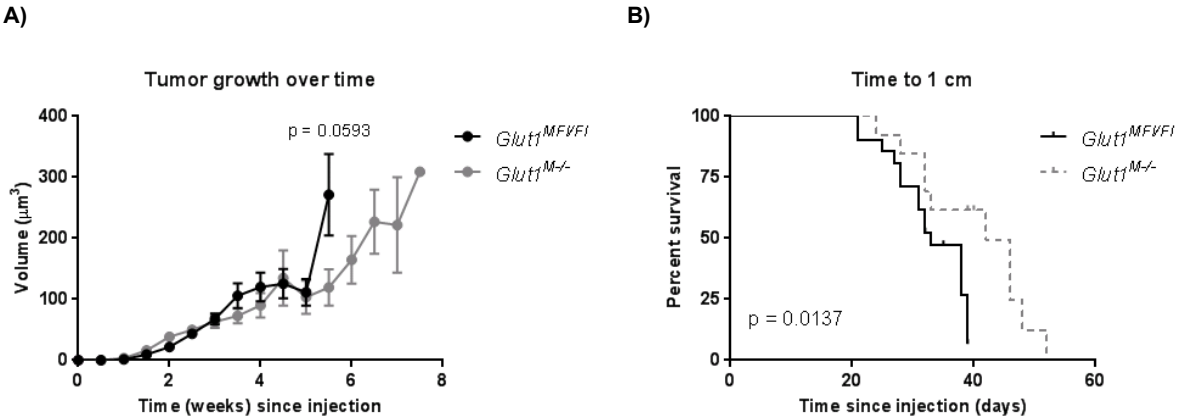

A) Analysis of tumor growth over time. Tumors were palpated three times weekly and tracked to a pre-determined size cutoff (1 cm in the largest dimension). **B)** Kaplan-Meier analysis showing that M-Wnt tumor growth to 1 cm progressed significantly more slowly in *Glut1*$^{M-/-}$ compared to *Glut1*$^{MFl/Fl}$ mice.

Figure 3.6. *Glut1*$^{M-/-}$ immune microenvironments may suppress tumor growth

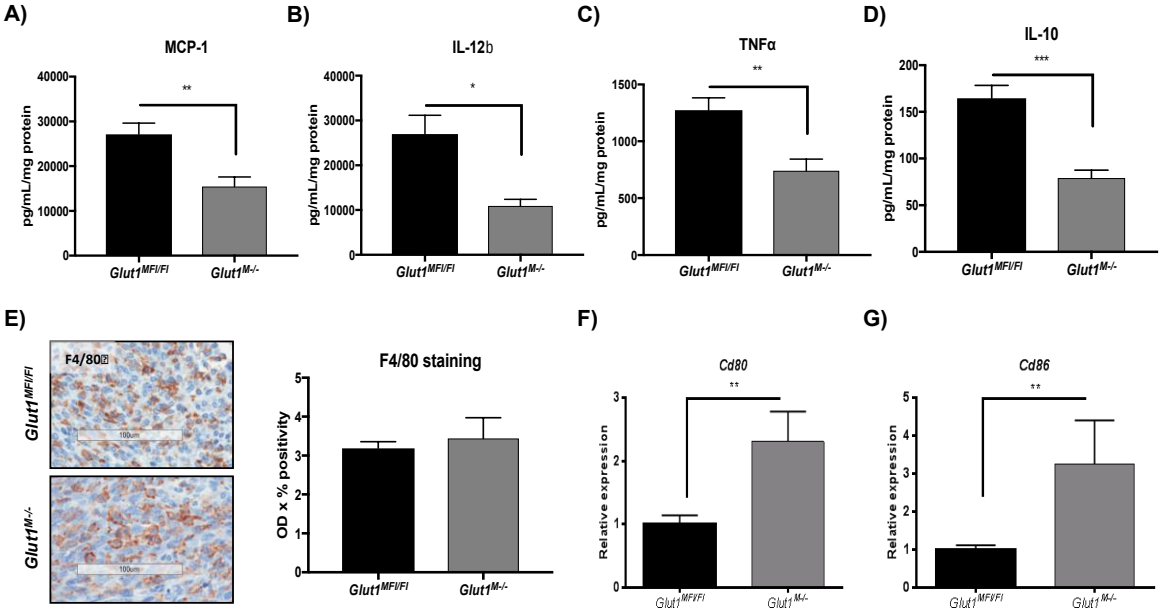

A-D) Protein concentrations of the inflammatory cytokines MCP1 (**p=0.0064), IL-12β (*p=0.0171), TNFα (**p=0.0050), and IL-10 (***p=0.0003) in tumor lysates were quantitated with Luminex assays. **E)** Representative images and digital quantitation of tumor F4/80 staining. Scale bar = 100 μm. **F-G)** qRT-PCR analysis of **F)** *Cd80* and **G)** *Cd80* in tumor lysates.

3.7. Tables

Table 3.1: Antibodies used for flow cytometry studies

Antigen	Fluorophore	Company; cat. #	Dilution	Lot #
Fc block (CD16/32)	N/A	Biolegend; 101320	1:50	B200134
Live/dead dye	Zombie Green	BioLegend; 423111	1:400	N/A
CD45	BV605	BioLegend; 103140	1:200	B211813
CD11b	BUV395	BD Biosciences; 563553	1:00	6028814
Ly6C	BV421	BD Biosciences; 562727	1:100	5357529
MHC II	BV711	eBioscience; 17-5321-81	1:200	6167935
CD64	PE-Cy7	BioLegend; 139313	1:200	B197402
ARG1	PE	R&D Systems; IC5868P	1:40	ADBB0415041
iNOS	APC	Affymetrix (eBioscience); 17-5920-80	1:40	4318613

Table 3.2: Antibodies and analysis parameters for quantitative histology

Antigen	Company; cat. #	Dilution	Lot #	Algorithm: metric
CD31	Abcam; ab28364	1:2500	GR212364-5	Color Deconvolution: OD x % positivity
Ki67	Vector Laboratories; VPRM04	1: 250	ZA0731	IHC Nuclear: % positive nuclei
Cleaved caspase-3	Cell Signaling; 9661	1:1500	43	Positive pixel count: % strong-positive pixels
F4/80	AbD Serotec; MCA-497	1:2000	0413	Color Deconvolution: OD x % positivity

Abbreviations: OD: optical density; Y: tyrosine

CHAPTER 4

DEVELOPMENT OF A DIGITAL ALGORITHM TO QUANTITATE CD31$^+$ VASCULATURE IN CANCER-ADJACENT NORMAL HUMAN BREAST

4.1. Overview

Studies of histologically benign-appearing, cancer-adjacent tissue may yield important insights into factors that influence locoregional disease recurrence after therapy. Triple-negative breast cancers are more likely than other breast cancer subtypes to recur locally and to metastasize within the first three to five years of patient follow-up, but microenvironmental factors underlying differential recurrence rates among breast cancer subtypes are poorly understood. Given the essential nature of tumor angiogenesis in cancer invasion and metastatic progression, we hypothesized that the vascular content of cancer-adjacent breast tissue differs in association with the subtype of the corresponding tumor. To this end, we developed a novel digital algorithm to quantitate CD31$^+$ vasculature in histologically benign tissue from women with breast cancer. We found that the digital algorithm was highly correlated with manual assessment, suggesting that high-throughput, quantitative estimates of vascular content and phenotypes could be provided. This algorithm will ultimately be used to determine how parameters such as vascular density and median vessel size vary with respect to tumor subtype, established breast cancer risk factors, and other tissue histologic features.

4.2. Introduction

Triple-negative breast cancer (TNBC) exhibits higher rates of locoregional recurrence relative to other breast cancer subtypes, particularly within the first three to five years of follow-up [52, 53, 57, 58]. Tumor biological characteristics are a key factor that may contribute to observed differential recurrence rates, but we and others have demonstrated that gene expression profiles of and cell-cell interactions within cancer-adjacent breast also vary according to the subtype of the corresponding tumor [76, 77]. For example, fibroblasts are key contributors to the inflammatory gene expression and cytokine production associated with TNBC-adjacent tissue environments [76]; however, it is unknown whether the content and/or phenotypes of other stromal cell types in benign-appearing, cancer-adjacent tissue also differ in association with breast cancer subtype.

The vasculature is a particularly understudied component of the breast cancer microenvironment. A small number of reports [111-114] have profiled cancer cell-endothelial interactions in the setting of frank breast tumors, but very little work has examined the vascular properties of normal or tumor-adjacent breast. Given that the induction of angiogenesis is a requisite step for progression to metastatic disease, it is plausible that subtype-specific differences in cancer-adjacent vascular properties may play a role in observed variations in local recurrence rates. We hypothesized that cancer-adjacent vascular content and phenotypes differ in association with the intrinsic subtype of the corresponding tumor. To this end, we developed a novel digital algorithm designed to quantitate immunohistochemical (IHC) staining of CD31, a cell-surface marker greatly enriched in endothelial cells, in histologically benign tissue from women with breast cancer. This algorithm will be used to determine how vascular features in cancer-adjacent tissue relate to tumor subtype, established breast cancer risk factors, and other histologic features of cancer-adjacent breast.

4.3. Materials and methods

4.3.1. Study population

A subset of patients from the University of North Carolina Normal Breast Study (UNC NBS), a study previously described [211, 212], was included in this report. Briefly, the UNC NBS is a hospital-based study of normal breast tissue and breast cancer microenvironments conducted in association with UNC Hospitals. Women undergoing breast surgeries (excisional biopsy, lumpectomy, mastectomy, reduction mammoplasty, or other cosmetic procedure) between October 2009 and April 2013 were eligible to participate if they were at least 18 years of age, English-speaking, and consented to donate tissue during their surgery. As described in [211, 212], all participants donated grossly normal-appearing tissue as assessed by pathology assistants at UNC. Tissue was snap-frozen in liquid nitrogen. Patients also provided demographic, lifestyle, and breast cancer risk factor exposure data through a telephone interview, and medical records abstraction was performed to obtain anthropometric and medical history data. Medical records follow-up is continuing, to be conducted annually for 10 years following a patient's surgery. Protocols were approved by the University of North Carolina School of Medicine Institutional Review Board.

The full UNC NBS study population consisted of 474 women, including 399 women with ipsilateral invasive breast cancer and 75 women with a benign breast condition [211]. Hematoxylin and eosin-stained tissue slides were created for each patient and manually reviewed. Specimens from 16 women were excessively folded and unsuitable for further analysis, whereas those from 4 women were found to have histologically abnormal tissue with >50% epithelial cell content. After excluding these 20 patients, the final NBS study population consisted of 454 women, including 387 women with ipsilateral invasive breast cancer and 67 women with a benign condition [211]. In the present analysis, cases with pathologically confirmed invasive, *in situ*, or benign breast disease, as well as those with a

prior history of breast cancer, were selected, excluding women undergoing prophylactic or cosmetic procedures. Since some participants in the NBS had a prior breast surgery, patients undergoing a second breast surgery were also excluded to avoid quantitating vasculature within granulation or fibrotic tissue induced by a previous breast surgery. These exclusions resulted in a total of 410 patients, of which 235 were randomly selected, equating to approximately half (51.8%) of all NBS study participants. We analyzed one sample per woman, using second specimens to assess intra-individual variation for approximately 20% of our population (n = 52 women; 22.1%). Slides were manually reviewed after IHC staining (see below), and 8 samples were excluded due to high levels of non-specific staining. Therefore, the total study population consisted of 228 women (50.2% of NBS participants) and 279 unique tissue samples. The demographic characteristics of our population are presented in **Table 4.1**. The majority of women in our study (91.7%) had invasive or *in situ* breast cancer at the time of their surgery, whereas the remaining patients had either a benign condition (7.5%) or a previous history of treated breast cancer at least one year prior to their consented surgery (0.9%). Average age at surgery was highest among breast cancer patients, and lowest among women presenting with benign conditions. Body mass index (BMI) did not differ substantially among groups.

Given the high percentage of breast cancer patients in our study, the clinicopathologic characteristics of the corresponding tumors are presented in **Table 4.2**. Consistent with expectations, the majority of tumors were ER^+, PR^+, and $HER2^-$. Tumors also tended to be small ($\leq$2.0 cm.) and low stage, with 85.2% of patients presenting with stage 0-2 disease.

4.3.2. Immunohistochemical CD31 staining

As described in [211], snap-frozen tissue was cut over dry ice and 20-μm sections were cut and mounted on positively charged glass slides. Slides were then randomized to

batches of 24, and IHC staining was performed according to standard protocols. Briefly, slides were fixed in zinc formalin for 10 minutes, and heat-induced epitope retrieval was performed using Lab Vision HIER Buffer (Thermo Fisher Scientific, Waltham, MA). Slides were then incubated with 3% hydrogen peroxide to block endogenous peroxidases, blocked with 10% normal goat serum for 1 hour at room temperature, and incubated with pre-titrated mouse anti-CD31 antibodies (0.25 µg/mL; #3528, lot #4; Cell Signaling Technologies, Danvers, MA) overnight at 4°C. Slides were then incubated with biotinylated goat anti-mouse IgG secondary antibodies (#115-065-166, lot #89998; Jackson ImmunoResearch, West Grove, PA) for 1 hour at room temperature, and staining was visualized using ABC Elite (#PK-6100; Vector Laboratories, Burlingame, CA) and diaminobenzidine (DAB; #TA-125-QHDX; Thermo Fisher Scientific) reagents. Antibodies were diluted in Thermo Antibody diluent (#TA-125-ADQ), and all washes were performed with 0.05M Tris + 0.05% TWEEN-20. All sections were counterstained with hematoxylin.

A negative control (no-primary antibody) slide consisting of human umbilical vein endothelial cells (HUVECs) grown on chamber slides was included in each batch of stained breast tissue to control for non-specific binding of the secondary antibody. HUVECs (ATCC, Manassas, VA) maintained in EGM-2 culture medium supplemented with BulletKit reagents (Lonza, Walkersville, MD) were seeded at a density of 50,000 cells/well in 1 well of a 4-well chamber slide (BD Falcon, Franklin Lakes, NJ), and permitted to grow for 3 days. Slides were then fixed with 4% paraformaldehyde, and stained (1 slide per batch of tissue) according to the protocol described above.

4.3.3. Development of digital algorithm

Stained slides were scanned into high-resolution digital images using the Aperio ScanScope CS system (Aperio Technologies, Vista, CA) at a magnification of 20x. Tissue aberrations (e.g., large folds, surgical ink) and areas of extensive non-specific staining were

excluded via annotation with Aperio ImageScope software. All annotations were made by an investigator blinded to patient demographic information and other tissue characteristics. Annotated images were then imported into Definiens Architect XD version 2.7.0 for analysis with Definiens Tissue Studio version 4.4.2 (Cambridge, MA). Briefly, a training set consisting of 30 randomly selected slides was constructed, and the tissue and glass components of each specimen were segmented (**Figure 4.1A-B)**. A Tissue Studio Cellular Analysis Solution capable of detecting and classifying IHC-stained vasculature was then tuned to identify DAB^+ (i.e., $CD31^+$) regions. Importantly, given reports that capillaries average 8 μm in diameter [213], we trained the algorithm to exclude stained objects with cross-sectional areas of <50 μm^2. High-magnification views of the tissue area outlined in **Figure 4.1A** are shown in **Figures 4.1C-E** to illustrate vascular detection. The algorithm first detects "entire" blood vessels without regard to underlying vascular structure, which can be classified according to user-defined or software-default size categories if desired (**Figure 4.1D**). The algorithm then partitions each vascular object into "wall" and "lumen" components as applicable (**Figure 4.1E**).

4.3.4. Algorithm validation

After the trained algorithm was applied to the entire slide set, digital images were manually reviewed for gross irregularities. Visual inspection suggested high accuracy in identifying vascular areas. However, we identified 75, predominantly stroma-rich and mixed-histology slides with faint staining for which the tissue and glass components were not reliably partitioned. Thus, the tissue vs. glass parameter was re-tuned for this subset of slides, leaving all vascular parameters unchanged. However, misclassification persisted in 42.7% of slides from this subset (11.5% of all study specimens), and deficits in vessel quantitation were detected during validation (see below; **data not shown**). Therefore, the original algorithm was utilized for all 279 slides, and future molecular epidemiologic

assessment of vessel histology will incorporate sensitivity analyses excluding these 75 slides with areas of problematic classification.

Vessel density and average vessel size were computed by the algorithm in an automated fashion. Custom SAS software scripts (version 9.4; SAS Institute, Cary, NC) were also generated to compute median vessel area, percent vessel area ($\frac{\text{total vessel area}}{\text{tissue area}} * 100$), and percent endothelial area ($\frac{\text{total vessel area - lumen area}}{\text{tissue area}} * 100$) using data exported from Definiens Tissue Studio "Image Object Tables," which contain quantitative data corresponding to every stained object in a given slide. Data obtained from these automated approaches were compared to results acquired from manual slide annotation. A validation set consisting of 33 randomly selected slides with 1-2 serial sections each was constructed and each slide was manually annotated at high magnification using Aperio ImageScope software, with each annotation layer representing a different tissue component (**Figure 4.2**). Only structures with 2 or more nuclei were annotated to minimize the inclusion of $CD31^+$ leukocytes, and structures with cross-sectional areas of <50 μm^2 were excluded to facilitate agreement with the algorithm. Vessel density ($\frac{\text{number of vessels}}{\text{net tissue area}}$), median vessel area, average vessel area, percent vessel area ($\frac{\text{total vessel area}}{\text{net tissue area}} * 100$), and percent endothelial area ($\frac{\text{total vessel area - lumen area}}{\text{net tissue area}} * 100$) were then computed for each slide, with net tissue area equivalent to tissue area - (glass area + artifacts area) for all metrics. The agreement between automated and manually calculated values was evaluated with Pearson's correlation, percentage agreement, and Cohen's quadratic weighted kappa analyses using SAS and GraphPad Prism version 6.0 (GraphPad Inc, La Jolla, CA).

4.4. Results

4.4.1. Evaluation of algorithm performance: comparison to manual annotation

To evaluate algorithm performance, we first conducted correlation analyses wherein automated data from 33 randomly selected slides was compared to that acquired from manual annotation. Correlation analyses for each vascularity metric, as well as tissue area, are presented in **Figures 4.3**. Automated and manually derived tissue areas were strongly correlated (Pearson's correlation coefficient, r = 0.8936) despite the presence of tissue-glass misclassifications in 15.2% (5/33) of slides in the validation set (**Figure 4.3A**). In addition, moderate associations were observed between automated and manually computed vessel density (r = 0.5559), median vessel size (r = 0.4894), and average vessel size (r = 0.5626) (**Figure 4.3B-D**). Automated and manually derived percent vascular area (r = 0.2697) and percent endothelial area (r = 0.2397) were weakly correlated (**data not shown**) and will be excluded from future studies. Moreover, the dynamic range of these latter parameters was generally limited (range: 0-4), indicating that they are unlikely to be biologically meaningful.

To explore possible explanations for the observed variability between automated and manually computed vascular metrics, we considered that algorithm performance may vary in association with tissue histology and classified each slide in the validation set as "fibrous," "fatty," or "mixed". However, these adjustments for tissue composition did not uniformly improve overall agreement between automated and manually calculated vascularity metrics (**data not shown**).

We further assessed algorithm performance by dividing the automated and manual measurements for each vascular metric (vessel density, and median and average vessel size) into quartiles, and calculating the percent agreement between quartile assignments (**Tables 4.3**-**4.5**). When perfect agreement was required (grey cells in **Tables 4.3**-**4.5**), the percent agreement between automated and manual metrics equaled 48.5% for all 3

vascular parameters. Due to the heterogeneity of our datasets, we then calculated percent agreement after dichotomizing the data for each metric above and below the median (thick cell outlines in **Tables 4.3**-**4.5**). Percent agreement between quartile assignments increased to 70.0% for vessel density (quadratic-weighted Cohen's κ: 0.4748), and to 75.8% for both median and average vessel size (quadratic-weighted Cohen's κ: 0.4878 and 0.5022, respectively).

4.4.2. Distributions of tissue vascularity metrics

Having gained a comprehensive understanding of algorithm performance vs. manual annotation, we sought to characterize the biologic variability of each metric across the entire study slide set (n = 279 specimens). Histograms depicting the distribution of each metric are presented in **Figure 4.4**. The vessel density distribution exhibited a leftward skew, with the majority of data points residing between 0 and 125 vessels/mm^2 (**Figure 4.4A**). Data pertaining to median vessel size approximated a normal distribution (**Figure 4.4B**); however, that of average vessel size exhibited a leftward skew and substantially larger range (~100-700 μm^2 [average] vs. 75-150 μm^2 [median]; **Figure 4.4C**). We also plotted the distribution of percent vessel area and percent endothelial area, and confirmed the limited dynamic range of these metrics across the entire slide set (~0-8; **data not shown**).

4.5. Discussion

A small number of previous studies [116, 117] has characterized the vascular features of normal breast tissue. However, these studies only reported data from a small or unspecified number of women, and one study [117] only consented women aged 18-29 years. Therefore, little is known about: 1) whether vascular characteristics of normal human

breast tissue vary in association with diverse demographic factors; and 2) how the vascular features of histologically normal tissue adjacent to breast cancers may vary in accordance with corresponding tumor subtypes and in association with established breast cancer risk factors. To address these knowledge gaps, we generated a novel, high-throughput algorithm tuned to quantitate $CD31^+$ vasculature in histologically normal breast tissue from women with breast cancer. This algorithm was applied to a set of 279 specimens from 228 women, and, to our knowledge, represents the largest, most comprehensive analysis of normal breast vascular content reported to-date.

Our method was developed via integration of high-throughput digital technology and manual review. First, prior to tuning the algorithm, we minimized the inclusion of tissue aberrations and artifacts with potential to substantially misrepresent vascular content and phenotypes. In the second cycle of manual review, performed after applying the algorithm to all 279 specimens, we examined each digitally annotated slide for gross irregularities. Finally, automated and manually computed vessel parameters were directly compared. Evaluation of vascular characteristics in the 33-slide validation set revealed that, compared to manual annotation, the algorithm tended to overestimate vessel density and underestimate both median and average vessel size. However, these estimates were quantitatively highly correlated with the manual estimates and can be objectively and reproducibly estimated, and visual inspection suggested high accuracy in identifying vascular regions. The observed discrepancies appeared to primarily arise from the inability of the algorithm to discern objects with staining intensities below a certain threshold. Large vessels, particularly those sectioned in an oblique fashion, exhibited areas of faint and/or non-continuous endothelial cell staining and were partitioned by the algorithm into multiple smaller structures. In contrast, overarching vessel structure was more faithfully captured during manual annotation, leading to relative reductions in vessel density and increases in vessel size. Despite these differences, automated and manually computed parameters

exhibited moderate concordance according to widely accepted benchmarks for interpretation of the Cohen's κ statistic [214]. Nevertheless, future molecular epidemiologic assessment of this dataset (see below) will include sensitivity analyses excluding samples with areas of problematic classification.

The data obtained from this method will be applied in the context of a molecular epidemiologic study to characterize vascular content (vessel density) and phenotypes (median vessel size) in cancer-adjacent normal breast. Median, as opposed to average, vessel size was selected for use in future analyses because the data for this parameter across all study specimens approached a normal distribution. Samples from NBS are well annotated with respect to clinical features and patient demographic data, enabling studies of how vascular features vary with the intrinsic subtype of the corresponding tumor, as well as in association with tissue histology and established breast cancer risk factors. Ultimately, we anticipate that this work will reveal subtype-specific differences in the vascular properties of cancer-adjacent breast, and provide insight into factors that may contribute to observed differences in local tumor recurrence rates.

4.6. Figures

Figure 4.1. Example of vascular algorithm output

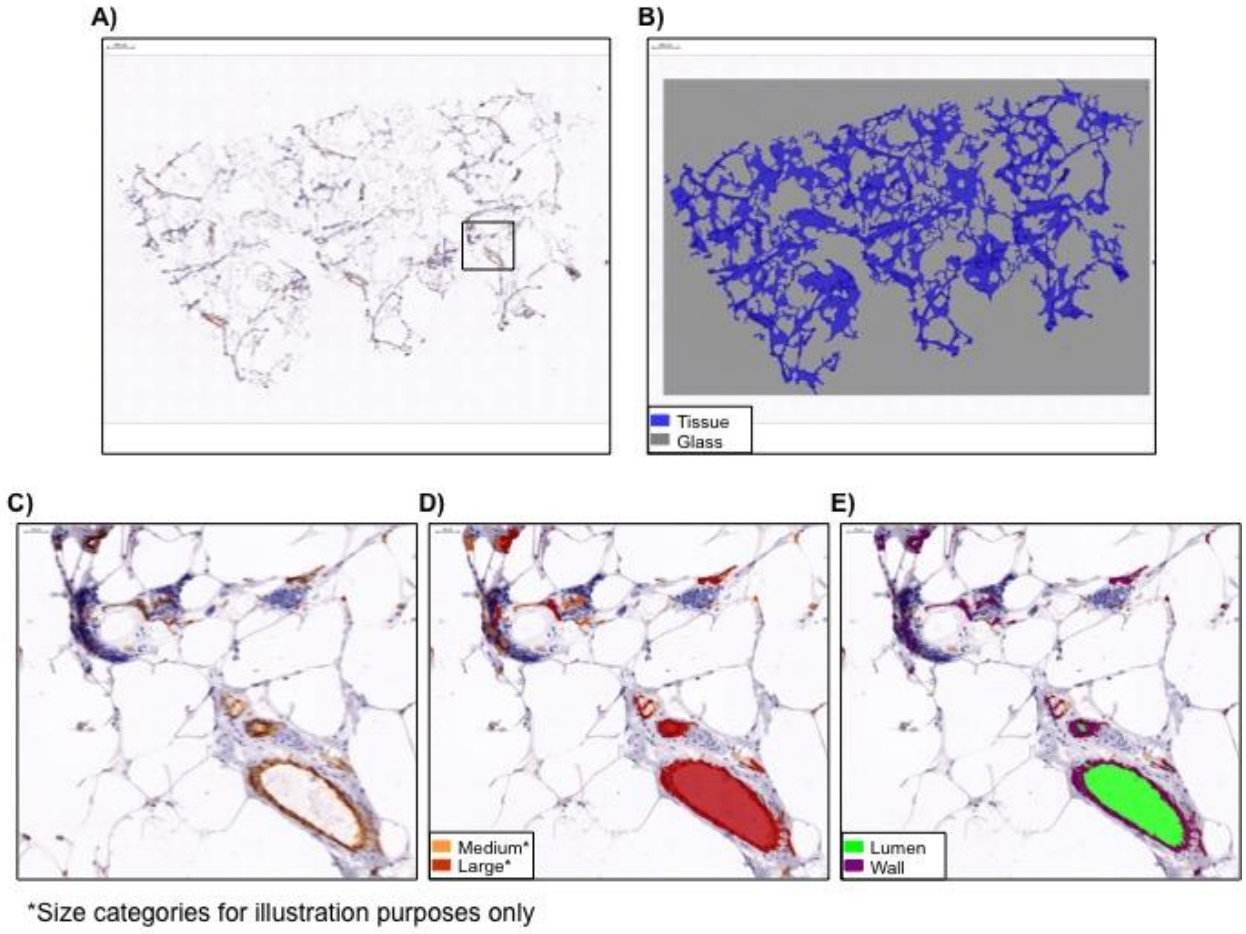

A) Histologic section of adipose-rich cancer-adjacent breast immunohistochemically stained for CD31. The black rectangle indicates the location presented at high magnification in **C-E**. Scale bar = 500 μm. **B)** Digital rendering of tissue (blue) vs. glass (grey) components. Scale bar = 500 μm. **C)** High-magnification image of the location outlined in **A**. Brown indicates areas of CD31-positivity. **D)** Digital rendering of vessel identification algorithm; in this output, no distinction is made between vessel lumena and walls. Vessel size categories (e.g., medium [orange]; large [red]) are shown here for illustration purposes only. **E.** Digital rendering of vessel identification algorithm; this output can distinguish between vessel walls (purple) and vessel lumena (green). Scale bar for **C-E** = 50 μm.

Figure 4.2. Representative manual annotations for algorithm validation slide set

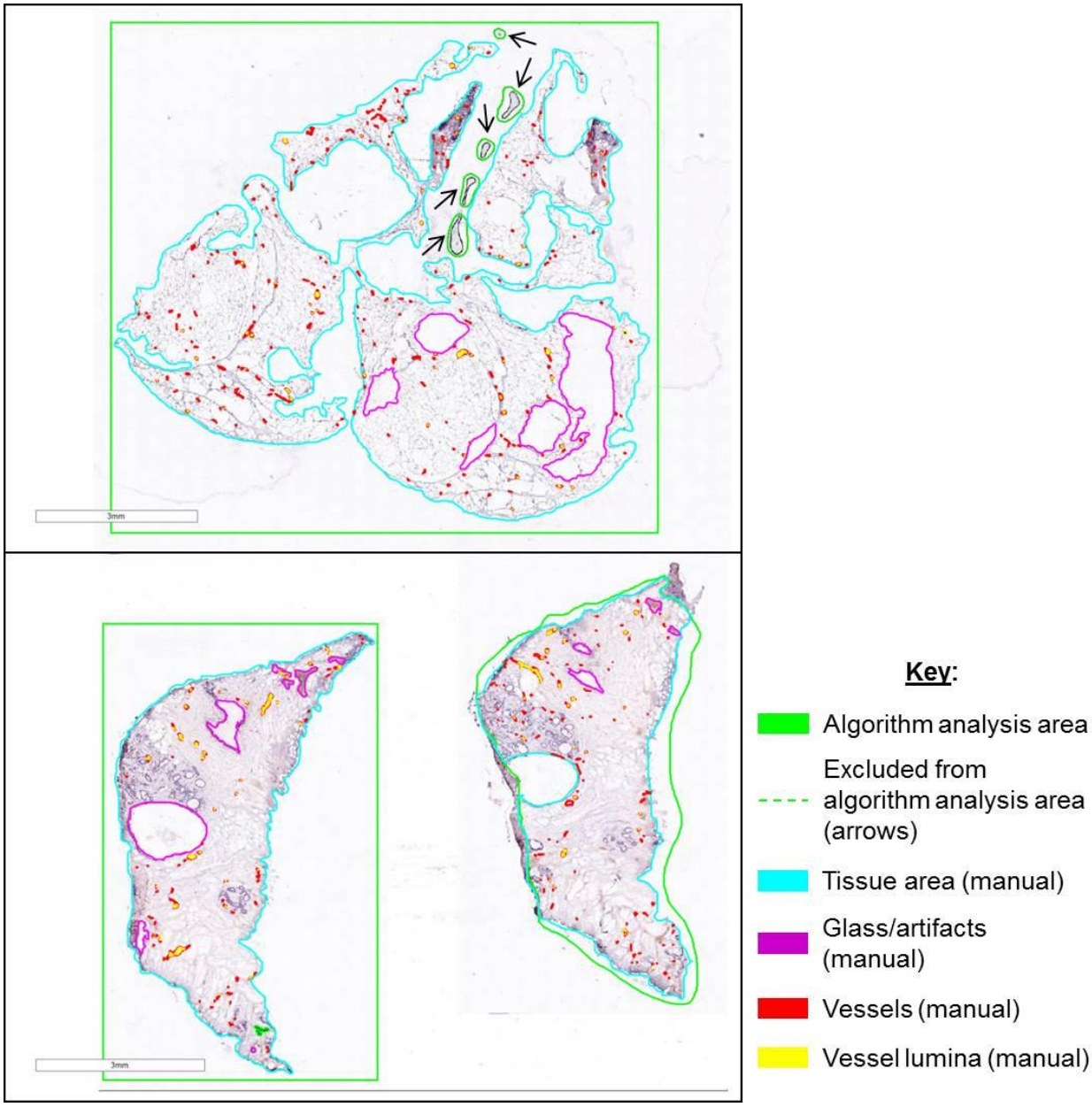

Digital images of adipose- (top) and stroma-rich (bottom) tissue specimens overlaid with the layers denoting the algorithm analysis area (green layer) and manually segmented tissue compartments. The blue, magenta, red, and yellow layers denote manually annotated tissue area, glass and artifacts, vessels, and vessel lumina, respectively. In the top slide, air bubbles outlined in dashed green lines (indicated with arrows) were excluded from the algorithm analysis area. Scale bar for both panels = 3 mm.

Figure 4.3. Correlations between automated and manually computed vessel metrics across the 33-slide validation set

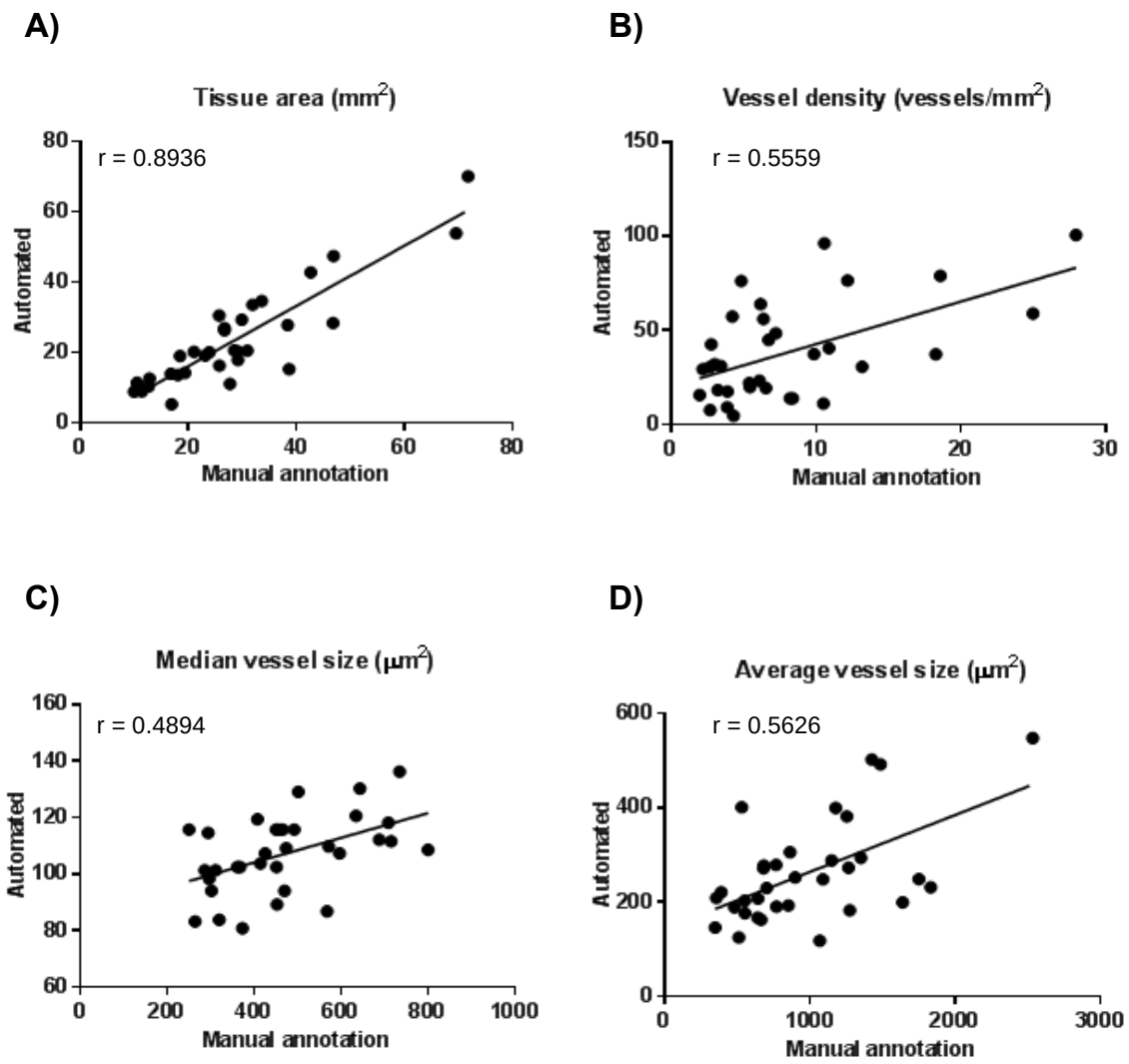

Pearson's correlation coefficients and lines of best fit comparing automated and manually computed tissue and vascular parameters for the 33-slide validation set, including **A)** tissue area; **B)** vessel density; and **C)** median and **D)** average vessel size.

Figure 4.4. Distribution of tissue vascularity metrics across the entire 279-slide set

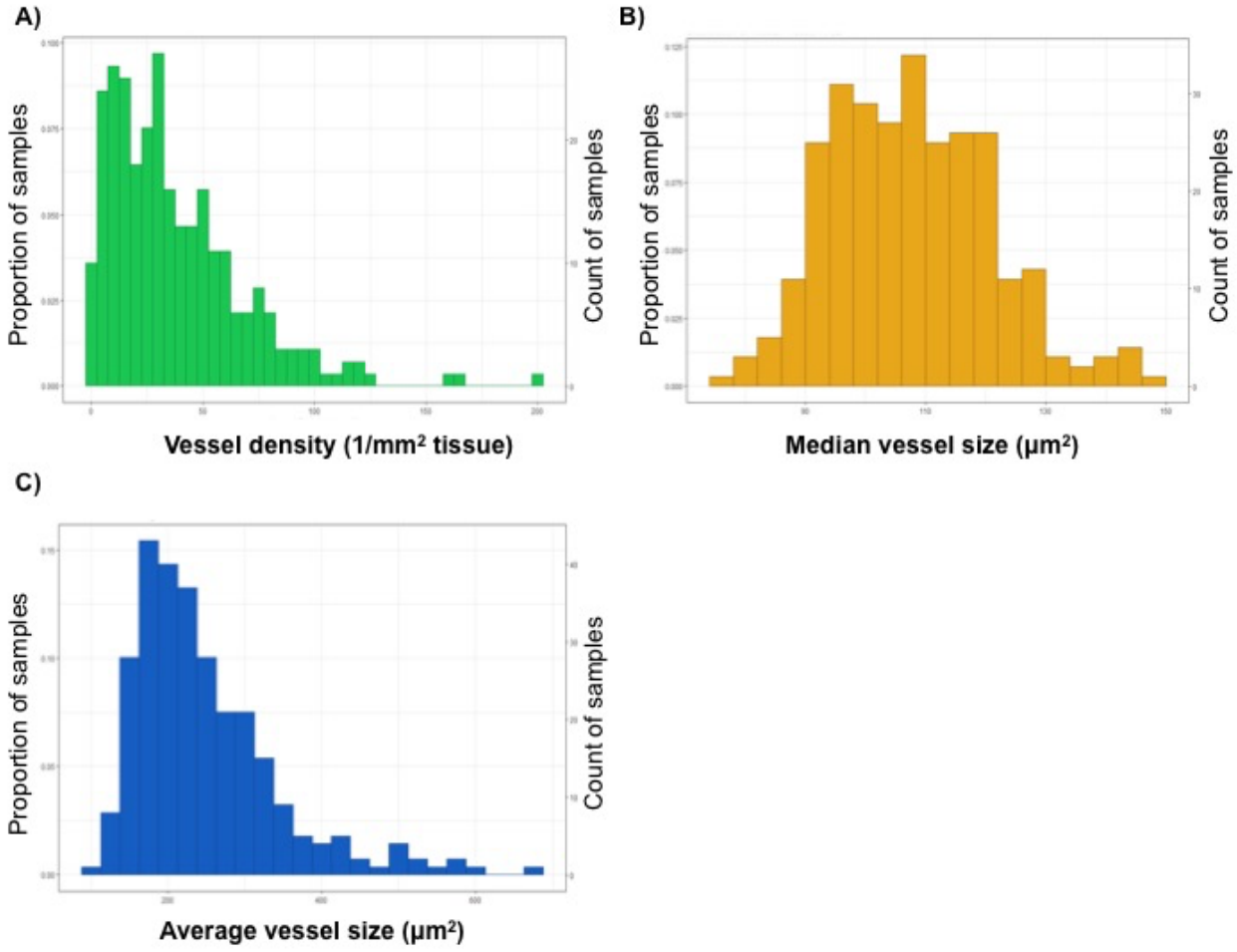

Distribution (sample proportion and count) of **A)** vessel density (1/mm^2 of tissue), **B)** median vessel size, and **C)** average vessel size across the entire study slide set (n = 279 slides).

4.7. Tables

Table 4.1. Distribution of patient demographic factors (n = 228)

	Breast cancer diagnosis			No cancer history
	Invasive disease	**No active disease***	***In situ* disease**	**Benign condition**
Total n (%)	180 (78.9)	2 (0.9)	29 (12.7)	17 (7.5)
Age at surgery ± SD	53.8 ± 12.3	49.5 ± 7.7	57.3 ± 12.0	46.7 ± 15.4
Race				
White	110 (61.1)	2 (100.0)	21 (72.4)	9 (52.9)
Black	56 (31.1)	0 (0.0)	3 (10.3)	7 (41.2)
Other/Not reported	14 (7.8)	0 (0.0)	5 (17.2)	1 (5.9)
BMI ± SD (kg/m^2)	29.4 ± 6.9	33.8 ± 7.7	25.7 ± 5.7	28.4 ± 8.3

*Patients with a prior breast cancer history were diagnosed and treated with complete response at least one year prior to the consented surgery, and had no active disease at the time of surgery.

Table 4.2. Distribution of tumor characteristics among breast cancer patients (n = 209)

	n	%
Stage		
0	29	13.9
1	93	44.5
2	56	26.8
3	22	10.5
4	6	2.9
Missing	3	1.4
Grade		
1	40	19.1
2	81	38.8
3	85	40.7
Missing	3	1.4
Tumor size		
≤2 cm.	113	54.1
>2-5 cm.	68	32.5
>5 cm.	28	13.4
Lymph node status		
Positive	70	33.5
Negative	116	55.5
Missing	23	11.0
ER status		
Positive	146	69.9
Borderline	4	1.9
Negative	54	25.8
Missing	5	2.4
PR status		
Positive	121	57.9
Borderline	6	2.9
Negative	76	36.4
Missing	6	2.9
HER2 status*		
Positive	34	18.9
Negative	138	76.7
Missing	8	4.4

*Among invasive cases only.

Table 4.3. Agreement between automated and manually computed vessel density in the 33-slide validation set

		Automated				
		Q1	**Q2**	**Q3**	**Q4**	**Totals**
Manual	**Q1**	4	3	2	0	**9**
	Q2	2	3	0	3	**8**
	Q3	3	1	4	0	**8**
	Q4	0	1	2	5	**8**
	Totals	**9**	**8**	**8**	**8**	

Quadratic-weighted Cohen's κ: 0.4748 (95% CI: 0.1738 - 0.7830)

Percent agreement (perfect agreement): 48.5%

Percent agreement (dichotomization above and below the mean): 70.0%

Q: quartile; CI: confidence interval. Shaded cells indicate perfect agreement between automated and manually calculated metrics, whereas cells outlined with thick gridlines demonstrate dichotomization above and below the median.

Table 4.4. Agreement between automated and manually computed median vessel size in the 33-slide validation set

		Automated				
		Q1	**Q2**	**Q3**	**Q4**	**Totals**
Manual	**Q1**	5	2	2	0	**9**
	Q2	2	4	1	1	**8**
	Q3	2	0	3	3	**8**
	Q4	0	2	2	4	**8**
	Totals	**9**	**8**	**8**	**8**	

Quadratic-weighted κ: 0.4878 (95% CI: 0.1832 - 0.7924)

Percent agreement (perfect agreement): 48.5%

Percent agreement (dichotomization above and below the mean): 75.8%

Q: quartile; CI: confidence interval. Shaded cells indicate perfect agreement between automated and manually calculated metrics, whereas cells outlined with thick gridlines demonstrate dichotomization above and below the median.

Table 4.5. Agreement between automated and manually computed average vessel size in the 33-slide validation set

		Automated				
		Q1	**Q2**	**Q3**	**Q4**	**Totals**
Manual	**Q1**	5	3	0	1	**9**
	Q2	2	3	3	0	**8**
	Q3	1	0	4	3	**8**
	Q4	1	2	1	4	**8**
	Totals	**9**	**8**	**8**	**8**	

Quadratic-weighted κ: 0.5022 (95% CI: 0.1960 - 0.8084)

Percent agreement (perfect agreement): 48.5%

Percent agreement (dichotomization above and below the mean): 75.8%

Q: quartile; CI: confidence interval. Shaded cells indicate perfect agreement between automated and manually calculated metrics, whereas cells outlined with thick gridlines demonstrate dichotomization above and below the median.

CHAPTER 5

INTEGRATIVE SUMMARY AND FUTURE DIRECTIONS

5.1. Summary

With a focus on characterizing the unique features of TNBC microenvironments, this body of work laid a strong, broad foundation for understanding how breast tissue stroma varies in association with the intrinsic subtype of the corresponding tumor. Our studies highlight the complexity of TNBC microenvironments by profiling three distinct stromal cell constituents (fibroblasts, myeloid cells, and vasculature), and have relevance to multiple stages of disease (pre-malignant, invasive, and recurrent TNBC). In Chapter 2, profiling of cell-cell interactions in pre-malignant BBC revealed that fibroblasts induced p53-dependent morphologic changes in benign and atypical hyperplastic epithelium that correlated with distinct patterns of transcription. In Chapter 3, we demonstrated that suppression of glycolysis in myeloid cells impeded CLBC progression, potentially through the regulation of inflammation in both normal and tumor microenvironments. Finally, in Chapter 4, we developed a digital algorithm designed to quantitate $CD31^+$ vasculature in histologically benign tissue from breast cancer patients, with the long-term goal of understanding how cancer-adjacent vascular content and phenotypes relate to differential recurrence rates among tumor subtypes. Collectively, this work addressed important questions relating to stromal-epithelial interactions in TNBC, identifying previously uncharacterized phenotypic, transcriptional, and proteomic responses of cancer cells to their microenvironments. Additional studies to uncover epidemiologic associations that directly relate to stromal-

epithelial interactions in human tissue are also underway (see section **5.4**). The goal of the present Chapter is to describe the overarching translational relevance of this dissertation, and to broadly demonstrate how the complementary experimental models used herein can be integrated in future work (**Figure 5.1**).

5.2. Importance and translational implications of studying pre-invasive and malignant stromal-epithelial interactions

The tissue microenvironment been described as a contextual double-edged sword. Physiologic microenvironments can restrain or even revert malignant phenotypes, whereas aberrant, permissive microenvironmental signals destabilize tissue architecture to promote carcinogenesis and malignant progression [59]. That the normal microenvironment acts as a barrier to carcinogenesis implies that tumorigenic cells must *acquire*, and that normal microenvironments *select for*, mutations and associated adaptive phenotypes (e.g., enhanced proliferation and/or invasion) that improve biologic fitness [215].

Studies of heterotypic interactions during early stages of tumor development are important for understanding how pre-malignant cells overcome microenvironmental constraints. In Chapter 2, we characterized the evolution of stromal-epithelial interactions during progression to malignancy and identified novel morphogenetic responses of pre-invasive breast epithelium to fibroblast co-culture. Responses to co-culture were dependent upon genetic context (i.e., epithelial p53 status), with p53-deficient cells displaying accelerated adaptive changes (increased asphericity/local invasion) relative to p53-sufficient controls. Furthermore, identification of gene expression patterns correlating with morphology provides insight into signals that induce or sustain adaptive epithelial phenotypes, and may

lead to the identification of targetable interactions for BBC prevention in susceptible populations.

Invasive cancer cells possess an array of adaptive phenotypes that have enabled them to successfully overcome stromal barriers to carcinogenesis. In turn, aberrant paracrine communication patterns between cancer cells and the surrounding tissue facilitate development of a permissive stroma that further perpetuates tumor progression [215]. Elucidation of stromal-epithelial interactions in established TNBCs, such as those described in Chapter 3, is crucial for the development of novel therapeutic targets for this clinically intractable tumor subtype. Similarly, although the M-Wnt cells used in our study only invade locally within the mammary fat pad, studies of heterotypic interactions can also provide important insights into the biology of metastatic tumors: identification of stromal factors that retain metastatic cancer cells in a latent state, as well as signals enabling them to emerge from dormancy, will be crucial for preventing disease relapse [59, 216, 217]. Whether or not contextual metastatic cues vary across breast cancer subtypes is an important area for future study.

5.3. Limitations

5.3.1. 3D cultures

Although 3D co-cultures facilitate contextually relevant studies of tissue biology, particularly compared to cells cultured in a monolayer on plastic, the inclusion of a limited number of cell types (e.g., cancer cells and one stromal cell constituent) implies that these models fail to recapitulate the full dynamic complexity of living tissues. Similarly, we also acknowledge that immortalized stromal cells, such as the hTERT-immortalized fibroblasts used herein, do not reflect the full spectrum of biologic variability associated with primary

human cells. Primary fibroblasts from each stage of pre-malignant breast disease represented in our study would offer the greatest degree of physiologic relevance; however, tissue of suitable quality for live-cell isolation is not readily available. Thus, co-cultures are amenable to the study of a single or small number of signaling pathways in relative isolation and under relatively homogeneous conditions, but more complex model systems and related analytical approaches are required to understand how cell-cell interactions are altered in more heterogeneous environments. While OCT may be technically amenable to analyses of this nature, the non-high-throughput nature and complex technologic requirements of this method currently preclude its widespread use in the field. Therefore, development of more streamlined OCT analysis procedures and novel bioinformatic tools for increasingly complex models of TNBC microenvironments is critical.

5.3.2. Orthotopic tumor model

A limitation of orthotopic tumor models in general is that the natural history of these cancers is substantially different from that of human disease. Injection of mice with tumor cells represents an “artificial” etiology, whereas human carcinogenesis occurs in part due to genetic predisposition and/or acquisition of somatic mutations from environmental exposures. Orthotopic models also typically require greater technical skill, particularly compared to subcutaneous models, as cells must be precisely injected or even surgically implanted into the desired tissue [218]. Despite these limitations, orthotopic models afford many advantages to studies of tumor microenvironments, including: 1) the ability to inject the same number of cancer cells into each animal, thus enabling experimental control; 2) relatively rapid tumor development (typically days to weeks vs. weeks to months for spontaneous cancer models); and 3) physiologic relevance with respect to site of tumor growth; i.e., tumors develop in the stroma context of the tissue from which they were originally derived.

Given that CLBC was only recently recognized [48], there is an urgent need to better characterize the mutational profiles of human cancers to enable more physiologically relevant studies of tumor-stromal interactions, particularly in *in vivo* settings. Previous studies in animal models suggest that loss-of-function mutations in *TP53* may be important in the biology of this subtype. For example, Knight et al. recently reported a GEMM of spontaneous breast cancer wherein both cMET overexpression and p53 loss in the mammary epithelium synergize to promote tumors that pathologically resemble human CLBCs [75]. In addition, overexpression of prolactin in the mammary epithelium of *TP53*-null mice accelerated the formation of tumors with claudin-low histopathology [219]. However, as the M-Wnt cells used in Chapter 3 are *TP53*-wild-type, additional genetic factors are likely to play a role in CLBC development and progression. Data pertaining to BBCs may provide additional clues; however, we must caution that the documented molecular differences between BBCs and CLBCs [12, 49, 51] imply that results from studies of one subtype may not be broadly applicable to the other.

5.3.3. Human tissue model

Results from the NBS must be interpreted in light of its hospital-based nature. Participants are more likely to reflect the population of Chapel Hill, NC and surrounding areas, with overall higher socioeconomic status and better access to healthcare than the general US population. However, given the limited number of previous studies pertaining to normal and cancer-adjacent breast vasculature, as well as the qualitative nature thereof and small number of patients therein, our study is an important step to understanding how tumor-adjacent vasculature varies in association with tumor subtype and associated risk factors. Nevertheless, it will be important to validate our results in additional populations. We must also acknowledge that a general limitation of digital histology algorithms is that they must often be tuned to individual slide sets due to variability in tissue preservation methods

(frozen vs. FFPE), tissue topologies, colorimetric substrates, and staining intensities, potentially precluding their use in clinical settings where rapid specimen assessment is required. Furthermore, algorithms also exhibit limited flexibility and analyses are bound by a finite set of parameters. To circumvent these constraints, novel machine/deep learning modalities are being developed for a variety of biologic applications, including using digital histology images to diagnose, subtype, and prognose breast cancers [220-223]. Ultimately, there is much to be learned from molecular research of human tissue, to which advancements in a wide range of digital histopathology techniques will undoubtedly contribute.

5.4. Avenues for future research: methodologic complementarity

A natural extension of the work presented in Chapter 2 is to characterize p53-dependent fibroblast-epithelial interactions in the context of malignant BBC. To this end, similar 3D morphogenesis and gene expression assays to those described herein are currently ongoing, leveraging a panel of well-characterized isogenic (p53-sufficient and -deficient) invasive breast cancer cell lines. Incorporation of both BBC (HME-CC, SUM102) and luminal (MCF-7, ZR-75-1) cell line pairs in this study will also facilitate identification of subtype-specific microenvironmental interactions, as opposed to generalized, stereotypic responses of breast cancer cells to fibroblast co-culture. Interestingly, an invasive MCF10 line (MCF10CA1a) with a spontaneous activating mutation in *PIK3CA* has also been reported [224], and creation of a p53-deficient line could enable investigations of malignant stromal-epithelial crosstalk on an otherwise isogenic background.

Pathway-focused analyses of co-cultures can be further tested in the context of human studies. In particular, the rapid proliferation of publically available datasets facilitates

validation of gene signatures (specific groups of genes that vary in response to a given biologic stimulus) or other transcriptional findings in human patients at minimal cost. Integration of these techniques is critical for the identification and validation of novel risk factor, diagnostic, prognostic, and predictive biomarkers in breast cancer.

The predominant question raised in Chapter 3 is mechanistic in nature: how precisely does loss of myeloid *Glut1* impair CLBC progression? Our study points to a role for myeloid *Glut1*-mediated modulation of inflammatory processes, but these interactions must be further evaluated in a mechanistic setting. Integration of additional animal models and cell-based assays will have utility for exploring these novel hypotheses. As one example, to test the hypothesis that increased immunosurveillance (i.e., altered effector T cell function) underlies the delayed tumor progression observed in $Glut1^{M-/-}$ compared to $Glut1^{MFl/Fl}$ mice, $Glut1^{M-/-}$ animals could be crossed to syngeneic C57BL/6J *Rag1* null mice; the resulting animals would harbor $Glut1^{-/-}$ myeloid cells and would lack mature T (and B) cells (https://www.jax.org/strain/002216). Normalization of M-Wnt tumor progression patterns in $Glut1^{M-/-}$; $Rag1^{-/-}$ mice to $Glut1^{MFl/Fl}$ or near-$Glut1^{MFl/Fl}$ levels would implicate a role for Glut1-dependent myeloid cell-T cell interactions in regulating CLBC progression. *In vitro* T cell-stimulation assays could also be performed to test this hypothesis in the context of a smaller scale, more tractable experimental unit. Incubation of cytotoxic T-cells with tumor-associated macrophages from mice of both genotypes, followed by incubation of primed T-cells with cultured M-Wnt cells, could enable direct assessment of T cell cytotoxicity in the context of $Glut1^{M-/-}$ and $Glut1^{MFl/Fl}$ microenvironments. Importantly, however, these cell-based assays would necessitate extensive study of primary cell phenotypes to facilitate experimental reproducibility, as well as a careful evaluation of culture conditions to ensure primary cell survival for the duration of the assay.

An additional area for future research with relevance to Chapter 3 relates to the concept of reverse Warburg metabolism. In this model, activated CAFs undergo *Glut1*-

dependent aerobic glycolysis and secrete lactate into the tumor microenvironment, in turn "feeding" cancer cells and enabling cancer cell oxidative mitochondrial metabolism [225, 226]. This stromal-epithelial "lactate shuttle" has been reported to facilitate prostate tumor growth [227] and protect breast cancer cells from hypoxia-mediated apoptosis [226], and may underlie tumor-promoting effects of CAFs in colon cancer and melanoma models [228]. Evidence of the reverse Warburg effect has also been detected in human breast and prostate tumors, wherein it is associated with increased recurrence rates and high tumor stage, respectively [226, 229]. Interestingly, our laboratory has previously demonstrated that BMDMs from *Glut1*$^{M-/-}$ relative to *Glut1*$^{MFl/Fl}$ mice produce lower concentrations of lactate in response to pro-inflammatory lipopolysaccharide/interferon gamma (LPS/IFNγ) stimulation [183]. Accordingly, important avenues for future research are to determine if *Glut1*$^{M-/-}$ MFP macrophages also produce less lactate in response to pro-inflammatory stimuli, and to address whether macrophages in tumor stroma also contribute to the growth-promoting effects of reverse Warburg metabolism in cancer.

Finally, as aforementioned, the algorithm described in Chapter 4 will be applied to molecular epidemiologic studies of human tissue. Samples in the NBS are clinically annotated with respect to both demographic and life exposure data, enabling thorough assessment of how vascular content and phenotypes vary in association with TNBC tumor characteristics (e.g., grade, stage, size, and lymph node status) and risk factors (e.g., young age/premenopausal status, African American race, obesity, parity, and never having breastfed) [19, 22, 31, 32, 41]. Furthermore, as molecular characteristics of frank breast tumors are strongly reflected in histologically normal tissue located within 1 cm of the primary lesion, but are attenuated or absent at distances of 3 and 5 cm [230-232], it will also be important to consider the distance of each cancer-adjacent tissue sample from the tumor.

In future work, mechanisms by which the vasculature influences both primary and metastatic tumor behavior should be characterized. Animal tumor models will be particularly

important to contextualizing these studies to epidemiologic associations identified with the vascular algorithm, particularly those that are challenging or even impossible to model in cell-based systems (e.g., parity). Interactions identified in tissue-level studies can be further dissected *in vitro*, wherein utilization of breast-specific endothelial cells will be crucial to maintaining the physiologic relevance of the system [111, 112, 116].

In conclusion, the work presented herein used a broad range of molecular tools to identify novel phenotypic, transcriptional, and tissue-level responses of TNBC cells to a diverse array of microenvironmental constituents. Continued, integrated use of these complementary model systems is vital to further enhancing our understanding of stromal-epithelial interactions in TNBC, and to conclusively identifying novel therapeutic targets for this intractable tumor subtype.

5.5. Figures

Figure 5.1. Integration of complementary model systems furthers knowledge of TNBC microenvironments

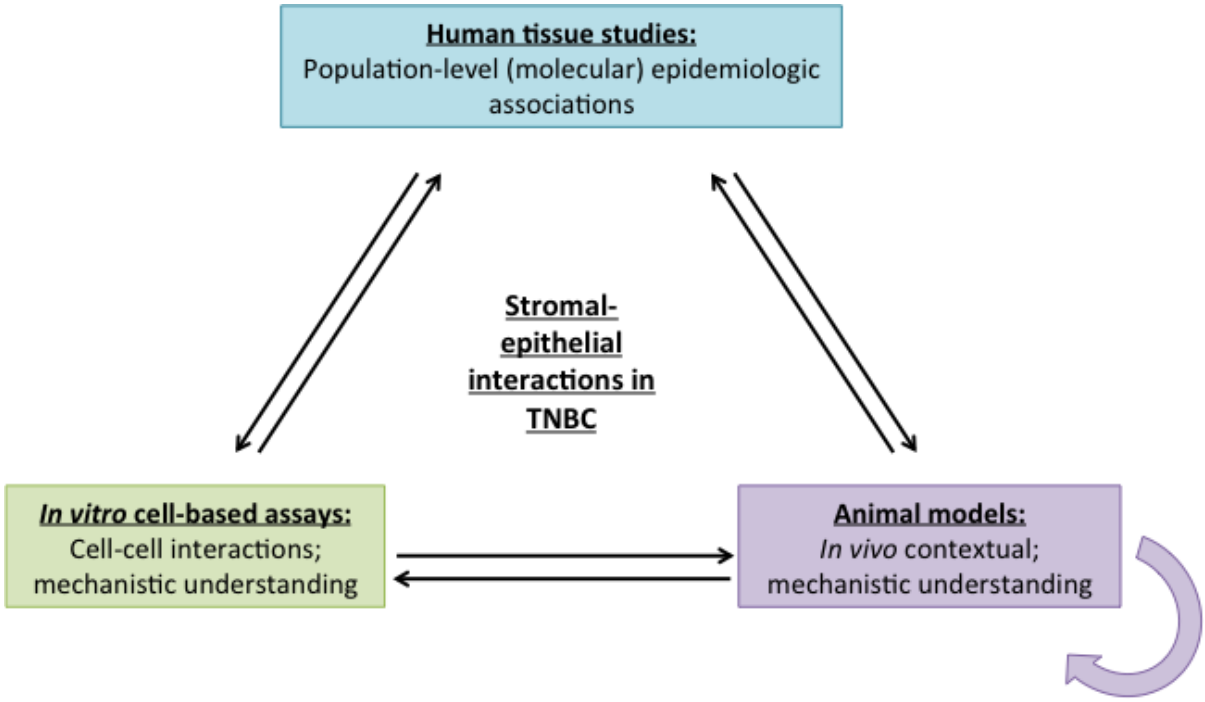

A number of complementary model systems are available for the study of tissue microenvironments. Epidemiologic associations revealed by human studies can be mechanistically probed “in-context” with animal models, or in cell-based assays that afford a highly controlled setting. *In vitro* assays that identify novel stromal-epithelial communication patterns or improve mechanistic understanding of previously described interactions can be further examined in the setting of a complex living tissue, whereas tissue-level phenomena in animals can be dissected into smaller, more tractable experimental units *in vitro*. Moreover, hypothesis-generating work in animals can be supplemented by incorporating additional genetically engineered *in vivo* models that improve mechanistic understanding. Finally, results from studies of stromal-epithelial interactions in both cell-based and animal models can be applied in epidemiologic resources to determine the relevance of a given interaction to human populations.

REFERENCES

1. Dontu, G., et al., *Stem cells in normal breast development and breast cancer.* Cell Prolif, 2003. **36 Suppl 1**: p. 59-72.

2. Hennighausen, L. and G.W. Robinson, *Signaling pathways in mammary gland development.* Dev Cell, 2001. **1**(4): p. 467-75.

3. Moumen, M., et al., *The mammary myoepithelial cell.* Int J Dev Biol, 2011. **55**(7-9): p. 763-71.

4. Stein, T., N. Salomonis, and B.A. Gusterson, *Mammary gland involution as a multi-step process.* J Mammary Gland Biol Neoplasia, 2007. **12**(1): p. 25-35.

5. Stanford, J.C., et al., *Efferocytosis produces a prometastatic landscape during postpartum mammary gland involution.* J Clin Invest, 2014. **124**(11): p. 4737-52.

6. Rosen, P.P., *Rosen's Breast Pathology*. 3rd ed. ed. 2008, Philadelphia: Wolters Kluwer/Lippincott Williams & Wilkins.

7. Twigger, A.J., et al., *Gene expression in breastmilk cells is associated with maternal and infant characteristics.* Sci Rep, 2015. **5**: p. 12933.

8. Gudjonsson, T., et al., *Myoepithelial cells: their origin and function in breast morphogenesis and neoplasia.* J Mammary Gland Biol Neoplasia, 2005. **10**(3): p. 261-72.

9. Siegel, R.L., K.D. Miller, and A. Jemal, *Cancer statistics, 2018.* CA Cancer J Clin, 2018. **68**(1): p. 7-30.

10. Perou, C.M., et al., *Molecular portraits of human breast tumours.* Nature, 2000. **406**(6797): p. 747-52.

11. Sorlie, T., et al., *Gene expression patterns of breast carcinomas distinguish tumor subclasses with clinical implications.* Proc Natl Acad Sci U S A, 2001. **98**(19): p. 10869-74.

12. Prat, A., et al., *Phenotypic and molecular characterization of the claudin-low intrinsic subtype of breast cancer.* Breast Cancer Res, 2010. **12**(5): p. R68.

13. Parker, J.S., et al., *Supervised risk predictor of breast cancer based on intrinsic subtypes.* J Clin Oncol, 2009. **27**(8): p. 1160-7.

14. Sotiriou, C., et al., *Breast cancer classification and prognosis based on gene expression profiles from a population-based study.* Proc Natl Acad Sci U S A, 2003. **100**(18): p. 10393-8.

15. Hennigs, A., et al., *Prognosis of breast cancer molecular subtypes in routine clinical care: A large prospective cohort study.* BMC Cancer, 2016. **16**(1): p. 734.

16. van 't Veer, L.J., et al., *Gene expression profiling predicts clinical outcome of breast cancer.* Nature, 2002. **415**(6871): p. 530-6.

17. Sweeney, C., et al., *Intrinsic subtypes from PAM50 gene expression assay in a population-based breast cancer cohort: differences by age, race, and tumor characteristics.* Cancer Epidemiol Biomarkers Prev, 2014. **23**(5): p. 714-24.

18. Prat, A., et al., *Molecular characterization of basal-like and non-basal-like triple-negative breast cancer.* Oncologist, 2013. **18**(2): p. 123-33.

19. Carey, L.A., et al., *Race, breast cancer subtypes, and survival in the Carolina Breast Cancer Study.* JAMA, 2006. **295**(21): p. 2492-502.

20. Cheang, M.C., et al., *Basal-like breast cancer defined by five biomarkers has superior prognostic value than triple-negative phenotype.* Clin Cancer Res, 2008. **14**(5): p. 1368-76.

21. Livasy, C.A., et al., *Phenotypic evaluation of the basal-like subtype of invasive breast carcinoma.* Mod Pathol, 2006. **19**(2): p. 264-71.

22. Millikan, R.C., et al., *Epidemiology of basal-like breast cancer.* Breast Cancer Res Treat, 2008. **109**(1): p. 123-39.

23. Nielsen, T.O., et al., *Immunohistochemical and clinical characterization of the basal-like subtype of invasive breast carcinoma.* Clin Cancer Res, 2004. **10**(16): p. 5367-74.

24. Stead, L.A., et al., *Triple-negative breast cancers are increased in black women regardless of age or body mass index.* Breast Cancer Res, 2009. **11**(2): p. R18.

25. Cozzo, A.J., A.M. Fuller, and L. Makowski, *Contribution of Adipose Tissue to Development of Cancer.* Compr Physiol, 2017. **8**(1): p. 237-282.

26. Yang, X.R., et al., *Associations of breast cancer risk factors with tumor subtypes: a pooled analysis from the Breast Cancer Association Consortium studies.* J Natl Cancer Inst, 2011. **103**(3): p. 250-63.

27. Dolle, J.M., et al., *Risk factors for triple-negative breast cancer in women under the age of 45 years.* Cancer Epidemiol Biomarkers Prev, 2009. **18**(4): p. 1157-66.

28. Kwan, M.L., et al., *Association of high obesity with PAM50 breast cancer intrinsic subtypes and gene expression.* BMC Cancer, 2015. **15**: p. 278.

29. Lennon, H., et al., *The Obesity Paradox in Cancer: a Review.* Curr Oncol Rep, 2016. **18**(9): p. 56.

30. Strulov Shachar, S. and G.R. Williams, *The Obesity Paradox in Cancer-Moving Beyond BMI.* Cancer Epidemiol Biomarkers Prev, 2017. **26**(1): p. 13-16.

31. Anderson, K.N., R.B. Schwab, and M.E. Martinez, *Reproductive risk factors and breast cancer subtypes: a review of the literature.* Breast Cancer Res Treat, 2014. **144**(1): p. 1-10.

32. Ma, H., et al., *Reproductive factors and the risk of triple-negative breast cancer in white women and African-American women: a pooled analysis.* Breast Cancer Res, 2017. **19**(1): p. 6.

33. Trivers, K.F., et al., *The epidemiology of triple-negative breast cancer, including race.* Cancer Causes Control, 2009. **20**(7): p. 1071-82.

34. Yang, X.R., et al., *Differences in risk factors for breast cancer molecular subtypes in a population-based study.* Cancer Epidemiol Biomarkers Prev, 2007. **16**(3): p. 439-43.

35. Li, C.I., et al., *Reproductive factors and risk of estrogen receptor positive, triple-negative, and HER2-neu overexpressing breast cancer among women 20-44 years of age.* Breast Cancer Res Treat, 2013. **137**(2): p. 579-87.

36. Phipps, A.I., et al., *Reproductive history and oral contraceptive use in relation to risk of triple-negative breast cancer.* J Natl Cancer Inst, 2011. **103**(6): p. 470-7.

37. Brouckaert, O., et al., *Update on triple-negative breast cancer: prognosis and management strategies.* Int J Womens Health, 2012. **4**: p. 511-20.

38. Dairkee, S.H., et al., *Immunolocalization of a human basal epithelium specific keratin in benign and malignant breast disease.* Breast Cancer Res Treat, 1987. **10**(1): p. 11-20.

39. Wetzels, R.H., et al., *Detection of basement membrane components and basal cell keratin 14 in noninvasive and invasive carcinomas of the breast.* Am J Pathol, 1989. **134**(3): p. 571-9.

40. Wada, T., et al., *Vimentin expression in benign and malignant lesions in the human mammary gland.* Anticancer Res, 1992. **12**(6B): p. 1973-82.

41. Bertucci, F., P. Finetti, and D. Birnbaum, *Basal breast cancer: a complex and deadly molecular subtype.* Curr Mol Med, 2012. **12**(1): p. 96-110.

42. Molyneux, G., et al., *BRCA1 basal-like breast cancers originate from luminal epithelial progenitors and not from basal stem cells.* Cell Stem Cell, 2010. **7**(3): p. 403-17.

43. Cancer Genome Atlas, N., *Comprehensive molecular portraits of human breast tumours.* Nature, 2012. **490**(7418): p. 61-70.

44. Holstege, H., et al., *BRCA1-mutated and basal-like breast cancers have similar aCGH profiles and a high incidence of protein truncating TP53 mutations.* BMC Cancer, 2010. **10**: p. 654.

45. Foulkes, W.D., et al., *Germline BRCA1 mutations and a basal epithelial phenotype in breast cancer.* J Natl Cancer Inst, 2003. **95**(19): p. 1482-5.

46. Sorlie, T., et al., *Repeated observation of breast tumor subtypes in independent gene expression data sets.* Proc Natl Acad Sci U S A, 2003. **100**(14): p. 8418-23.

47. Perou, C.M., *Molecular stratification of triple-negative breast cancers.* Oncologist, 2010. **15 Suppl 5**: p. 39-48.

48. Herschkowitz, J.I., et al., *Identification of conserved gene expression features between murine mammary carcinoma models and human breast tumors.* Genome Biol, 2007. **8**(5): p. R76.

49. Dias, K., et al., *Claudin-Low Breast Cancer; Clinical & Pathological Characteristics.* PLoS One, 2017. **12**(1): p. e0168669.

50. Hennessy, B.T., et al., *Characterization of a naturally occurring breast cancer subset enriched in epithelial-to-mesenchymal transition and stem cell characteristics.* Cancer Res, 2009. **69**(10): p. 4116-24.

51. Sabatier, R., et al., *Claudin-low breast cancers: clinical, pathological, molecular and prognostic characterization.* Mol Cancer, 2014. **13**: p. 228.

52. Dent, R., et al., *Triple-negative breast cancer: clinical features and patterns of recurrence.* Clin Cancer Res, 2007. **13**(15 Pt 1): p. 4429-34.

53. Liedtke, C., et al., *Response to neoadjuvant therapy and long-term survival in patients with triple-negative breast cancer.* J Clin Oncol, 2008. **26**(8): p. 1275-81.

54. Amos, K.D., B. Adamo, and C.K. Anders, *Triple-negative breast cancer: an update on neoadjuvant clinical trials.* Int J Breast Cancer, 2012. **2012**: p. 385978.

55. Rouzier, R., et al., *Breast cancer molecular subtypes respond differently to preoperative chemotherapy.* Clin Cancer Res, 2005. **11**(16): p. 5678-85.

56. Carey, L.A., et al., *The triple negative paradox: primary tumor chemosensitivity of breast cancer subtypes.* Clin Cancer Res, 2007. **13**(8): p. 2329-34.

57. Zhang, C., et al., *Higher locoregional recurrence rate for triple-negative breast cancer following neoadjuvant chemotherapy, surgery and radiotherapy.* Springerplus, 2015. **4**: p. 386.

58. Chen, V.E., et al., *Pathologic response after neoadjuvant chemotherapy predicts locoregional control in patients with triple negative breast cancer.* Adv Radiat Oncol, 2017. **2**(2): p. 105-109.

59. Bissell, M.J. and W.C. Hines, *Why don't we get more cancer? A proposed role of the microenvironment in restraining cancer progression.* Nat Med, 2011. **17**(3): p. 320-9.

60. Neve, R.M., et al., *A collection of breast cancer cell lines for the study of functionally distinct cancer subtypes.* Cancer Cell, 2006. **10**(6): p. 515-27.

61. Casbas-Hernandez, P., J.M. Fleming, and M.A. Troester, *Gene expression analysis of in vitro cocultures to study interactions between breast epithelium and stroma.* J Biomed Biotechnol, 2011. **2011**: p. 520987.

62. Katt, M.E., et al., *In Vitro Tumor Models: Advantages, Disadvantages, Variables, and Selecting the Right Platform.* Front Bioeng Biotechnol, 2016. **4**: p. 12.

63. Wells, R.G., *The role of matrix stiffness in regulating cell behavior.* Hepatology, 2008. **47**(4): p. 1394-400.

64. Lee, G.Y., et al., *Three-dimensional culture models of normal and malignant breast epithelial cells.* Nat Methods, 2007. **4**(4): p. 359-65.

65. Lo, A.T., et al., *Constructing three-dimensional models to study mammary gland branching morphogenesis and functional differentiation.* J Mammary Gland Biol Neoplasia, 2012. **17**(2): p. 103-10.

66. Barcellos-Hoff, M.H., et al., *Functional differentiation and alveolar morphogenesis of primary mammary cultures on reconstituted basement membrane.* Development, 1989. **105**(2): p. 223-35.

67. Simian, M. and M.J. Bissell, *Organoids: A historical perspective of thinking in three dimensions.* J Cell Biol, 2017. **216**(1): p. 31-40.

68. Chhetri, R.K., et al., *Longitudinal study of mammary epithelial and fibroblast co-cultures using optical coherence tomography reveals morphological hallmarks of pre-malignancy.* PLoS One, 2012. **7**(11): p. e49148.

69. Oldenburg, A.L., et al., *Inverse-power-law behavior of cellular motility reveals stromal-epithelial cell interactions in 3D co-culture by OCT fluctuation spectroscopy.* Optica, 2015. **2**(10): p. 877-885.

70. Blackmon, R.L., et al., *Imaging Extracellular Matrix Remodeling In Vitro by Diffusion-Sensitive Optical Coherence Tomography.* Biophys J, 2016. **110**(8): p. 1858-1868.

71. Yu, X., et al., *Quantification of The Effect of Toxicants on the Intracellular Kinetic Energy and Cross-Sectional Area of Mammary Epithelial Organoids by OCT Fluctuation Spectroscopy.* Toxicol Sci, 2017. **162**(1): p. 234-240.

72. Ocana, A., et al., *Preclinical development of molecular-targeted agents for cancer.* Nat Rev Clin Oncol, 2010. **8**(4): p. 200-9.

73. Pfefferle, A.D., et al., *Transcriptomic classification of genetically engineered mouse models of breast cancer identifies human subtype counterparts.* Genome Biol, 2013. **14**(11): p. R125.

74. Herschkowitz, J.I., et al., *Comparative oncogenomics identifies breast tumors enriched in functional tumor-initiating cells.* Proc Natl Acad Sci U S A, 2012. **109**(8): p. 2778-83.

75. Knight, J.F., et al., *Met synergizes with p53 loss to induce mammary tumors that possess features of claudin-low breast cancer.* Proc Natl Acad Sci U S A, 2013. **110**(14): p. E1301-10.

76. Casbas-Hernandez, P., et al., *Tumor intrinsic subtype is reflected in cancer-adjacent tissue.* Cancer Epidemiol Biomarkers Prev, 2015. **24**(2): p. 406-14.

77. Graham, K., et al., *Gene expression profiles of estrogen receptor-positive and estrogen receptor-negative breast cancers are detectable in histologically normal breast epithelium.* Clin Cancer Res, 2011. **17**(2): p. 236-46.

78. Troester, M.A., et al., *DNA defects, epigenetics, and gene expression in cancer-adjacent breast: a study from The Cancer Genome Atlas.* NPJ Breast Cancer, 2016. **2**: p. 16007.

79. Roman-Perez, E., et al., *Gene expression in extratumoral microenvironment predicts clinical outcome in breast cancer patients.* Breast Cancer Res, 2012. **14**(2): p. R51.

80. Finak, G., et al., *Stromal gene expression predicts clinical outcome in breast cancer.* Nat Med, 2008. **14**(5): p. 518-27.

81. Kalluri, R. and M. Zeisberg, *Fibroblasts in cancer.* Nat Rev Cancer, 2006. **6**(5): p. 392-401.

82. Moorman, A.M., et al., *The prognostic value of tumour-stroma ratio in triple-negative breast cancer.* Eur J Surg Oncol, 2012. **38**(4): p. 307-13.

83. Yaghjyan, L., et al., *Mammographic breast density and subsequent risk of breast cancer in postmenopausal women according to tumor characteristics.* J Natl Cancer Inst, 2011. **103**(15): p. 1179-89.

84. Kerlikowske, K. and A.I. Phipps, *Breast density influences tumor subtypes and tumor aggressiveness.* J Natl Cancer Inst, 2011. **103**(15): p. 1143-5.

85. Camp, J.T., et al., *Interactions with fibroblasts are distinct in Basal-like and luminal breast cancers.* Mol Cancer Res, 2011. **9**(1): p. 3-13.

86. Hsu, H.C., et al., *Stromal Fibroblasts from the Interface Zone of Triple Negative Breast Carcinomas Induced Epithelial-Mesenchymal Transition and its Inhibition by Emodin.* PLoS One, 2017. **12**(1): p. e0164661.

87. Mueller, K.L., et al., *Fibroblast-secreted hepatocyte growth factor mediates epidermal growth factor receptor tyrosine kinase inhibitor resistance in triple-negative breast cancers through paracrine activation of Met.* Breast Cancer Res, 2012. **14**(4): p. R104.

88. Costa, A., et al., *Fibroblast Heterogeneity and Immunosuppressive Environment in Human Breast Cancer.* Cancer Cell, 2018. **33**(3): p. 463-479.

89. Allaoui, R., et al., *Cancer-associated fibroblast-secreted CXCL16 attracts monocytes to promote stroma activation in triple-negative breast cancers.* Nat Commun, 2016. **7**: p. 13050.

90. Takai, K., et al., *Targeting the cancer-associated fibroblasts as a treatment in triple-negative breast cancer.* Oncotarget, 2016. **7**(50): p. 82889-82901.

91. Gouon-Evans, V., M.E. Rothenberg, and J.W. Pollard, *Postnatal mammary gland development requires macrophages and eosinophils.* Development, 2000. **127**(11): p. 2269-82.

92. Van Nguyen, A. and J.W. Pollard, *Colony stimulating factor-1 is required to recruit macrophages into the mammary gland to facilitate mammary ductal outgrowth.* Dev Biol, 2002. **247**(1): p. 11-25.

93. Humphreys, R.C., et al., *Apoptosis in the terminal endbud of the murine mammary gland: a mechanism of ductal morphogenesis.* Development, 1996. **122**(12): p. 4013-22.

94. Gyorki, D.E., et al., *Resident macrophages influence stem cell activity in the mammary gland.* Breast Cancer Res, 2009. **11**(4): p. R62.

95. Lin, E.Y., et al., *Macrophages regulate the angiogenic switch in a mouse model of breast cancer.* Cancer Res, 2006. **66**(23): p. 11238-46.

96. Lin, L., et al., *CCL18 from tumor-associated macrophages promotes angiogenesis in breast cancer.* Oncotarget, 2015. **6**(33): p. 34758-73.

97. Mantovani, A., et al., *Tumor-associated macrophages and the related myeloid-derived suppressor cells as a paradigm of the diversity of macrophage activation.* Hum Immunol, 2009. **70**(5): p. 325-30.

98. Chen, Y., et al., *Tumor-recruited M2 macrophages promote gastric and breast cancer metastasis via M2 macrophage-secreted CHI3L1 protein.* J Hematol Oncol, 2017. **10**(1): p. 36.

99. Chen, J., et al., *CCL18 from tumor-associated macrophages promotes breast cancer metastasis via PITPNM3.* Cancer Cell, 2011. **19**(4): p. 541-55.

100. Qian, B.Z. and J.W. Pollard, *Macrophage diversity enhances tumor progression and metastasis.* Cell, 2010. **141**(1): p. 39-51.

101. Campbell, M.J., et al., *Proliferating macrophages associated with high grade, hormone receptor negative breast cancer and poor clinical outcome.* Breast Cancer Res Treat, 2011. **128**(3): p. 703-711.

102. Yao, M., et al., *Elevated expression of chemokine C-C ligand 2 in stroma is associated with recurrent basal-like breast cancers.* Mod Pathol, 2016. **29**(8): p. 810-23.

103. Medrek, C., et al., *The presence of tumor associated macrophages in tumor stroma as a prognostic marker for breast cancer patients.* BMC Cancer, 2012. **12**: p. 306.

104. Yuan, Z.Y., et al., *High infiltration of tumor-associated macrophages in triple-negative breast cancer is associated with a higher risk of distant metastasis.* Onco Targets Ther, 2014. **7**: p. 1475-80.

105. Laoui, D., et al., *Tumor-associated macrophages in breast cancer: distinct subsets, distinct functions.* Int J Dev Biol, 2011. **55**(7-9): p. 861-867.

106. Sousa, S., et al., *Human breast cancer cells educate macrophages toward the M2 activation status.* Breast Cancer Res, 2015. **17**: p. 101.

107. Stewart, D.A., et al., *Basal-like breast cancer cells induce phenotypic and genomic changes in macrophages.* Mol Cancer Res, 2012. **10**(6): p. 727-38.

108. Bergers, G. and L.E. Benjamin, *Tumorigenesis and the angiogenic switch.* Nature Reviews Cancer, 2003. **3**: p. 401.

109. Nalwoga, H., et al., *Vascular proliferation is increased in basal-like breast cancer.* Breast Cancer Res Treat, 2011. **130**(3): p. 1063-71.

110. Bujor, I.S., et al., *Evaluation of Vascular Proliferation in Molecular Subtypes of Breast Cancer.* In Vivo, 2018. **32**(1): p. 79-83.

111. Ingthorsson, S., et al., *Endothelial cells stimulate growth of normal and cancerous breast epithelial cells in 3D culture.* BMC Res Notes, 2010. **3**: p. 184.

112. Sigurdsson, V., et al., *Endothelial induced EMT in breast epithelial cells with stem cell properties.* PLoS One, 2011. **6**(9): p. e23833.

113. Di Modica, M., et al., *Breast cancer-secreted miR-939 downregulates VE-cadherin and destroys the barrier function of endothelial monolayers.* Cancer Lett, 2017. **384**: p. 94-100.

114. Zhang, W., et al., *Endothelial cells promote triple-negative breast cancer cell metastasis via PAI-1 and CCL5 signaling.* FASEB J, 2018. **32**(1): p. 276-288.

115. Marme, F. and A. Schneeweiss, *Targeted Therapies in Triple-Negative Breast Cancer.* Breast Care (Basel), 2015. **10**(3): p. 159-66.

116. Sigurdsson, V., et al., *Human breast microvascular endothelial cells retain phenotypic traits in long-term finite life span culture.* In Vitro Cell Dev Biol Anim, 2006. **42**(10): p. 332-40.

117. Naccarato, A.G., et al., *Definition of the microvascular pattern of the normal human adult mammary gland.* J Anat, 2003. **203**(6): p. 599-603.

118. Guray, M. and A.A. Sahin, *Benign breast diseases: classification, diagnosis, and management.* Oncologist, 2006. **11**(5): p. 435-49.

119. Hartmann, L.C., et al., *Benign breast disease and the risk of breast cancer.* N Engl J Med, 2005. **353**(3): p. 229-37.

120. Dupont, W.D. and D.L. Page, *Risk factors for breast cancer in women with proliferative breast disease.* N Engl J Med, 1985. **312**(3): p. 146-51.

121. Ellis, I.O., *Intraductal proliferative lesions of the breast: morphology, associated risk and molecular biology.* Mod Pathol, 2010. **23 Suppl 2**: p. S1-7.

122. Hartmann, L.C., et al., *Atypical hyperplasia of the breast--risk assessment and management options.* N Engl J Med, 2015. **372**(1): p. 78-89.

123. Degnim, A.C., et al., *Extent of atypical hyperplasia stratifies breast cancer risk in 2 independent cohorts of women.* Cancer, 2016. **122**(19): p. 2971-8.

124. Menes, T.S., et al., *Subsequent Breast Cancer Risk Following Diagnosis of Atypical Ductal Hyperplasia on Needle Biopsy.* JAMA Oncol, 2017. **3**(1): p. 36-41.

125. Renshaw, A.A. and E.W. Gould, *Long term clinical follow-up of atypical ductal hyperplasia and lobular carcinoma in situ in breast core needle biopsies.* Pathology, 2016. **48**(1): p. 25-9.

126. London, S.J., et al., *A prospective study of benign breast disease and the risk of breast cancer.* JAMA, 1992. **267**(7): p. 941-4.

127. Hartmann, L.C., et al., *Understanding the premalignant potential of atypical hyperplasia through its natural history: a longitudinal cohort study.* Cancer Prev Res (Phila), 2014. **7**(2): p. 211-7.

128. Kerlikowske, K., *Epidemiology of ductal carcinoma in situ.* J Natl Cancer Inst Monogr, 2010. **2010**(41): p. 139-41.

129. Page, D.L., et al., *Atypical hyperplastic lesions of the female breast. A long-term follow-up study.* Cancer, 1985. **55**(11): p. 2698-708.

130. Clark, S.E., et al., *Molecular subtyping of DCIS: heterogeneity of breast cancer reflected in pre-invasive disease.* Br J Cancer, 2011. **104**(1): p. 120-7.

131. Livasy, C.A., et al., *Identification of a basal-like subtype of breast ductal carcinoma in situ.* Hum Pathol, 2007. **38**(2): p. 197-204.

132. Tamimi, R.M., et al., *Comparison of molecular phenotypes of ductal carcinoma in situ and invasive breast cancer.* Breast Cancer Res, 2008. **10**(4): p. R67.

133. Meijnen, P., et al., *Immunohistochemical categorisation of ductal carcinoma in situ of the breast.* Br J Cancer, 2008. **98**(1): p. 137-42.

134. Muggerud, A.A., et al., *Molecular diversity in ductal carcinoma in situ (DCIS) and early invasive breast cancer.* Mol Oncol, 2010. **4**(4): p. 357-68.

135. Kumar, A.S., V. Bhatia, and I.C. Henderson, *Overdiagnosis and overtreatment of breast cancer: rates of ductal carcinoma in situ: a US perspective.* Breast Cancer Res, 2005. **7**(6): p. 271-5.

136. Page, D.L., et al., *Continued local recurrence of carcinoma 15-25 years after a diagnosis of low grade ductal carcinoma in situ of the breast treated only by biopsy.* Cancer, 1995. **76**(7): p. 1197-200.

137. Sanders, M.E., et al., *The natural history of low-grade ductal carcinoma in situ of the breast in women treated by biopsy only revealed over 30 years of long-term follow-up.* Cancer, 2005. **103**(12): p. 2481-4.

138. Cowell, C.F., et al., *Progression from ductal carcinoma in situ to invasive breast cancer: revisited.* Mol Oncol, 2013. **7**(5): p. 859-69.

139. Porter, D., et al., *Molecular markers in ductal carcinoma in situ of the breast.* Mol Cancer Res, 2003. **1**(5): p. 362-75.

140. Ma, X.J., et al., *Gene expression profiles of human breast cancer progression.* Proc Natl Acad Sci U S A, 2003. **100**(10): p. 5974-9.

141. Sgroi, D.C., *Preinvasive breast cancer.* Annu Rev Pathol, 2010. **5**: p. 193-221.

142. Burkhardt, L., et al., *Gene amplification in ductal carcinoma in situ of the breast.* Breast Cancer Res Treat, 2010. **123**(3): p. 757-65.

143. O'Connell, P., et al., *Analysis of loss of heterozygosity in 399 premalignant breast lesions at 15 genetic loci.* J Natl Cancer Inst, 1998. **90**(9): p. 697-703.

144. Done, S.J., et al., *p53 mutations in mammary ductal carcinoma in situ but not in epithelial hyperplasias.* Cancer Res, 1998. **58**(4): p. 785-9.

145. van der Groep, P., et al., *Molecular profile of ductal carcinoma in situ of the breast in BRCA1 and BRCA2 germline mutation carriers.* J Clin Pathol, 2009. **62**(10): p. 926-30.

146. Half, E., et al., *Cyclooxygenase-2 expression in human breast cancers and adjacent ductal carcinoma in situ.* Cancer Res, 2002. **62**(6): p. 1676-81.

147. Dietrich, D., et al., *[Multiplexed methylation analysis--a new technology to analyse the methylation pattern of laser microdissected cells of normal breast tissue, DCIS and invasive ductal carcinoma of the breast].* Verh Dtsch Ges Pathol, 2007. **91**: p. 197-207.

148. O'Connell, P., et al., *Molecular genetic studies of early breast cancer evolution.* Breast Cancer Res Treat, 1994. **32**(1): p. 5-12.

149. Sun, Y., et al., *Primed atypical ductal hyperplasia-associated fibroblasts promote cell growth and polarity changes of transformed epithelium-like breast cancer MCF-7 cells via miR-200b/c-IKKbeta signaling.* Cell Death Dis, 2018. **9**(2): p. 122.

150. Casbas-Hernandez, P., et al., *Role of HGF in epithelial-stromal cell interactions during progression from benign breast disease to ductal carcinoma in situ.* Breast Cancer Res, 2013. **15**(5): p. R82.

151. Allinen, M., et al., *Molecular characterization of the tumor microenvironment in breast cancer.* Cancer Cell, 2004. **6**(1): p. 17-32.

152. Cichon, M.A., et al., *Microenvironmental influences that drive progression from benign breast disease to invasive breast cancer.* J Mammary Gland Biol Neoplasia, 2010. **15**(4): p. 389-97.

153. Hu, M., et al., *Distinct epigenetic changes in the stromal cells of breast cancers.* Nat Genet, 2005. **37**(8): p. 899-905.

154. Hilson, J.B., S.J. Schnitt, and L.C. Collins, *Phenotypic alterations in ductal carcinoma in situ-associated myoepithelial cells: biologic and diagnostic implications.* Am J Surg Pathol, 2009. **33**(2): p. 227-32.

155. Hu, M., et al., *Regulation of in situ to invasive breast carcinoma transition.* Cancer Cell, 2008. **13**(5): p. 394-406.

156. Hu, M., et al., *Role of COX-2 in epithelial-stromal cell interactions and progression of ductal carcinoma in situ of the breast.* Proc Natl Acad Sci U S A, 2009. **106**(9): p. 3372-7.

157. Sternlicht, M.D., et al., *The human myoepithelial cell is a natural tumor suppressor.* Clin Cancer Res, 1997. **3**(11): p. 1949-58.

158. Lo, P.K., et al., *Tumor-associated myoepithelial cells promote the invasive progression of ductal carcinoma in situ through activation of TGFbeta signaling.* J Biol Chem, 2017. **292**(27): p. 11466-11484.

159. Sarper, M., et al., *Loss of MMP-8 in ductal carcinoma in situ (DCIS)-associated myoepithelial cells contributes to tumour promotion through altered adhesive and proteolytic function.* Breast Cancer Res, 2017. **19**(1): p. 33.

160. Bombonati, A. and D.C. Sgroi, *The molecular pathology of breast cancer progression.* J Pathol, 2011. **223**(2): p. 307-17.

161. Ma, X.J., et al., *Gene expression profiling of the tumor microenvironment during breast cancer progression.* Breast Cancer Res, 2009. **11**(1): p. R7.

162. Troester, M.A., et al., *Gene expression patterns associated with p53 status in breast cancer.* BMC Cancer, 2006. **6**: p. 276.

163. Masutomi, K., et al., *Telomerase maintains telomere structure in normal human cells.* Cell, 2003. **114**(2): p. 241-53.

164. Johnson, K.R., J.L. Leight, and V.M. Weaver, *Demystifying the effects of a three-dimensional microenvironment in tissue morphogenesis.* Methods Cell Biol, 2007. **83**: p. 547-83.

165. Buess, M., et al., *Characterization of heterotypic interaction effects in vitro to deconvolute global gene expression profiles in cancer.* Genome Biol, 2007. **8**(9): p. R191.

166. Mailleux, A.A., M. Overholtzer, and J.S. Brugge, *Lumen formation during mammary epithelial morphogenesis: insights from in vitro and in vivo models.* Cell Cycle, 2008. **7**(1): p. 57-62.

167. Verbsky, J. and P.W. Majerus, *Increased levels of inositol hexakisphosphate (InsP6) protect HEK293 cells from tumor necrosis factor (alpha)- and Fas-induced apoptosis.* J Biol Chem, 2005. **280**(32): p. 29263-8.

168. Moogk, D., et al., *Melanoma expression of matrix metalloproteinase-23 is associated with blunted tumor immunity and poor responses to immunotherapy.* J Transl Med, 2014. **12**: p. 342.

169. Laurin, M., et al., *Rac-specific guanine nucleotide exchange factor DOCK1 is a critical regulator of HER2-mediated breast cancer metastasis.* Proc Natl Acad Sci U S A, 2013. **110**(18): p. 7434-9.

170. D'Arcy, M., et al., *Race-associated biological differences among Luminal A breast tumors.* Breast Cancer Res Treat, 2015. **152**(2): p. 437-48.

171. Field, L.A., et al., *Identification of differentially expressed genes in breast tumors from African American compared with Caucasian women.* Cancer, 2012. **118**(5): p. 1334-44.

172. Stewart, P.A., et al., *Differentially expressed transcripts and dysregulated signaling pathways and networks in African American breast cancer.* PLoS One, 2013. **8**(12): p. e82460.

173. Castro, N.P., et al., *Evidence that molecular changes in cells occur before morphological alterations during the progression of breast ductal carcinoma.* Breast Cancer Res, 2008. **10**(5): p. R87.

174. Sadlonova, A., et al., *Breast fibroblasts modulate epithelial cell proliferation in three-dimensional in vitro co-culture.* Breast Cancer Res, 2005. **7**(1): p. R46-59.

175. Sadlonova, A., et al., *Identification of molecular distinctions between normal breast-associated fibroblasts and breast cancer-associated fibroblasts.* Cancer Microenviron, 2009. **2**(1): p. 9-21.

176. Petersen, O.W., et al., *Interaction with basement membrane serves to rapidly distinguish growth and differentiation pattern of normal and malignant human breast epithelial cells.* Proc Natl Acad Sci U S A, 1992. **89**(19): p. 9064-8.

177. Weaver, V.M., et al., *Reversion of the malignant phenotype of human breast cells in three-dimensional culture and in vivo by integrin blocking antibodies.* J Cell Biol, 1997. **137**(1): p. 231-45.

178. Laoui, D., et al., *Functional Relationship between Tumor-Associated Macrophages and Macrophage Colony-Stimulating Factor as Contributors to Cancer Progression.* Front Immunol, 2014. **5**.

179. Mukhtar, R.A., et al., *Elevated levels of proliferating and recently migrated tumor-associated macrophages confer increased aggressiveness and worse outcomes in breast cancer.* Ann Surg Oncol, 2012. **19**(12): p. 3979-86.

180. Hanahan, D. and R.A. Weinberg, *Hallmarks of cancer: the next generation.* Cell, 2011. **144**(5): p. 646-74.

181. Vats, D., et al., *Oxidative metabolism and PGC-1beta attenuate macrophage-mediated inflammation.* Cell Metab, 2006. **4**(1): p. 13-24.

182. Freemerman, A.J., et al., *Metabolic reprogramming of macrophages: glucose transporter 1 (GLUT1)-mediated glucose metabolism drives a proinflammatory phenotype.* J Biol Chem, 2014. **289**(11): p. 7884-96.

183. Freemerman, A.J., et al., *Myeloid Slc2a1-deficient Murine Model Revealed Macrophage Activation and Metabolic Phenotype is Fueled by GLUT1.* Submitted, 2018.

184. Dunlap, S.M., et al., *Dietary energy balance modulates epithelial-to-mesenchymal transition and tumor progression in murine claudin-low and basal-like mammary tumor models.* Cancer Prev Res (Phila), 2012. **5**(7): p. 930-42.

185. Cho, K.W., et al., *Adipose Tissue Dendritic Cells Are Independent Contributors to Obesity-Induced Inflammation and Insulin Resistance.* J Immunol, 2016. **197**(9): p. 3650-3661.

186. Tamoutounour, S., et al., *CD64 distinguishes macrophages from dendritic cells in the gut and reveals the Th1-inducing role of mesenteric lymph node macrophages during colitis.* Eur J Immunol, 2012. **42**(12): p. 3150-66.

187. Tomayko, M.M. and C.P. Reynolds, *Determination of subcutaneous tumor size in athymic (nude) mice.* Cancer Chemother Pharmacol, 1989. **24**(3): p. 148-54.

188. Sundaram, S., et al., *Role of HGF in obesity-associated tumorigenesis: C3(1)-TAg mice as a model for human basal-like breast cancer.* Breast Cancer Res Treat, 2013. **142**(3): p. 489-503.

189. Kratz, M., et al., *Metabolic dysfunction drives a mechanistically distinct proinflammatory phenotype in adipose tissue macrophages.* Cell Metab, 2014. **20**(4): p. 614-25.

190. Li, P., et al., *Functional heterogeneity of CD11c-positive adipose tissue macrophages in diet-induced obese mice.* J Biol Chem, 2010. **285**(20): p. 15333-45.

191. Nakajima, S., et al., *Accumulation of CD11c+CD163+ Adipose Tissue Macrophages through Upregulation of Intracellular 11beta-HSD1 in Human Obesity.* J Immunol, 2016. **197**(9): p. 3735-3745.

192. Shaul, M.E., et al., *Dynamic, M2-like remodeling phenotypes of CD11c+ adipose tissue macrophages during high-fat diet--induced obesity in mice.* Diabetes, 2010. **59**(5): p. 1171-81.

193. Weisberg, S.P., et al., *Obesity is associated with macrophage accumulation in adipose tissue.* J Clin Invest, 2003. **112**(12): p. 1796-808.

194. Wentworth, J.M., et al., *Pro-inflammatory CD11c+CD206+ adipose tissue macrophages are associated with insulin resistance in human obesity.* Diabetes, 2010. **59**(7): p. 1648-56.

195. Zeyda, M., et al., *Human adipose tissue macrophages are of an anti-inflammatory phenotype but capable of excessive pro-inflammatory mediator production.* Int J Obes (Lond), 2007. **31**(9): p. 1420-8.

196. Williams, C.B., E.S. Yeh, and A.C. Soloff, *Tumor-associated macrophages: unwitting accomplices in breast cancer malignancy.* NPJ Breast Cancer, 2016. **2**.

197. Driessens, G., J. Kline, and T.F. Gajewski, *Costimulatory and coinhibitory receptors in anti-tumor immunity.* Immunol Rev, 2009. **229**(1): p. 126-44.

198. Arendt, L.M., et al., *Obesity promotes breast cancer by CCL2-mediated macrophage recruitment and angiogenesis.* Cancer Res, 2013. **73**(19): p. 6080-93.

199. Morris, P.G., et al., *Inflammation and increased aromatase expression occur in the breast tissue of obese women with breast cancer.* Cancer Prev Res (Phila), 2011. **4**(7): p. 1021-9.

200. Xu, X., et al., *Obesity activates a program of lysosomal-dependent lipid metabolism in adipose tissue macrophages independently of classic activation.* Cell Metab, 2013. **18**(6): p. 816-30.

201. Tirapu, I., et al., *Low surface expression of B7-1 (CD80) is an immunoescape mechanism of colon carcinoma.* Cancer Res, 2006. **66**(4): p. 2442-50.

202. Haile, S.T., et al., *Tumor cell programmed death ligand 1-mediated T cell suppression is overcome by coexpression of CD80.* J Immunol, 2011. **186**(12): p. 6822-9.

203. Geeraerts, X., et al., *Macrophage Metabolism As Therapeutic Target for Cancer, Atherosclerosis, and Obesity.* Front Immunol, 2017. **8**.

204. Penny, H.L., et al., *Warburg metabolism in tumor-conditioned macrophages promotes metastasis in human pancreatic ductal adenocarcinoma.* Oncoimmunology, 2016. **5**(8): p. e1191731.

205. Forero, A., et al., *Expression of the MHC Class II Pathway in Triple-Negative Breast Cancer Tumor Cells Is Associated with a Good Prognosis and Infiltrating Lymphocytes.* Cancer Immunol Res, 2016. **4**(5): p. 390-399.

206. He, Y., et al., *MHC class II expression in lung cancer.* Lung Cancer, 2017. **112**: p. 75-80.

207. Johnson, D.B., et al., *Melanoma-specific MHC-II expression represents a tumour-autonomous phenotype and predicts response to anti-PD-1/PD-L1 therapy.* Nat Commun, 2016. **7**: p. 10582.

208. Park, I.A., et al., *Expression of the MHC class II in triple-negative breast cancer is associated with tumor-infiltrating lymphocytes and interferon signaling.* PLoS One, 2017. **12**(8): p. e0182786.

209. Wang, B., et al., *Transition of tumor-associated macrophages from MHC class II(hi) to MHC class II(low) mediates tumor progression in mice.* BMC Immunol, 2011. **12**: p. 43.

210. Abram, C.L., et al., *Comparative analysis of the efficiency and specificity of myeloid-Cre deleting strains using ROSA-EYFP reporter mice.* J Immunol Methods, 2014. **408**: p. 89-100.

211. Sandhu, R., et al., *Digital histologic analysis reveals morphometric patterns of age-related involution in breast epithelium and stroma.* Hum Pathol, 2016. **48**: p. 60-8.

212. Chollet-Hinton, L., et al., *Stroma modifies relationships between risk factor exposure and age-related epithelial involution in benign breast.* Mod Pathol, 2018.

213. Freitas, R.A., *Nanomedicine, Volume 1: Basic Capabilities*. 1999, Austin, TX: Landes Bioscience.

214. Landis, J.R. and G.G. Koch, *The measurement of observer agreement for categorical data.* Biometrics, 1977. **33**(1): p. 159-74.

215. Lee, H.O., et al., *Evolution of tumor invasiveness: the adaptive tumor microenvironment landscape model.* Cancer Res, 2011. **71**(20): p. 6327-37.

216. Hurst, R.E., et al., *Targeting dormant micrometastases: rationale, evidence to date and clinical implications.* Ther Adv Med Oncol, 2016. **8**(2): p. 126-37.

217. Ghajar, C.M., et al., *The perivascular niche regulates breast tumour dormancy.* Nat Cell Biol, 2013. **15**(7): p. 807-17.

218. Bibby, M.C., *Orthotopic models of cancer for preclinical drug evaluation: advantages and disadvantages.* Eur J Cancer, 2004. **40**(6): p. 852-7.

219. O'Leary, K.A., et al., *Prolactin cooperates with loss of p53 to promote claudin-low mammary carcinomas.* Oncogene, 2014. **33**(23): p. 3075-82.

220. Yamamoto, Y., et al., *Quantitative diagnosis of breast tumors by morphometric classification of microenvironmental myoepithelial cells using a machine learning approach.* Sci Rep, 2017. **7**: p. 46732.

221. Xu, Y., et al., *Large scale tissue histopathology image classification, segmentation, and visualization via deep convolutional activation features.* BMC Bioinformatics, 2017. **18**(1): p. 281.

222. Mani, S., et al., *Machine learning for predicting the response of breast cancer to neoadjuvant chemotherapy.* J Am Med Inform Assoc, 2013. **20**(4): p. 688-95.

223. Montazeri, M., et al., *Machine learning models in breast cancer survival prediction.* Technol Health Care, 2016. **24**(1): p. 31-42.

224. Bessette, D.C., et al., *Using the MCF10A/MCF10CA1a Breast Cancer Progression Cell Line Model to Investigate the Effect of Active, Mutant Forms of EGFR in Breast*

Cancer Development and Treatment Using Gefitinib. PLoS One, 2015. **10**(5): p. e0125232.

225. Sun, P., et al., *miR-186 regulates glycolysis through Glut1 during the formation of cancer-associated fibroblasts.* Asian Pac J Cancer Prev, 2014. **15**(10): p. 4245-50.

226. Whitaker-Menezes, D., et al., *Evidence for a stromal-epithelial "lactate shuttle" in human tumors: MCT4 is a marker of oxidative stress in cancer-associated fibroblasts.* Cell Cycle, 2011. **10**(11): p. 1772-83.

227. Fiaschi, T., et al., *Reciprocal metabolic reprogramming through lactate shuttle coordinately influences tumor-stroma interplay.* Cancer Res, 2012. **72**(19): p. 5130-40.

228. Zhang, D., et al., *Metabolic reprogramming of cancer-associated fibroblasts by IDH3alpha downregulation.* Cell Rep, 2015. **10**(8): p. 1335-48.

229. Pertega-Gomes, N., et al., *A lactate shuttle system between tumour and stromal cells is associated with poor prognosis in prostate cancer.* BMC Cancer, 2014. **14**: p. 352.

230. Heaphy, C.M., et al., *Telomere DNA content and allelic imbalance demonstrate field cancerization in histologically normal tissue adjacent to breast tumors.* Int J Cancer, 2006. **119**(1): p. 108-16.

231. Trujillo, K.A., et al., *Markers of fibrosis and epithelial to mesenchymal transition demonstrate field cancerization in histologically normal tissue adjacent to breast tumors.* Int J Cancer, 2011. **129**(6): p. 1310-21.

232. Trujillo, K.A., et al., *Breast field cancerization: isolation and comparison of telomerase-expressing cells in tumor and tumor adjacent, histologically normal breast tissue.* Mol Cancer Res, 2011. **9**(9): p. 1209-21.